UCLouvain

École polytechnique de Louvain

Quantifying the microstructural changes in the brain of patients with alcohol use disorder after abstinence via diffusion MRI

Author: **Delinte Nicolas**
Supervisors: **Macq Benoît, Dricot Laurence**
Readers: **Rensonnet Gaëtan, Peeters Frank**
Academic year 2019–2020
Master [120] in Biomedical Engineering

Abstract

In recent years, there has been an increased interest for the characterization of neuropathologies, such as alcohol use disorder, using diffusion MRI. Diffusion MRI is an imaging technique based on the diffusion of water molecules, which can provide information about the microstructure of the brain. The goal of this report is to identify which diffusion-based models and their respective metrics best describe the microstructural changes observed during abstinence in different brain regions and to identify which of these regions are the most impacted.
A patient with alcohol use disorder was scanned with a diffusion MRI sequence before and after a two week abstinence period from alcohol. A data processing pipeline was created to obtain the metrics of different models from the diffusion data and a selection of the most useful metrics was determined. A region-based analysis found that regions such as the corpus callosum, the limbic system and the cerebellar peduncles presented a high number of microstructural changes.

Acknowledgements

I would like to thank Benoit Macq for giving me the opportunity to work on this subject during my master's thesis.

I would also like to show my gratitude to Geatan Rensonnet, Laurence Dricot and Philippe de Timary for the time and attention they took to answer my questions about this multi-disciplinary subject.

Last but not least, I would like to thank Ysaline and Alexandre for the mutual assistance and great atmosphere they provided while working on this thesis.

Contents

List of Figures

List of Tables

Abbreviations

AD Axial Diffusivity.

ADC Apparent Diffusion Coefficient.

AK Axial Kurtosis.

AUD Alcohol Use Disorder.

BBB Blood-Brain Barrier.

CC Corpus Callosum.

cFA compartment Fractional Anisotropy.

CSD Constrained Spherical Deconvolution.

CSF Cerebro Spinal Fluid.

CT Computed Tomography.

DIAMOND DIstribution of 3D Anisotropic MicrOstructural eNvironments in Diffusion-compartment imaging.

DICOM Digital Imaging and Communications in Medicine.

DKI Diffusion Kurtosis Imaging.

dMRI Diffusion MRI.

DTI Diffusion Tensor Imaging.

DWI Diffusion-Weighted Imaging.

FA Fractional Anisotropy.

fODF fiber Orientation Distribution Function.

FOV Field Of View.

gFA generalized FA.

MD Mean Diffusivity.

MI Mutual Information.

MK Mean Kurtosis.

MNI Montreal Neurological Institute.

MRI Magnetic Resonance Imaging.

MSDKI Mean Signal Diffusion Kurtosis Imaging.

NODDI Neurite Orientation Dispersion and Density Imaging.

ODI Orientation Dispersion Index.

PGSE Pulse Gradient Spin Echo.

PMF Probability Mass Function.

RD Radial Diffusivity.

RF Radio Frequency.

RGB Red Green Blue.

RK Radial Kurtosis.

ROI Region Of Interest.

TBSS Tract-based Spatial Statistics.

TE Echo time.

TR Repetition Time.

VOI Volume Of Interest.

WM White Matter.

WMTI White Matter Tract Integrity.

Introduction

In recent years, there has been an increased interest for the characterization of neuropathologies using diffusion-weighted magnetic resonance imaging. Alcohol use disorder is one of those neuropathologies.

Alcohol-dependence is a widely spread disorder that is estimated to be present in 5–7% of the population of developed countries. Since alcohol use disorder (AUD) impacts both the mental and physical health of the patient, it becomes difficult to treat as both mood and cognition alterations play a role in the motivation for alcohol-drinking.

de Timary & al. [1] have identified a metabolic pathway linking alcohol consumption and neuro-inflammation. Chronic alcohol abuse alters the composition of the gut microbiota, changing its permeability and allowing bacterial components to pass through the gut membrane and reach the systemic circulation. This initiates an inflammatory cascade allowing inflammatory molecules to reach the central nervous system, induce neuro-inflammation and impact the brain microstructure.

These microstructural changes observed in AUD patients can be detected in MRI using diffusion magnetic resonance imaging (dMRI). dMRI is an imaging technique based on the diffusion of water molecules under the influence of an external magnetic field. The outputs are variables quantifying the diffusivity of the water molecules in different directions. These variables are often considered to be representative of different aspects of the brain microstructure (axonal density, white matter integrity, etc.) and could help quantify the impact of alcohol consumption on the microstructure and predict behavioral changes.

In the past few years, more advanced models (such as NODDI, DIAMOND and microstructure fingerprinting) have been built upon these dMRI sequences to further characterize the microstructure. These models consider each voxel as a sum of different compartments, representing the different biological structures present in these voxels.
All these different models provide multiple metrics that represent different biological aspects of the microstructure. Selecting the metrics that best describe the evolution of a neuropathology is thus a challenge. Furthermore, not all brain regions display the same microstructural changes during alcohol withdrawal.

The goals of this thesis are to identify which metrics best describe the microstructural changes observed during abstinence in different brain regions, to identify which brain

regions are the most impacted and to compare the different microstructural changes that can be observed by each model.

This thesis is composed of two main parts: a summary of the theoretical backgrounds upon which the methods used to quantify the microstructural changes are built upon, and the application of those models in a real life case study.
The theoretical background covers two main subjects: the theory behind magnetic resonance imaging (MRI) and alcohol use disorder. The magnetic resonance background goes through the magnetic properties behind MRI, diffusion MRI and the models that can be used to extract metrics from the diffusion data. The changes observed with these metrics due to different patterns of alcohol consumption are then summarized.

The second part of this report focuses on the application of the diffusion-based models to a patient with alcohol use disorder and is structured as follows: the description of the methods used, the results and a discussion of those results. The method section describes the data processing pipeline used to get from the raw diffusion data, obtained from a patient before and after a two-week alcohol withdrawal period, to the metrics quantifying the resulting microstructural changes. Those changes are then compared throughout different brain regions in the results section. Finally, the last section is a discussion on the metrics that were found to be useful to highlight significant changes during abstinence and which of the analyzed regions displayed the highest number of metric variations. This last section also compares the microstructural changes observed by each model.
Lastly, this work concludes with the limitations of the analysis presented and the future steps that can be taken to improve the characterization of alcohol use disorder during abstinence via diffusion MRI.

Part I

Theoretical background

Chapter 1

Magnetic resonance imaging

The first part of this thesis covers notions that will come in useful to understand the terms used and the principles behind the methods employed throughout this report. This first chapter covers magnetic resonance imaging, diffusion magnetic resonance imaging and the models that can be implemented with this imaging technique.

1.1 Magnetic resonance imaging

Magnetic resonance imaging (MRI) is an imaging technique used to obtain a variety of images (anatomical, functional, etc.) of the body. Compared to computed tomography (CT) scans, MRI is often seen as a safer alternative for repeated scans as it does not produce any radiation.
MRI is a fairly recent technology. It was discovered by two teams, one led by Felix Bloch in Stanford and another led by Edward M. Purcell in Harvard. They received the Nobel Prize in physics for this discovery in 1952. The first human images were obtained in 1976. The development of MRI also led to a Nobel Prize in chemistry in 1991 and in medicine in 2003 [2].

1.1.1 Magnetic properties

MRI makes use of the magnetic properties of hydrogen to provide anatomical images. Below is a summary of the atomic magnetic properties MRI relies on.

Every atom nucleus presents a *spin*. This spin I can have different discrete values based on the atomic number Z and mass number A, for example

- If A is even and Z is even : I=0 (^{12}C,^{16}O)
- If A is odd and Z is odd : I=1/2 (^{1}H,^{13}C,^{15}N)
- If A is even and Z is odd : I=1 (^{2}H,^{14}N)

There is a high quantity of ^{1}H in the molecules present in biological tissues. It is estimated that up to a third of the atoms present in our organism are hydrogen

atoms. The large quantity of these hydrogen atoms as well as their intrinsic magnetic moment makes them a key element in MRI.

A rotating charged particle induces the creation of :

- An electric current,
- A magnetic field, characterized by a magnetic moment μ, aligned with its axis of rotation (see Fig.1.1). The axis of rotation is represented by the vector S.

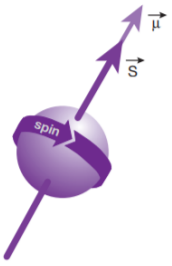

Fig 1.1: *Representation of the spin and the magnetic moment. From [2].*

Without the influence of external factors, such as a magnetic field, the magnetic moments of the molecules are randomly oriented. The sum of the resulting magnetic fields, in a large biological tissue sample, is thus null ($\sum \mu = 0$). However, when an exterior magnetic field B_0 is applied on the tissue, the individual orientations will align with the magnetic field either in a parallel (low energy state E_1) or anti-parallel (high energy state E_2) manner (see Fig.1.2). The resulting magnetic field is no longer null ($\sum \mu \neq 0$).

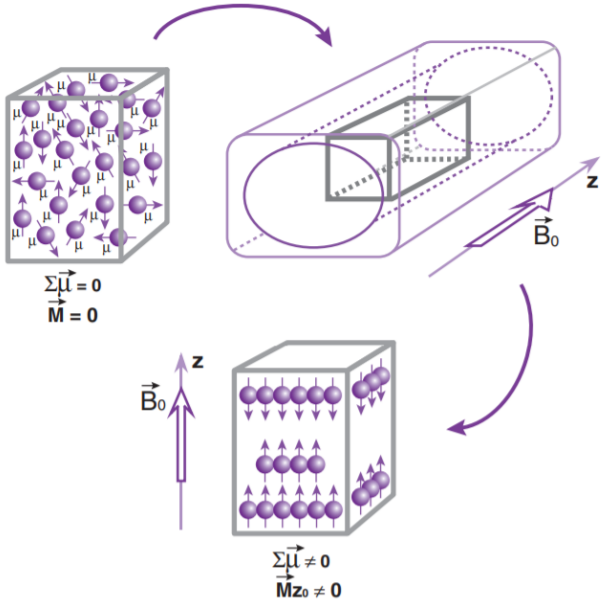

Fig 1.2: *Influence of external fields on the magnetic moment orientation. From [2].*

The magnetic moment μ in a magnetic field B_0 induces a *torque* $\Gamma = \mu x B_0$. Due to this torque, the protons are actually not perfectly oriented along the z axis, but are precessing in a "double-cone" manner, like a spinning top would under the influence of earth's gravity (see Fig.1.3).

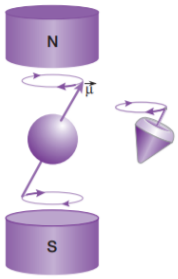

Fig 1.3: *Representation of the "double cone" movement. From [2].*

The frequency at which the axis rotates around the "cone" is called de Larmor frequency

$$\nu_0 = \frac{\gamma B_0}{2\pi}, \tag{1.1}$$

with γ being the gyromagnetic ratio, specific to each nuclei.
Under the influence of a magnetic field B_0, all the individual spin's magnetic moments lead to a macroscopic magnetisation

$$M = \frac{1}{V}\sum \mu_i. \tag{1.2}$$

This macroscopic magnetisation is discribed by the following formulas:

- $\Delta E = E_{down} - E_{up} = \hbar\gamma B_0 = h\omega_0$
- $M_0 = \frac{\gamma^2 h^2 \rho B_0 I(I+1)}{3kT}$

The state occupancy follows a Boltzmann distribution. The proportion of protons in each energy state is computed with the formula

$$\frac{N_{up}}{N_{down}} = e^{\gamma h B_0/kT}, \tag{1.3}$$

with N_{up} / N_{down} the proportion of parallel / antiparallel spins, γ the gyromagnetic ratio, $\hbar$ the Planck's constant / 2π, k the Boltzmann's constant, T the temperature [K] and B the intensity of static magnetic field [T]. [3]

If an RF pulse oscillating is applied at the Larmor frequency of the atom ($f_{RF} = f_0$), then the following equations are obtained:

- $B_1(t) = 2B_1(t)cos(2\pi f_{RF} t + \phi)1_{xy}$
- $M = M_z 1_z + M_{xy} 1_{xy}$

- $\omega_0 = 2\pi f_0$

The angular frequency around B_1 (Ox) is given by the formula [2] (see Fig.1.4)

$$\omega_1 = \gamma B_1. \tag{1.4}$$

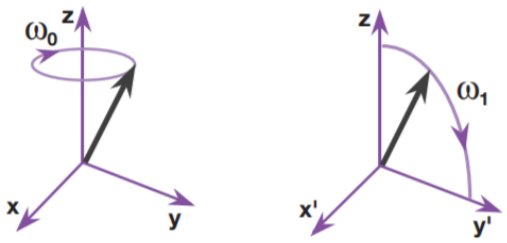

Fig 1.4: *Precession angular frequencies ω_0 and ω_1. From [2].*

In Fig.1.5 are displayed the two most common RF impulses: 90° and 180°.
After a 90° RF impulse (B), the protons in excess will go from a low energy state E_1 to a state with a high energy E_2, and the protons will be in phase. This decreases the M_z component and increases the M_{xy} component of the magnetization vector.
After a 180° RF impulse (C), the protons reach a high energy state E_2, inverting the direction of the the magnetization vector M_z.

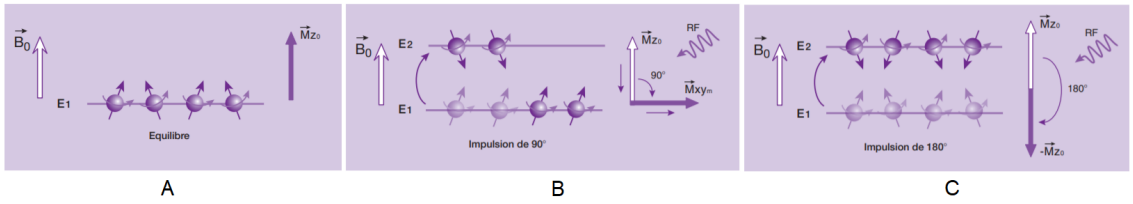

Fig 1.5: *A. Resting state; B. System after 90 RF impulse; C. System after 180 RF impulse. From [2].*

T1 relaxation

The T1 relaxation is also called spin-lattice relaxation or longitudinal relaxation. It is characterized by an exchange of energy between the spins in the system and the environment.
The relaxation of the longitudinal component of the magnetic field (M_z) is linked to T1 by the formula

$$M_z(t) = M_0 + (M_z(0) - M_0)e^{\frac{-t}{T1}}. \tag{1.5}$$

Following a 90° RF impulse, the longitudinal component becomes null due to the distribution of the spins between the energy levels E_1 and E_2. This state is unstable and will lead to a reverse transition from the high energy state E_2 to the low energy E_1.
This transition back to the equilibrium state will release energy. This energy will

be transferred to the network (spin-network relaxation) and the efficiency of this transfer will increase as the frequency of the molecular collisions ν_c gets closer to the Larmor frequency ν_0. When these two frequencies are similar, T1 will be short (high level of energy transfer). T1 will increase as the two frequencies differ from each other (see Fig.1.6).

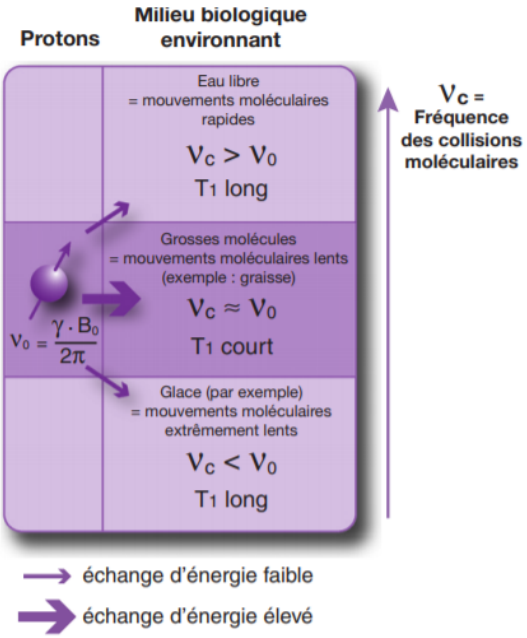

Fig 1.6: *Influence of surrounding tissue composition on energy exchange. From [2].*

The value of ν_0 can be increased with the external magnetic field B_0. The differences in frequency ν_c in the different tissues will lead to different responses. This type of sequence is called "T1-weighted".

T2 relaxation

The T2 relaxation is also called spin-spin relaxation or transversal relaxation. It is due to the fluctuations in the magnetic fields and inhomogeneities of B_0. It is characterized by a loss in coherence of the spin phases.

$$M_{xy}(t) = M_{xy}(0)e^{\frac{-t}{T2}} \tag{1.6}$$

The effective relaxation time also takes into account the inhomogeneities of B_0

$$\frac{1}{T_2^*} = \frac{1}{T_2} + \gamma \Delta B_0. \tag{1.7}$$

A 90^o RF impulse will also have an impact on the transversal component of the magnetic field M_{xy} due to a "rephasing" of the protons. The end of this RF impulse will display a quick dephasing of the protons, leading the transversal component to

become null once again.

The transversal magnetization follows a decreasing exponential with a T2 constant, characteristic of a specific tissue. T2 thus represents the transversal relaxation of a tissue. The longer T2 is, the longer the transversal magnetization persists. T2 values for biologic tissues (such as muscle, fat and grey matter) vary between 50 [ms] to 100 [ms] but the extreme values can range from nearly 0 [ms] (ice) to 2000 [ms] (ventricular Cerebro Spinal Fluid (CSF)) [4]. The T2 time depends on the molecular structure of the tissue as well as on the matter state (solid or liquid). T2 is longer in liquids compared to solids or tissues composed of large molecules, as illustrated in Fig.1.7. Sequences that use this difference in T2 to differentiate tissues are called "T2-weighted".

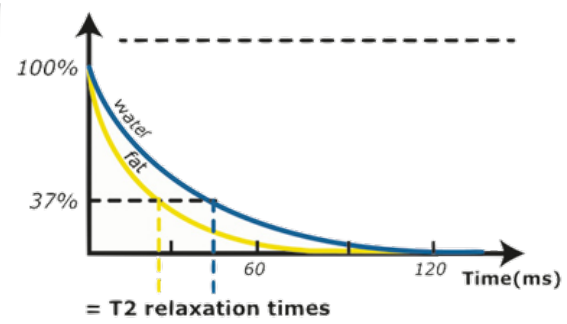

Fig 1.7: *T2 relaxation difference in water and fat.*

Bloch equations

The nuclear magnetization in each direction, depending on T1 and T2, can be computed using a set of macroscopic equations known as the Bloch equations: [5]

- $\frac{dM_x}{dt} = -\frac{M_x}{T_2} + \Delta\omega M_y - \gamma B_{1y} M_z$
- $\frac{dM_y}{dt} = -\Delta\omega M_x - \frac{M_y}{T_2} + \gamma B_{1x} M_z$
- $\frac{dM_z}{dt} = \gamma B_{1y} M_x - \gamma B_{1x} M_y + \frac{M_0 - M_z}{T_1}$

With γ being the gyromagnetic ratio.

1.1.2 Spin-echo sequence

One of the first sequence developed in MRI was the spin-echo sequence, as represented in Fig.1.8. It is composed of a 90° followed by a 180° RF impulse.
There are two main parameters in a spin-echo sequence :

- Echo time (TE): length of time between the RF impulse and the first echo,
- Repetition time (TR): length of time between two 90^o RF impulses.

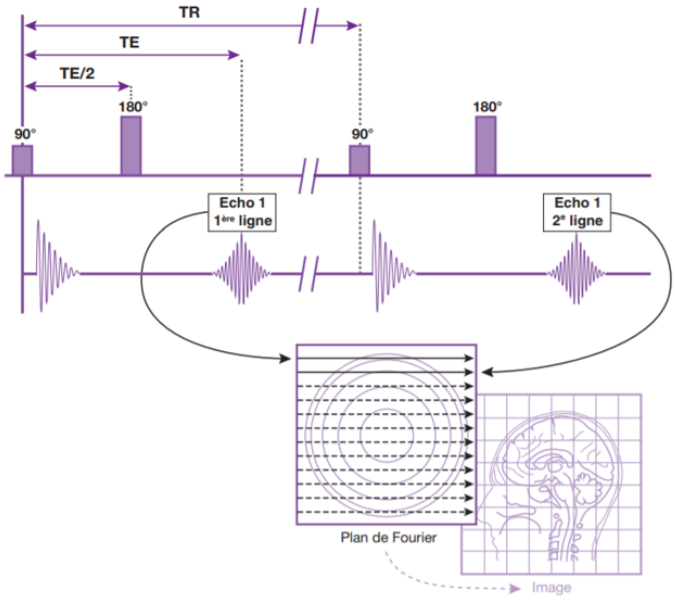

Fig 1.8: *Spin echo sequence and Fourier space. From [2].*

T1 contrast

To get a scan with a strong T1 contrast, both the TR and TE must be short. This allows to highlight the difference in T1 relaxation in the different tissues while keeping the T2 contribution to a minimum, as shown in Fig.1.9. In these scans, the white matter is represented in light grey, the grey matter in a darker shade of grey and the fluids in black.
T1-weighted images are thus useful to distinguish white matter from grey matter and to highlight anatomical landmarks on a macroscopic scale. The anatomical images used in this thesis were T1-weighted and were used to segment different brain regions (see Section 3.2 for more information on how the anatomical images were used).

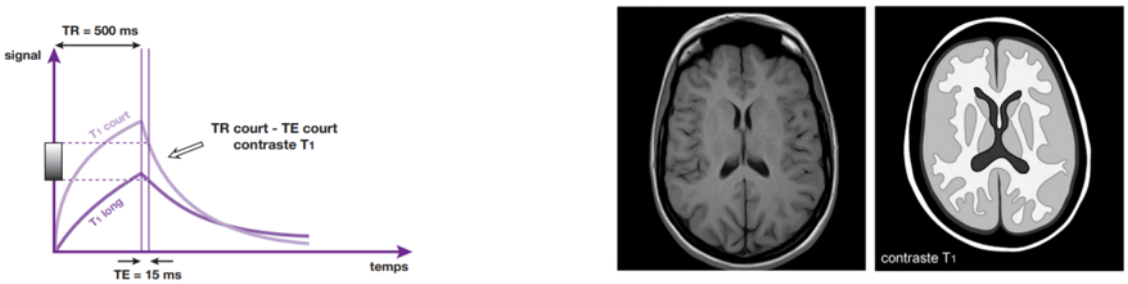

Fig 1.9: *T1 contrast. Adapted from [2].*

T2 contrast

Similarly, it is possible to get a scan with a strong T2 contrast with a long TR and long TE, as displayed in Fig.1.10. In these images the white matter is in dark grey, the grey matter is in light grey and the cerebrospinal fluid is in white.

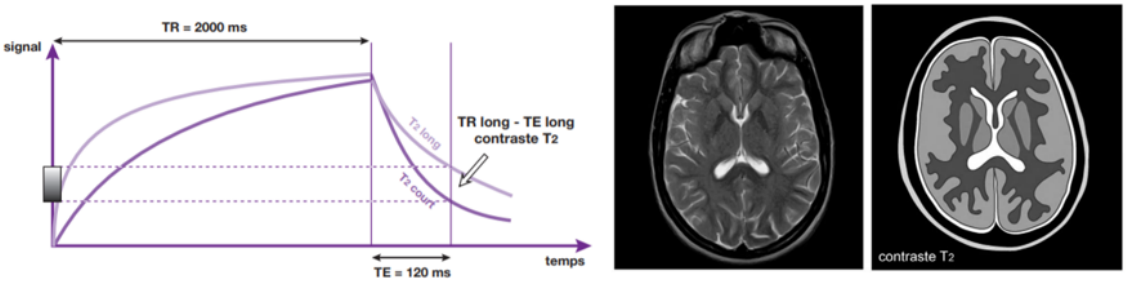

Fig 1.10: *T2 contrast. Adapted from [2].*

Proton density contrast

If both a long TR and a short TE are selected, the difference in relaxation time is no longer the main parameter of contrast in the image. With these settings, the tissues with a higher proton density will display a stronger signal, as illustrated in Fig.1.11. The grey matter appears as light grey, the white matter as grey and the cerebrospinal fluids appear in a darker shade of grey.

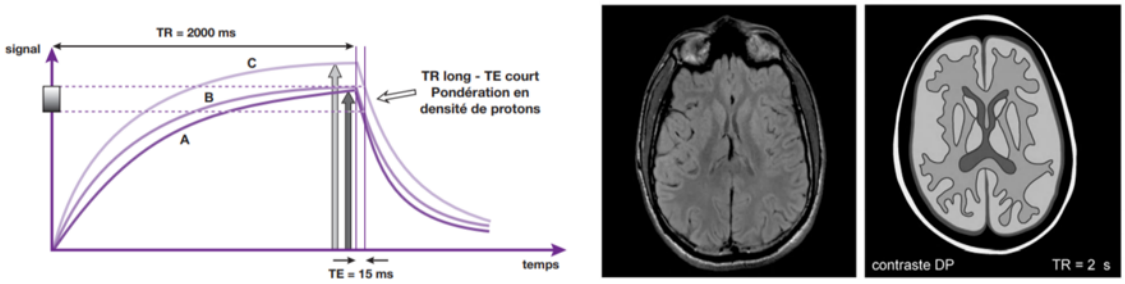

Fig 1.11: *Proton density contrast. Adapted from [2].*

1.1.3 Artefact types

MRI images are susceptible to artefacts due to the magnetic properties it relies on, and the duration of the sequences used. This section covers some of the most common artefacts found in MRI.

The duration of a MRI scan can vary between a few minutes up to an hour based on the type of sequence used and the resolution of the image. This large time window makes it difficult for patients to stay completely immobile, artefacts due to movement are thus common. The causes of **movement artefacts** can be separated into two categories: random and periodic movements. The amount of random movements can be reduced by decreasing the scan time. There is thus a trade-off between the precision of the scan and the amount of random movements. The periodic movements create "ghost images" (i.e. structures present in the image that are mislocated and/or appear multiple times, shown in Fig.1.12-A), their impact on the image can be reduced with *gating*. Some programs such as *FSL* or *ExploreDTI* also provide movement correction algorithms (the use of these programs will be detailed

in Section 3.2.1), where the different scans obtained during the sequences are registered to each other in order to compensate for the changes in position of the patient.

The **magnetic susceptibility** of certain materials can interfere with the imaging process. Metallic implants or dental work can create local inhomogeneities in the magnetic field which will result in distortion artefacts (shown in Fig.1.12-B). The resulting image will be distorted and the tissue surrounding the implant will not be accurately represented. A solution to these types of artefacts is to use different parameters for the spin-echo sequence, such as a shorter TE.

Aliasing artefacts, also known as folding-over or wrap-around artefacts, are often characterized by the edges of the images being folded over (shown in Fig.1.12-C) but can also occur in-between slices. They are due to an inadequate field of view (FOV) and can thus be removed by increasing the FOV or using an anti-aliasing software.

Gibb's artefact , also known as Gibb's truncation or Gibb's ringing, is characterized by parallel lines along the edges of high-contrast interfaces (shown in Fig.1.12-D). This phenomenon is a consequence of the use of Fourier transforms to reconstruct the MR signal. Increasing the matrix size reduces the truncation artefact. However, this results in a decrease of both the voxel size and the signal to noise ratio. As a consequence, even if truncation artefacts are still present, they can be masked by the image noise.

The **chemical displacement** or chemical shift, is characterized by artefacts at the interface between tissues of a different composition such as fat and water (shown in Fig.1.12-E). The different resonance frequencies of the adjacent tissues causes a spacial misregistration of the molecules. Possible solutions are to use fat-suppressed imaging, decrease the field strength or increase the magnetic gradient.

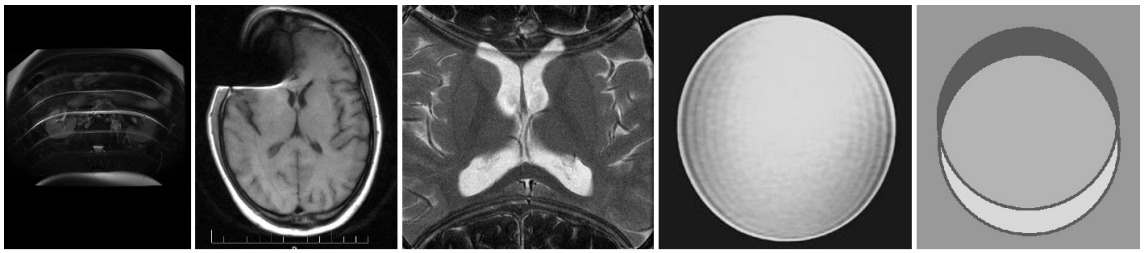

Fig 1.12: *MRI common artefacts: periodic motion (A); magnetic susceptibility (B); aliasing (C); Gibb's ringing (D); chemical shift (E). Adapted from [6].*

Finally, **Eddy currents**, also known as Foucault currents, are also known to create artefacts. Faraday's law of induction states that a changing magnetic field induces electrical currents in nearby conductors. MRI thus creates these Eddy currents in the body, which in turn generate their own magnetic fields, resulting in a distortion of the magnetic field. Correcting the Eddy currents is especially important for MRI sequences using large and frequent changes in the main magnetic field, such

as diffusion MRI. The objectives and functioning principles of diffusion MRI are detailed in the section below.

1.2 Diffusion-Weighted MRI (DW-MRI)

Other sequences were developed in MRI to make use of other properties such as the restricted diffusion of water molecules under a magnetic field.
This section describes the sequences and models used in Diffusion-Weighted MRI (DW-MRI), also known as Diffusion Weighted Imaging (DWI) or diffusion MRI (dMRI).
The main sequence used diffusion MRI is the Pulse Gradient Spin Echo (PGSE) sequence and its variations.
Two of the most commonly used models are the diffusion tensor model and diffusion kurtosis model. These models also allow for a visual representation of the fiber tracts known as tractography.

1.2.1 Pulse Gradient Spin Echo (PGSE)

A Pulse-Gradient Spin Echo (PGSE) sequence is composed of two magnetic gradients centered around a 180^o RF impulse. These gradients allow the characterization of some microstructural properties of the tissue volume, which would usually be out of reach with classic spin echo (SE) sequences [7]. The images obtained with DW-MRI give out information about the diffusion of the water molecules in the tissue structure by displaying a specific intensity for each voxel based on the observed diffusivity.

After the first RF pulse, a first magnetic gradient is applied. This gradient will dephase the magnetization. The second gradient, which is applied after the seond RF pulse, will rephase the magnetization (see Fig. 1.13) [8].

The PGSE sequence is defined by several parameters:

- Δ : the time between the onset of the two gradients,
- δ : the duration of application of a gradient,
- $\mathrm{g} = \mathrm{G}\hat{\mathrm{g}}$: G is the gradient intensity and $\hat{\mathrm{g}}$ represents the direction of application of said gradient.

These parameters can be combined into a single value, called 'b-value', which characterizes the PGSE sequence

$$b_{PGSE} = (\gamma G \delta)^2 (\Delta - \frac{\delta}{3}) \ [s/mm^2]. \tag{1.8}$$

If water molecules diffuse between the application of the two gradients, then they will not be correctly rephased by the second gradient and the intensity of the echo obtained will be reduced. The distance traveled by the water molecules will then depend on the time between the two gradients Δ and also the applied gradient

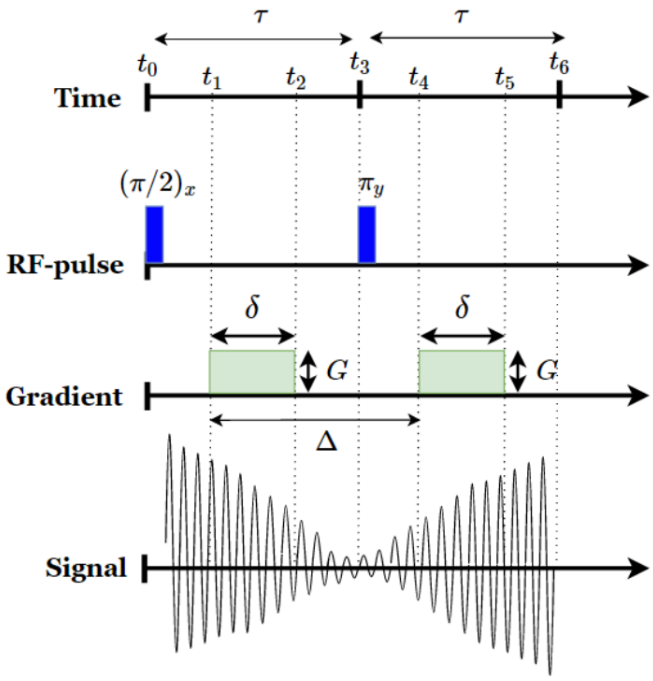

Fig 1.13: *PGSE sequence. From [8].*

intensity. The reduction in intensity due to diffusion is illustrated in Fig.1.14 [9]. On the figure's first line, each molecule stays in its place and will thus experience a rephasing gradient corresponding to their dephasing gradient. However, if the molecules are displaced, the gradients do no longer correspond and the molecules are out-of-phase following the application of the second gradient. The output signal will then be reduced.

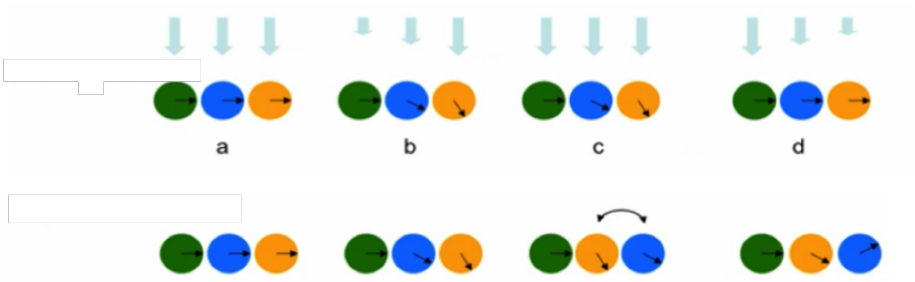

Fig 1.14: *Application of a gradient with (top) and without (bottom) diffusion. From [9].*

The diffusion of the water molecules in the brain can then be characterized by the reduction in intensity of the recorded signals. This diffusion can be affected by numerous factors such as the composition of the tissue, the type of molecules present or the temperature [7]. Images obtained with DW-MRI show a difference in contrast when the diffusion varies in the different structures. For example, in the cerebrospinal fluid (CSF), since the water molecules are free to move around, the intensity loss will

be more noticeable than in a structure with reduced diffusivity. The output signal is thus darker in regions with high diffusivity, such as the CSF, and lighter in regions of low diffusivity, such as grey matter (illustrated in Fig.1.15).

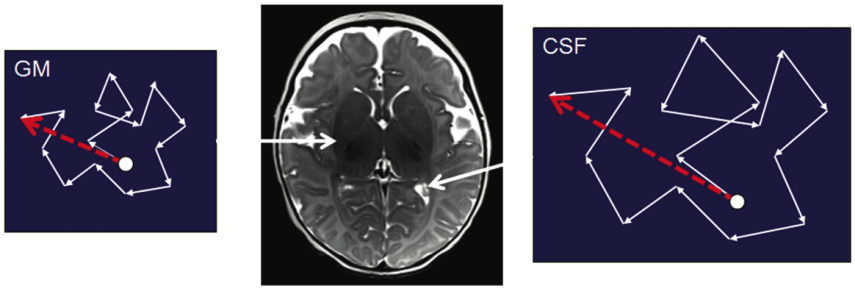

Fig 1.15: *Graphical representation of the movement of water molecules in the CSF (right) and grey matter (left). From [7].*

The diffusion of the water molecules is highly dependent on the shape of the microstructure. For example, the diffusivity of a water molecule in an axon will be higher along the direction of the axon compared to a direction perpendicular to it. The diffusion can then be represented by an ellipse, with the preferred direction of diffusion being represented on the larger axis. The diffusion is said to be anisotropic. On the other hand, if the diffusion is not impacted by the microstructure, such as in the CSF, then it will represented by a sphere (see Fig.1.16). The diffusion is then called isotropic [7].

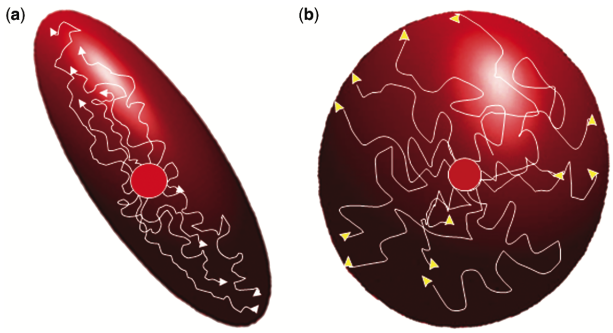

Fig 1.16: *Anisotropic diffusion (a), Isotropic diffusion (b). The arrows represented the possible movements of molecules. From [7].*

In order to obtain some information about the preferred direction of diffusion of the water molecules, the applied gradients have a varying orientation. The loss of signal due to the free diffusion of the water molecules can be described by an exponential law, called Stejskal-Tanner equation [10]

$$E(R^n) = e^{-b_{pgse}\hat{g}^T D\hat{g}} \text{ (anisotropic case)} = e^{-b_{pgse}D} \text{ (isotropic case)}, \tag{1.9}$$

with:

- D : the apparent diffusion coefficient,
- b_{PGSE} : the b-value.

The signal attenuation is described by the coefficient E. It represents the ratio between the observed signal when a diffusion signal is applied (with a b-value of 1000 [s/mm^2], for example) and the base signal (without a diffusion gradient and with an equivalent b-value of 0 [s/mm^2]) [11]. For DW-MRI, the D coefficient is estimated by solving the Stejskal-Tanner equation, after the measures with and without a diffusion gradient have been recorded. For homogeneous tissues presenting an isotropic diffusion, the diffusion coefficient is the same in every direction. For most biological tissues however, the microstructure present in those tissues often makes them heterogeneous. The diffusion coefficient will then depend on the orientation of the applied gradient.
This coefficient, also called apparent diffusion coefficient (ADC), is often used to obtain scalar maps representing the diffusion of a specific b-value. The ADC can be obtained with the formula

$$ADC = -log(\frac{S(b)}{S_0})/b, \tag{1.10}$$

with:

- $S(b)$: signal with a b-value of b
- S_0 : signal with a b-value equal to zero
- b : the b-value

1.2.2 Diffusion Tensor Imaging

By combining specific Diffusion MRI (dMRI) sequences with a diffusion tensor model, Diffusion Tensor Imaging (DTI) is obtained.
DTI allows the study of the tridimensionnal diffusion of water molecules. Contrarily to the images displaying the ADC (obtained with classic dMRI), where the diffusion coefficient was a scalar, the coefficients obtained with DTI are diffusion tensors. A minimum of 6 orientations are required to estimate the diffusion tensor. Indeed, the tensor is symmetric and is defined as

$$\mathbf{D} = \begin{pmatrix} D_{xx} & D_{xy} & D_{xz} \\ D_{yx} & D_{yy} & D_{yz} \\ D_{zx} & D_{zy} & D_{zz} \end{pmatrix}. \tag{1.11}$$

A DTI sequence is thus at least composed of 6 PGSE sequences with different orientation gradients as well as sequences with a very low b-value, in order to get a reference signal (without a diffusion gradient). The elements of $\mathbf{D}$ on its diagonal represent the diffusion coefficients along the three principal directions. Once the diffusion tensor is obtained, it becomes possible to use the eigenvalues of the tensor to represent interesting properties of cerebral tissues. The eigenvalues are defined by the Λ matrix

$$D = E \cdot \Lambda \cdot E^{-1}, \tag{1.12}$$

with E being the eigenvectors matrix and Λ the eigenvalues matrix

$$\mathrm{E} = \begin{pmatrix} e_{1x} & e_{2x} & e_{3x} \\ e_{1y} & e_{2y} & e_{3y} \\ e_{1z} & e_{2z} & e_{3z} \end{pmatrix}, \Lambda = \begin{pmatrix} \lambda_1 & 0 & 0 \\ 0 & \lambda_2 & 0 \\ 0 & 0 & \lambda_3 \end{pmatrix}.$$

Scalars derived from DTI

The trace is an information used in clinic representing the diffusion in each voxel. It is computed with the following formula [12]

$$Tr(D) = \lambda_1 + \lambda_2 + \lambda_3 = D_{xx} + D_{yy} + D_{zz}. \tag{1.13}$$

The mean diffusivity (Mean Diffusivity (MD)) can be computed from the mean of the eigenvalues of the diffusion tensor [12]

$$MD = \frac{Tr(D)}{3} = \frac{\lambda_1 + \lambda_2 + \lambda_3}{3} = \frac{D_{xx} + D_{yy} + D_{zz}}{3}. \tag{1.14}$$

The diffusivity can also be divided in a axial component (Axial Diffusivity (AD)) and a radial component (Radial Diffusivity (RD))

$$AD = \lambda_1, \tag{1.15}$$

$$RD = \frac{\lambda_2 + \lambda_3}{2}. \tag{1.16}$$

It is also possible to compute the fractional anisotropy (FA). This variable is the most common measure of anisotropy [11]. It is computed with the formula [12]

$$FA = \sqrt{\frac{3}{2}} \frac{\sqrt{(\lambda_1 - MD)^2 + (\lambda_2 - MD)^2 + (\lambda_3 - MD)^2}}{\sqrt{\lambda_1^2 + \lambda_2^2 + \lambda_3^2}}. \tag{1.17}$$

Or, equivalently

$$FA = \sqrt{\frac{1}{2} \frac{(\lambda_1 - \lambda_2)^2 + (\lambda_2 - \lambda_3)^2 + (\lambda_3 - \lambda_1)^2}{\lambda_1^2 + \lambda_2^2 + \lambda_3^2}}. \tag{1.18}$$

The FA values are contained between 0 and 1. A FA value of 0 means that all eigenvalues are equal $\lambda_1 = \lambda_2 = \lambda_3$ and that the diffusion is perfectly isotropic. In this case, as mentioned previously, the diffusion can be represented with a sphere. When the eigenvalues differ greatly, the FA value will tend to 1. The image obtained is called a "FA map" and represents the FA values in different shades of grey, see Fig.1.17-Left.

Colors derived from DTI

An RGB image can also be displayed with each color (red, green and blue) representing one of the three principal direction of diffusion of the diffusion tensor, see Fig.1.17-Right. These colors are a useful tool to quickly get an idea of the orientation of the diffusion tensors found by the diffusion tensor model.

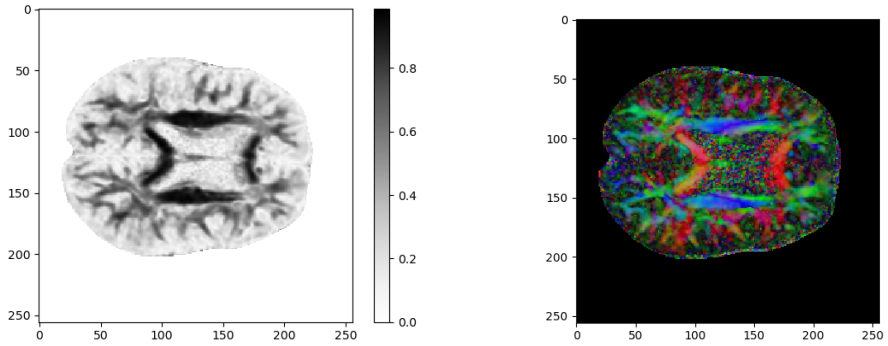

Fig 1.17: *Scalar measures derived from DTI: the FA image (left) and the corresponding colors from the principal directions (right).*

Glyphs derived from DTI

3D elements can also be used to visually characterize the information obtained on the diffusion of water molecules with DTI [11], as represented on Fig.1.18. These elements are glyphs and represent the principal orientation of the eigenvalues.

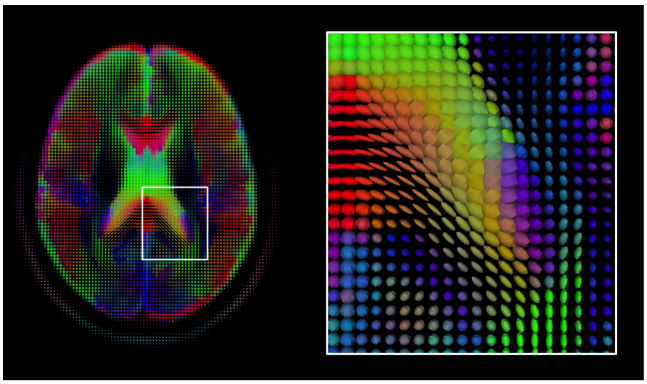

Fig 1.18: *Visualisation of DTI with glyphes and colors. From [13].*

Limitations of DTI

One of the main limitation of DTI is that water molecules are expected to follow a Gaussian distribution (non restrained diffusion) [12]. DTI also does not take into account the impact of multiple fibers crossing each other in a single voxel. If two

directional fibers are crossing each other perpendicularly, the resulting FA value will be null, which does not reflect the biological structure accurately. Several complex structures with different properties (axon radius, orientation, density, etc.) can also present the same Fractional Anisotropy (FA) value [12]. DTI models are phenomenological and not microstructural models and as such, do not give precise information about the microstructure.

1.2.3 Diffusion Kurtosis Imaging

Diffusion Kurtosis Imaging (DKI) expands on DTI and allows to quantify the non-Gaussian water diffusion with a kurtosis tensor. It was first developed by Jensen & al. in 2005 [14], DKI provides an estimate for the excess kurtosis of the diffusion displacement probability distribution, which is a metric of how much the diffusion differs from a normal distribution. It is considered to be a measure of the amount of tissue structure in a voxel, such as cellular compartments and membranes.
The kurtosis model defines the diffusion-weighted signal as

$$S(n, b) = S_0 e^{bD(n)+\frac{1}{6}b^2 D(n)K(n)}, \tag{1.19}$$

with:

- S_0 : the signal in the absence of a diffusion gradient,
- b : the b-value,
- $D(n)$: the diffusion along direction n,
- $K(n)$: the kurtosis value along direction n.

Other models have been built upon DKI. One of those model is mean signal diffusion kurtosis imaging (MSDKI) by Neto Henriques [15]. MSDKI is used to obtain a characterization of non-Gaussian diffusion independently of the degree of fiber organization. Indeed, "classic" DKI measures are impacted by properties such as fiber dispersion or the intersection angle of crossing fibers.

Another model is the white matter tract integrity (WMTI) model by Fiermans & al. [16]. WMTI is built upon DKI, it is used to estimate the contribution of hindered and restricted diffusion of well-aligned fibers. The metrics output by WMTI can be interpreted as the impact of intra- and extra-cellular compartments and could be used to estimate the axonal volume fraction and extra-cellular tortuosity. These measures could be used to distinguish processes of axonal loss from processes of myelin degeneration, according to [16].

1.2.4 Tractography

From the directional information and the diffusivity, it is possible to estimate the white matter tracts, by hypothesising that adjacent voxels presenting a similar orientation have a high chance of belonging to the same white matter fiber. Using

reconstruction algorithms, it is possible the build the white matter tracts, as illustrated in Fig.1.19.

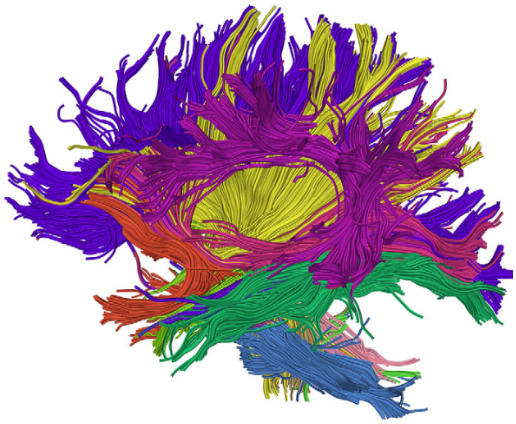

Fig 1.19: *White matter tracts obtained with DTI tractography. The colors were assigned with segmentation methods and atlases. From [7].*

1.3 Microstructural models

This section describes three microstructural models based on diffusion MRI. These models go further than classic models, such as DTI, by modeling the response of each voxel with multiple compartments. The individual voxels are no longer considered as a homogeneous volume with a unique signal response but as a sum of different compartments representing the microstructure inside the voxel.

1.3.1 NODDI

Neurite orientation dispersion and density imaging (NODDI) is based on diffusion MRI and claims to estimate the microstructural complexity of dendrites and axons.

As mentioned in the previous sections, DTI has two main limitations. First, DTI makes the hypothesis that the water molecule diffusion follows a Gaussian distribution. However, water molecule diffusion in actual living tissue is restricted by cell membranes and organelles, thereby showing a non-Gaussian distribution of displacement. Secondly, the interpretation of DTI parameters, such as fractional anisotropy (FA) and mean diffusivity (MD), which are thought to reflect biological microstructure (such as axonal integrity, white matter damage or axonal swelling) is rather difficult [17].

NODDI is an alternative proposed by Zhang & al. [17] to overcome these limitations. NODDI assumes a three-compartment tissue model including intracellular, extracellular, and cerebrospinal fluids in a single voxel. This enables the quantification

of the direction and structure of neurites (axons and dendrites) with a orientation-dispersed cylinder model and a Watson distribution. The parameters available as output of NODDI include the intracellular volume fraction, indicating neurite density, and the orientation dispersion index indicating the neurite orientation dispersion [17].

The three tissue models

The three tissue model is represented by the equation

$$A = (1 - \nu_{iso})(\nu_{ic}A_{ic} + (1 - \nu_{ic})A_{ec}) + \nu_{iso}A_{iso}, \tag{1.20}$$

with ν representing the volume fractions and A representing the normalized signal for the intra-cellular ($_{ic}$), extracellular ($_{ec}$) and CSF ($_{iso}$) compartments [17].

Intracellular

The response of the intracellular tissue is modeled as a set of sticks with a radius equal to 0. These sticks were chosen to represent the limited perpendicular diffusion of the neurites, expressed as

$$A_{ic} = \int_{S^2} f(n)e^{-bd_s(q.n)^2}dn, \tag{1.21}$$

with q the gradient direction and b the b-value of diffusion weighting. $f(n)dn$ gives the probability of finding sticks along the orientation n and $e^{-bd(q.n)^2}$ gives the signal attenuation due to unhindered diffusion along a stick with intrinsic diffusivity d_s and orientation n.

The orientation distribution function is modeled with a Watson distribution

$$f(n) = M(\frac{1}{2}, \frac{3}{2}, \kappa)^{-1}e^{\kappa(\mu.n)^2}, \tag{1.22}$$

with M being a confluent hypergeometric function, μ the mean orientation and κ the concentration parameter that measures the extent of orientation dispersion about μ.

Displayed in Fig.1.20, is the representation of a Watson distribution on the surface of a sphere, with increasing κ from left to right.

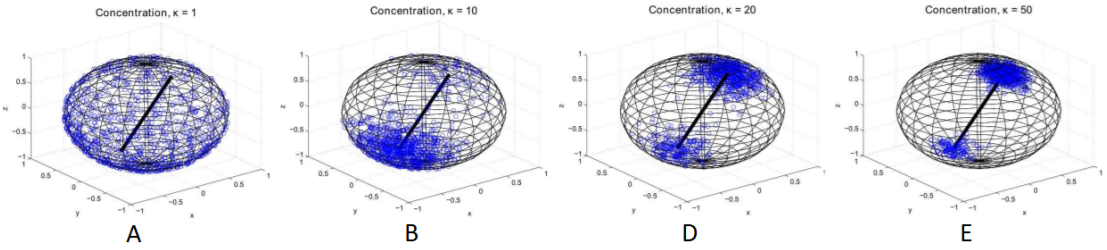

Fig 1.20: *Illustration of the Watson distribution. Adapted from [18].*

NODDI outputs a metric called the **orientation dispersion index (ODI)**, which is linked to κ by the formula

$$ODI = \frac{2}{\pi} arctan(1/\kappa). \tag{1.23}$$

Extracellular

The extracellular tissue model represents the space around the neurites with a hindered (but not restricted) diffusion. The model used is a Gaussian anisotropic distribution, expressed as

$$A_{ec} = e^{-bq^T(\int_{S^2} f(n)D(n)dn)q}, \tag{1.24}$$

with $D(n)$ being a cylindrically symmetric tensor with the principal direction of diffusion n, diffusion coefficients $d_{//}$ parallel to n and d_{per} perpendicular to n.

The following equation links the two diffusion coefficients $d_{per} = d_{//}(1 - \nu_{ic})$.

CSF

The CSF compartment models the space occupied by cerebrospinal fluid and is modeled as an isotropic Gaussian diffusion with diffusivity d_{iso}.

1.3.2 DIAMOND

The goal of this model is to describe the tridimensionnal diffusion in each voxel from the signal obtained from each tissue compartments. The obtained signal comes from the different microstructural environments (cell shape, orientation, extra-cellular space, etc.). The DIAMOND model (DIstribution of 3D Anisotropic MicrOstructural eNvironments in Diffusion-compartment imaging) is an extension of the model described by Yablonskiy et al. [19]. In the DIAMOND model, homogeneous 'spin-packets' are considered. The signal obtained comes from those 3D 'spin packets' and each voxel contains heterogeneous populations of 'spin-packets'. The diffusivity of each homogeneous 'spin-packet' is modeled by a diffusion tensor D and represents a 3D Gaussian diffusion. The signal obtained in each voxel being the sum of each 'spin-packet', the signal can be defined as

$$S_k = S_0 \int_D P(D) e^{-b_k g_k^T D g_k} dD, \tag{1.25}$$

with :

- S_k : The obtained diffusion signal,
- S_0 : The signal without diffusion gradient,
- $P(D)$: Distribution matrix giving the spin packet fraction defined by a 3D diffusion tensor in a voxel.

If a voxel is considered as an homogeneous microstructural environment characterized by a diffusion tensor $\mathbf{D}^0$, then P(D) is a 'delta' function such as : $P(D) = \delta(D - D^0)$. In this case, the DIAMOND model corresponds to a DTI model.
However, if a voxel presents several different homogeneous microstructural environments, the P(D) distribution is then composed of several delta functions, as represented in Fig.1.21. This is equivalent to a multi-tensor model, as described by Tuch & al. [20]

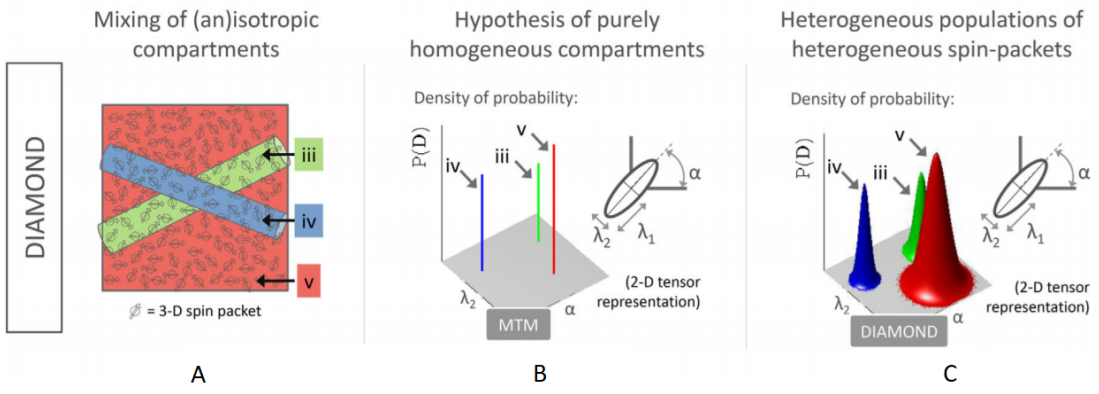

Fig 1.21: *Illustration of the microstructural environments in the DIAMOND model (A) isotropic compartments (red) and anisotropic compartments (blue and green); (B) homogeneous compartments ; (C) heterogeneous populations. Adapted from [21].*

DIAMOND uses the matrix-variate Gamma (mv-Γ) distribution to define P(D). The formal definition of the mv-Γ distribution is given hereafter [21]

$$P_{\kappa,\Sigma}(D)\,\frac{|D|^{\kappa-(p+1)/2}}{|\Sigma|^{\kappa}\Gamma_p(\kappa)}e^{Tr(\Gamma^{-1}D)}, \tag{1.26}$$

with :

- κ : The distribution shape parameter, the density becomes more concentrated around D_0 as κ increases. The more homogeneous the compartments, the higher the κ parameter.
- Σ : The scaling parameter.
- $\Gamma_p(\kappa) = \pi^{p(p-1)/4}\prod_{j=1}^{p}\Gamma\left(\kappa - \frac{j-1}{2}\right)$, the multi-variate gamma function.

A population presenting a narrow peak means the population is homogeneous while a large peak represents a heterogeneous population. If N_p spin packets populations are considered and by representing the composition of each population by a mv-Γ distribution written $P_{\kappa_j,\Sigma_j}(D)$, the distribution of the voxel is obtained

$$P(D) = \sum_{j=1}^{N_p} f_j P_{\kappa_j\Sigma_j}(D), \tag{1.27}$$

with:

- $\sum_{j=1}^{N_p} f_j = 1$
- f_j : The occupation fraction

To summarise, the DIAMOND model uses 3D spin packets modeled by the 'matrix-variate Gamma' (mv-Γ) distribution. This model allows to model the compartments where the diffusion is either isotropic or anisotropic. The existence of several compartments in a voxel is thus considered, taking into account the heterogeneities of each compartment. This model has limitations such as the fact that the number of spin packets (N_f) has to be known.

1.3.3 Microstructure fingerprinting

A model developed by Rensonnet G. [10] combines Monte Carlo simulations with dictionary matching to find which parameters best describe the underlying microstructure in each voxel. Similarly to the DIAMOND model, each voxel is considered to be composed of different structures (such as fascicles and an extra-axonal compartment).

A dictionary is generated using a large number of Monte Carlo simulations performed for various possible combinations of tissue parameters (see the right side of Fig.1.22). These parameters include the radius of the cylinders representing the axons, the fiber volume fraction in those cylinders, the extra-axonal diffusivity, etc. Each column of the created dictionary (a_x in Fig.1.22) is thus a fingerprint uniquely related to the underlying microstructural configuration in a voxel.
Each voxel is then matched separately, using a robust pattern matching algorithm, to the fingerprint –or combination of fingerprints– that best explains the signal y (the input diffusion data of the patient, see the left side of Fig.1.22). The obtained fingerprints then provide the associated tissue parameters.
Looking at the example in Fig.1.22, the signal y would be best approximated by the fascicles a_1 and a_5 with each column representing a fraction α and β of the signal, respectively.

The microstructure fingerprinting model makes use of the superposition approximation for DW-MRI signals in the presence of multiple fascicles. The signal arising from crossing fascicles is considered to be equal to the sum of the signals arising from each fascicle independently.

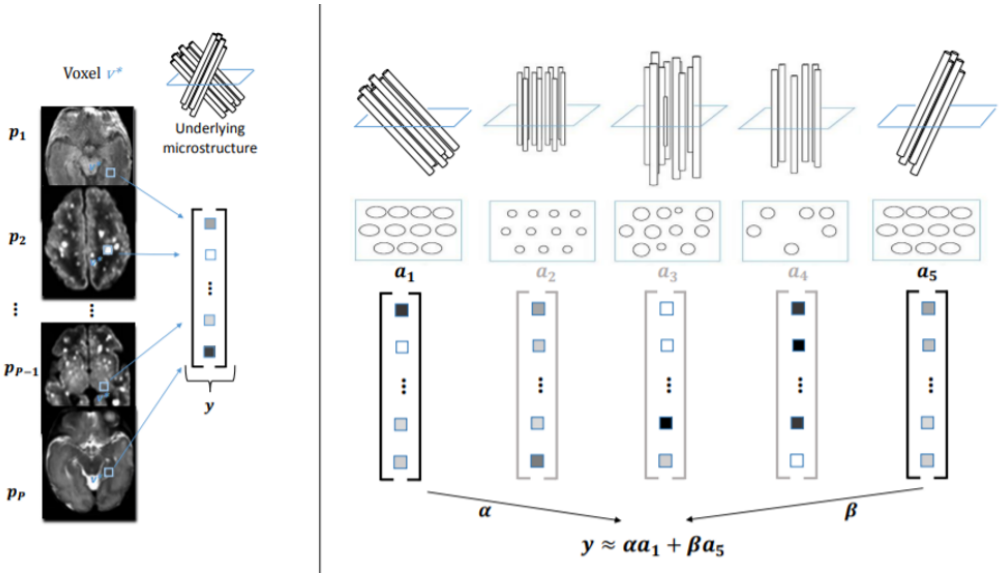

Fig 1.22: *Rensonnet Fingerprint summary. From [22].*

Chapter 2

Alcoholism

This second chapter covers the Alcohol Use Disorder (AUD), the biological impact of alcoholism on the brain as well as a literature review on the observed effects of alcohol consumption on the brain microstructure using diffusion MRI.

2.1 The biological impact of Alcohol Use Disorder

Alcoholism, also known as alcohol use disorder (AUD), is a broad term for any drinking of alcohol that results in mental or physical health problems [23].
Alcohol-dependence is a widely spread disorder that is estimated to be present in 5–7% of the population of developed countries [24]. It is also one of the principal causes of mortality with about 3.3 million deaths (5.9% of all deaths) being attributed to alcohol each year.
Since AUD impacts both the mental and physical health of the patient, it becomes difficult to treat as mood and cognition alterations play a role in the motivation for alcohol-drinking [24]. The AUD patients also have to deal with a “Kindling effect”. Due to neuroadaptions, each subsequent abstinence period without alcohol consumption leads to a withdrawal syndrome more severe than the previous withdrawal episode [23].

de Timary & al. [1] have identified a pathway leading the neuro-inflammation observed in AUD patients. The process, displayed in Fig.2.1 is done through a biological pathway called "leaky-gut".
Chronic alcohol abuse alters the composition of the gut microbiota, changing its permeability and allowing bacterial components to pass through the gut membrane and reach the systemic circulation. These gut-derived bacterial products are recognized by the immune cells circulating in the blood or residing in target organs, which release pro-inflammatory cytokines in response. These circulating cytokines are considered important mediators of the gut–brain communication, as they can reach the central nervous system and induce neuro-inflammation that is associated with change in mood, cognition and drinking behavior. The inflammatory cytokines also damage the blood-brain barrier (BBB) [1].

This leads us to the changes in microstructure observed in AUD patients which

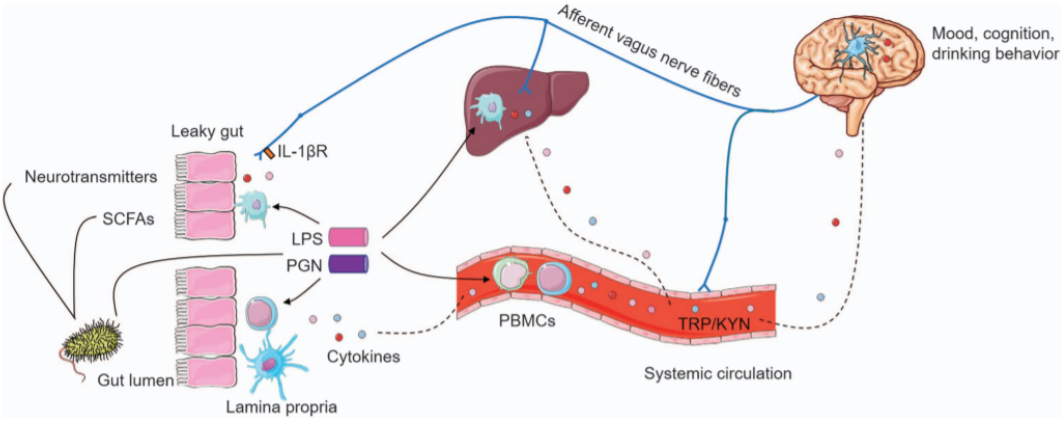

Fig 2.1: *Pathway leading to neuro-inflammation due to "leaky-gut". LPS and PGN : Gut-derived bacterial components. SCFAs : short-chain fatty acids. IL-1βR is a receptor which conveys the peripheral inflammatory message to the CNS. PBMCs : peripheral blood mononuclear cells.TRP/KYN : tryptophan/kynurenine. From [1].*

could be detected by MRI models such as DTI, NODDI [17], DIAMOND [21] and microstructure fingerprinting [10].
The first microstructural change that could be measured involves the microglia. Microglia are glial cells which represent 10 to 15% of all brain cells [25], they play a role in the central nervous system (CNS) immune system and in the brain maintenance. They are highly reactive to their environment and can be found in two states: in a "resting state" (Fig.2.2-left) or activated (Fig.2.2-right).

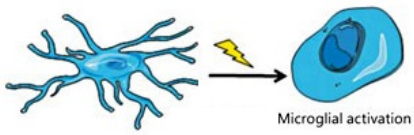

Fig 2.2: *Morphological change in microglia after activation. From [25].*

The change in morphology of microglial cells is expected to be translated into an value change of several metrics, such as a loss of fractional anisotropy. The mean diffusivity should also be impacted as the diffusion of molecules changes with the shape of the cell in which they are contained.
Several studies have associated AUD and morphological changes of the microglia, notably with positron emission tomography (PET) through the use of radioligands binding to a protein highly expressed in activated glial cells. "Pre-clinical models of alcohol dependence demonstrate microglial activation and expression of inflammatory mediators [...] These changes are associated with neuronal death and learning deficits" [26].

Mircostructural changes are also expected to appear in axons such as the one displayed in Fig.2.3. Since alcohol use induces a loss of mainly small fibers, myelin irregularity,

and segmental demyelination or remyelination accompanied by neuroinflammation, these changes should once again impact the dMRI signal and its related indices (such as FA and MD) [27].

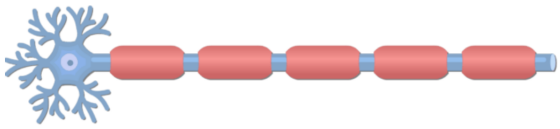

Fig 2.3: *Schematic representation of an axon. From [28].*

Changes in the microstructure could also be due to other mechanisms linked with neuro-inflammation and the consumption of ethanol, such as the formation of oedema and the long term reduction of brain volume due to reduction in white matter (WM) volume.
It has to be noted that the pathways leading to neuro-inflammation are not completely understood yet and that some symptoms observed in AUD patients could be due to co-morbidity factors.

2.2 Effects of alcohol consumption habits

The following sections cover the impact of alcohol consumption on the metrics described in Section 1.2.2. This particular section goes over the impact of alcohol consumption habits, including light and moderate drinking (usually defined as less than 2 alcohol units per day).

The impact of daily alcohol consumption on microstructure parameters, such as fractional anisotropy (FA) and the mean diffusivity (MD), is reported differently based on the study. While the general consensus is that heavy alcohol consumption leads to a reduced FA, increased MD and reduction of white matter integrity, light drinking does not yield such unanimous results.
In a study by Mc Evoy & al. [29], a U-shaped correlation was found between daily alcohol intake and FA. Light and moderate drinkers (<28 alcohol units in the last 14 days) showed an increase in FA, whereas heavy drinkers (>28 units in the last 14 days) showed a decrease in FA values. The authors also noted that the increase in FA was more noticeable in old light/moderate drinking men than in middle-aged men.
Other studies found a negative correlation between FA and daily alcohol intake [30].

2.3 Acute alcohol consumption

The effects of acute alcohol consumption correspond to the effects observed from the onset alcohol consumption to a few hours after ingestion.

A study by Kong & al. [31] has used diffusion kurtosis imaging (DKI) to analyse the impact of acute alcohol intake on the brain microstructure of healthy patients. DKI quantifies non-Gaussian diffusion and has been suggested by the authors to be advantageous over DTI as it better characterizes both normal and pathologic brain tissue, particularly for the assessment of gray matter. One of the primary parameter of DKI, mean kurtosis (MK), measures the degree of diffusion restriction and indicates microstructural complexity. DKI also gives out values for fractional anisotropy (FA) and mean diffusivity (MD).
The authors also used Arterial spin-labeling (ASL), which uses magnetically labeled arterial blood as a tracer to measure regional cerebral blood flow [31].

This study revealed an increase in mean kurtosis and FA at 0.5 hour post-alcohol intake in most brain regions and a decrease in MD in several brain regions at 1 hour after drinking. The decrease in MD was also described in another study by the same authors [32] (on rats), however, a decrease in mean kurtosis was observed in the first half hour in the frontal lobe and thalamus rather than an increase.
The 3D arterial spin-labeling showed an increased cerebral blood flow in most brain regions, particularly in the frontal regions. Men were found to be more sensitive than women to the acute effects of alcohol [31].

In an earlier study by the same authors [33], it was found that acute alcohol intake led to significantly reduced apparent diffusion coefficient (ADC) values of the frontal lobe, thalamus, and middle cerebellar peduncle, reaching a minimum value at 1 or 2 hours after alcohol intake. FA values of the frontal lobe were significantly increased, reaching a maximal value at 0.5 hour.

These findings led the authors of the article to hypothesize that the thalamus, limbic system, cerebellum, and especially the frontal lobes were more subject to alcohol-related brain damage than other cerebral regions. Since the alcohol-induced microstructural changes in these brain regions impact the function of these regions, alcohol intake likely results in both physiologic and psychological consequences on behavior. The limbic system primarily includes the nucleus accumbens, amygdala, and hypothalamus and predominantly controls appropriate responses to stimuli with social, emotional salience, it is also involved in the regulation of sensorial and visceral activity and closely related to psychological activities such as learning, memory, the generation of emotional responses, and behavior. Alcohol-induced parameter changes in the thalamus were associated with changes in mood. These alcohol-induced changes in mood have also been predicted by changes in thalamic connectivity, whereas changes in motor performance have been associated with the cerebellothalamic network. The prefrontal cortex is thought to be one of the most complex anatomic and functional structures of the human brain. Acute ethanol administration in humans has been shown to cause deficits in executive activities and language performance associated with the prefrontal cortex [31].

2.4 Chronic alcohol consumption

This section covers the microstructural consequences of chronic alcohol consumption. The effects observed are thus due to the frequent heavy drinking (more than two alcohol units per day on average) over a prolonged period of time (months, years). In most cases, the observations described apply to AUD patients with uncomplicated alcoholism, in contrast to AUD patients with clinically diagnosed alcoholism-related diseases.
These diseases include : Wernicke's encephalopathy, Korsakoff's syndrome, hepatic encephalopathy, central pontine myelinolysis, alcoholic cerebellar degeneration, alcohol-related dementia, and Marchiafava-Bignami disease. The regions impacted by these diseases (see Fig.2.4) have been linked to zones that were also affected in AUD patients with uncomplicated alcoholism when compared to control patients, although on a smaller scale [34, 35].

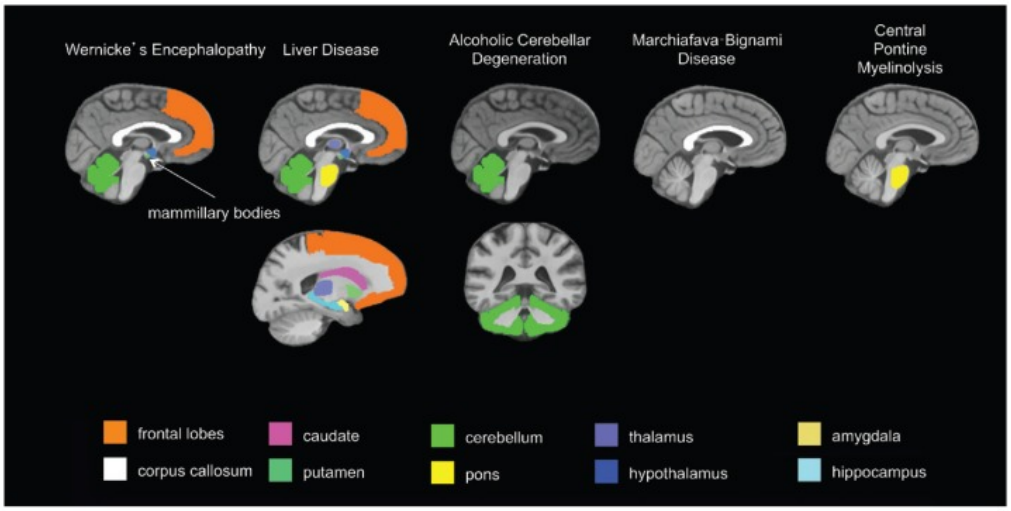

Fig 2.4: *Brain regions targeted by alcoholism-related diseases. From [34].*

2.4.1 Non-treatment-seeking AUD vs control

This section compares non-treatment-seeking (NTS) alcohol use disorder patients to a control population. The term NTS qualifies patients with AUD that still consume alcohol, in contrast to patients with AUD who undergo an abstinence period from alcohol.

The most common observation when comparing AUD patients to a control population is a lower FA in several tracts, such as : the corpus callosum, centrum semiovale, internal and external capsules, fornix, superior cingulate, and longitudinal fasciculi [34].

A study by Wang & al. [36], studied the impact of alcohol consumption on different regions of the corpus callosum (CC), illustrated on Fig.2.5.

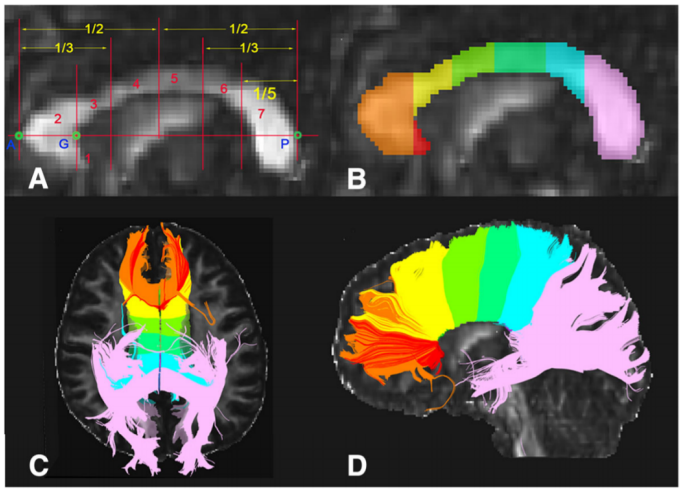

Fig 2.5: *Subregions of the corpus callosum. Segmentation scheme of the corpus callosum (A and B). A and P (in blue) are the anteriormost and posteriormost points, respectively. From [36].*

Overall, a very small decrease in FA was observed in AUD. A slightly more marked increase in MD was measured. MD encompasses the axial diffusivity (AD) and radial diffusivity (RD) (see Section 1.2.2 for more information). The values can be found in Fig.2.6.

Region	FA		AD		RD		MD	
	PT	HC	PT	HC	PT	HC	PT	HC
Subregion 1	0.47 ± 0.05	0.48 ± 0.03	1.41 ± 0.09	1.36 ± 0.09	0.64 ± 0.10	0.60 ± 0.06	**0.91 ± 0.09**	**0.85 ± 0.06***
Subregion 2	0.54 ± 0.04	0.55 ± 0.02	**1.40 ± 0.04**	**1.37 ± 0.04***	0.55 ± 0.06	0.52 ± 0.04	**0.83 ± 0.05**	**0.80 ± 0.04***
Subregion 3	0.49 ± 0.04	0.50 ± 0.03	**1.39 ± 0.04**	**1.35 ± 0.05***	0.60 ± 0.06	0.58 ± 0.05	0.87 ± 0.05	0.83 ± 0.05
Subregion 4	0.50 ± 0.04	0.50 ± 0.03	**1.44 ± 0.04**	**1.41 ± 0.04***	0.62 ± 0.06	0.59 ± 0.05	0.89 ± 0.05	0.87 ± 0.04
Subregion 5	0.49 ± 0.03	0.51 ± 0.03	**1.47 ± 0.04**	**1.43 ± 0.05***	**0.64 ± 0.06**	**0.60 ± 0.06***	**0.92 ± 0.05**	**0.88 ± 0.05***
Subregion 6	**0.46 ± 0.03**	**0.49 ± 0.03***	**1.53 ± 0.08**	**1.47 ± 0.05****	**0.71 ± 0.08**	**0.64 ± 0.06****	**0.98 ± 0.08**	**0.92 ± 0.05****
Subregion 7	0.55 ± 0.02	0.56 ± 0.02	1.57 ± 0.04	1.55 ± 0.05	0.59 ± 0.04	0.57 ± 0.04	0.92 ± 0.03	0.90 ± 0.04
Whole CC	0.53 ± 0.02	0.54 ± 0.02	**1.50 ± 0.03**	**1.47 ± 0.04***	**0.60 ± 0.04**	**0.57 ± 0.03***	**0.90 ± 0.04**	**0.87 ± 0.03***

Fig 2.6: *** $P < 0.01$, * $0.01 < P < 0.05$. For illustration, all values of AD, RD and MD were multiplied by 1000. Abbreviations: HC healthy controls, PT alcohol-dependent patients. Entries in boldface are diffusion metrics with significant inter-group differences ($P < 0.05$). From [36].*

The authors mention that, since FA changes can be driven by both parallel and perpendicular diffusivity, FA is thus a comprehensive reflection of the water diffusion profile. Other diffusion metrics may provide more directionally specific and complementary information. Specifically, AD represents the water diffusivity parallel to the axonal fibers. Altered AD may reflect axonal swelling, degeneration and deletion. RD represents the water diffusivity perpendicular to the axonal fibers. Altered RD may reflect myelin disruption. In this study, the authors found that the whole CC and its subregions of the alcohol-dependent patients exhibited alterations mainly in AD, RD and MD, which was consistent with other studies showing that these three

diffusion metrics can more sensitive than FA [36].
Using a similar methodolgy (analysing the fiber tracts going through the corpus callosum), Liu & al. [37] also found similar results with an overall decrease of generalized fractional anisotropy (gFA) in all segments of the corpus callosum, with the segment interconnecting the bilateral orbitofrontal cortices being the most affected. Generalized FA (gFA), measures the anisotropy of an orientation dispersion function (ODF) of white matter bundles. It is thus similar to FA, but it is supposedly less sensitive to errors that arise in the presence of complex fiber architectures, such as crossing fibers [38].

A study by Chumin & al. [39], found that when compared to a control population, young AUD patients had higher fractional anisotropy (FA) values throughout the major white matter (WM) tracts, but also had lower FA values in WM tracts in the cerebellum and right insula. Mean diffusivity was generally lower in the AUD group, predominantly in the areas where FA differences were absent.

Alterations of FA, MD, AD, and RD values may reflect differences in axonal diameters, density, and myelination. The literature has reported that decreases in WM integrity are associated with alcohol use (for review, see [34]) and higher WM integrity is associated with better cognitive functioning [40]. However, the authors' results show that young AUD subjects have elevated FA, with lower MD, RD, and AD throughout major WM tracts of the Tract-based Spatial Statistics (TBSS) FA skeleton (see Appendix B.3 for more information about TBSS) compared to yound controls. This suggests that young AUD may have different axonal diameters, density, and/or myelination compared to control subjects. The authors propose several potential explanations for these unexpected results. It is possible that accelerated myelination of callosal tracts may present a vulnerability for adolescent AUD [41]. Alternatively, such WM changes might reflect compensatory responses that occur during the early progression of AUD [42]. Indeed, fMRI (see Appendix B.1 for more information about fMRI) studies have shown that subtle reorganization of functional activation may occur during the progression of AUD with increasing use [43]. Taken together, these findings could suggest that the early stages of AUD may be associated with higher FA in many regions, either as a function of predisposition to AUD [44] or as a result of the effects of extensive alcohol exposure during the early stages of AUD. Further work is needed to understand whether or not these neurophysiological signatures are related to behavioral and cognitive endophenotypes in the early-stage AUD, and whether they are predictive of sustained AUDs throughout adulthood [39].

Another study by Chumin & al. [45], investigated the comorbidity between alcohol dependence and cigarette smoking. Smoking non-treatment seeking (NTS) AUD patients were found to present a lower FA compared to smoking social drinkers (SD), predominantly in the left hemisphere. The FA and the number of drinks per week were negatively related across the full sample.

A study by Wang & al. [46], found decreased fractional anisotropy and reduced

gray matter volume in the mesocorticolimbic system including the dorsal posterior cingulate cortex, the dorsal anterior cingulate cortex, the medial prefrontal cortex, the orbitofrontal cortex and the putamen in alcohol dependent patients compared to healthy controls.

A study by Pfefferbaum & al. [47], also investigated which regions were impacted by alcohol dependence. In Fig.2.7 are represented the most impacted regions, which display reduced FA values compared to the control population.

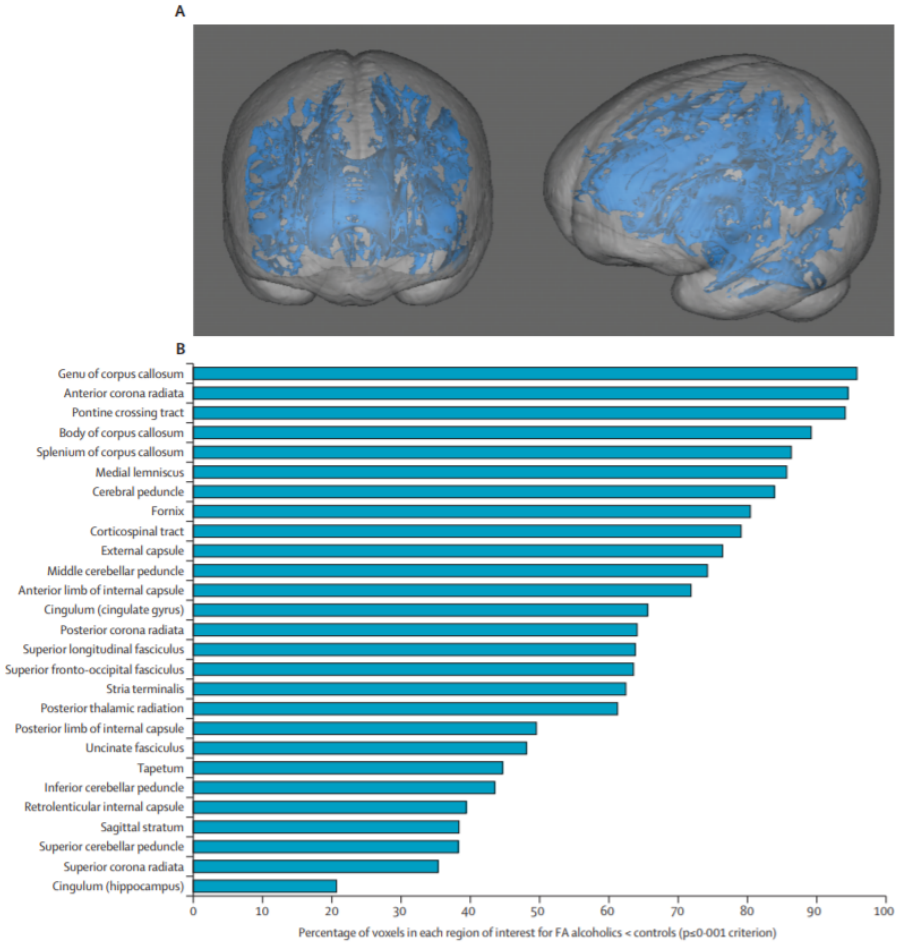

Fig 2.7: *Differences in ageing between alcohol-dependent participants and controls (A) 3D-rendering of the FA skeleton (blue) showing significant differences in alcoholic participants relative to controls. (B) Percentage of significant voxels showing an effect of alcohol dependence.*

A previous study by Pfefferbaum & al. [48], had already found that alcoholism affected FA and diffusivity, particularly the transverse diffusivity, of several fiber bundles. The frontal and superior sites (frontal forceps, internal and external capsules, fornix, and superior cingulate and longitudinal fasciculi) showed greater abnormalities in alcoholics relative to control subjects, whereas more posterior and inferior bundles were relatively spared [48].

An analysis of the neurite density and the orientation dispersion index (ODI) using NODDI by Morris & al. [49], showed that binge drinking young adults displayed a lower ODI, which was used a putative measure for neurite complexity, in the frontal cortical grey matter. The binge drinkers also displayed an increased neurite density in the cortical white matter near the regions with lower ODI. The ventral striatal grey matter ODI was also higher in the binge drinkers when compared to the controls.

2.4.2 Abstinent AUD vs control

As described by De Santis & al. [30], compared to control patients, AUD patients after 1 week of abstinence from alcohol consumption display a reduced FA and AD and an increase in MD and RD (see Fig.2.8). These changes were located mostly on white matter tracts in the frontal and superior regions. Furthermore, the differences in FA were more pronounced in the right hemisphere, while the differences in axial diffusivity were more pronounced in the left hemisphere.
The fiber tracts that were the most impacted were the corpus callosum and the fornix. The corpus callosum displayed a reduced FA, while MD and AD increased. In the fornix tracts, the only statistically significant decrease was the FA [30].
Although this decrease in FA without a significant change in AD or RD may seem counter-intuitive, it could be explained either through a small decrease of AD and a small increase of RD adding up to a larger increase of FA, or through part of the population experiencing higher RD and the other part showing a lower AD. Individually, the metrics would then not be statistically significant but their on impact on FA might be.

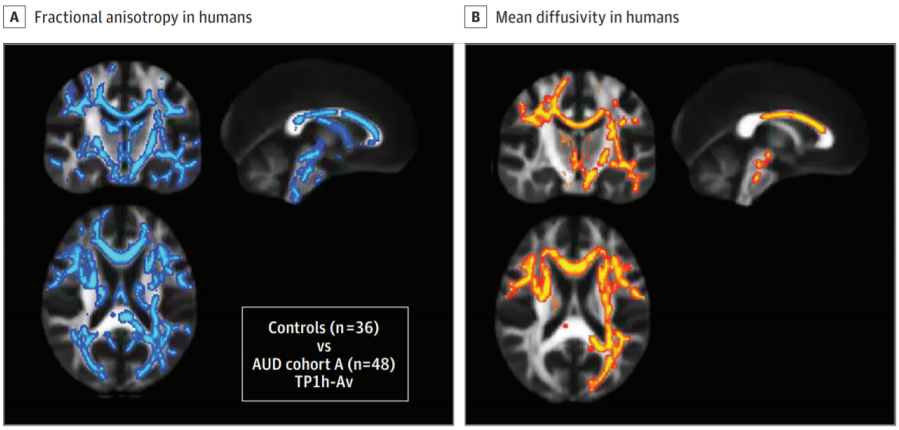

Fig 2.8: *Differences between Alcohol Use Disorder (AUD) patients and controls in the White Matter Skeleton. From [30].*

This decrease in FA was also observed in the frontal and superior tracts (underlying cingulate, frontal gyrus, and precentral areas) by Fortier & al. [50].

The differences between male and female abstinent AUD patients were studied by Sawyer & al. [51], it was noticed that in some regions (such as portions of the corpus

callosum, the superior longitudinal fasciculi II and III, and the arcuate fasciculus and extreme capsule) alcoholic men had diminished FA. Whereas, alcoholic women had higher FA in these regions. There were, however, no significant results from the axial or radial diffusivity analysis.

2.4.3 Before and after abstinence

AUD patients were observed by De Santis & al. [30] during the first few weeks of abstinence from alcohol. The FA decreased and the MD increased, increasing the difference in FA and MD values when compared to control non-AUD patients. The variation of AD was less clear with an increase or decrease in different brain regions varying with time. However, most white matter regions had experienced an increase in AD by the 6th week of abstinence.
This decrease in FA was attributed to a progressive myelin and axonal damage process, but also to glial or cellular reactions, such as the ones occurring during an ongoing inflammatory process [30].

A study by Zou & al. [52], looked at the microstructure differences between future abstinents and future relapsers (the groups were formed a posteriori) after an initial abstinence period. The future relapsers displayed a decrease in FA in the corpus callosum (genu and splenium) and an increase in FA in the stria terminalis/fornix. The relapsers also showed an increase in MD in the corpus callosum genu, stria terminalis and a decrease in MD in the anterior corona radiata.

Part II

Microstructure imaging in alcohol use disorder: a case study

Chapter 3

Methods

3.1 Data

The data was acquired in St-Luc, on a 3T SIGNA Premier GE MRI scanner.
Two AUD patients were scanned a first time before the abstinence period and then after two weeks of abstinence from alcohol consumption. However, during the first scanning session, one of the patient' scan was compromised and the resulting volumes were unusable. This left us with one set of data available for a before/after abstinence comparison and a single scan of a AUD patient after a two week abstinence period.

For each scan, an anatomical scan (T1-weighted, with a 156x256x256 resolution) was performed before the diffusion sequences. The diffusion volumes are composed of 160 volumes with direction gradients and 7 with b0 values. The size of the diffusion volumes varied between 256x256x66 to 256x256x68 between scans. The Eddy currents were corrected by the MRI scanner during the acquisition process.

The data to be analyzed during this thesis were thus the following files:

`20191125_HA_ANAT_T0.nii`	`20191213_HA_ANAT_T1.nii`	`20191213_FA_ANAT_T1.nii`
`20191125_HA_MS_T0.nii`	`20191213_HA_MS_T1.nii`	`20191213_FA_MS_T1.nii`
`20191125_HA_MS_T0.bval`	`20191213_HA_MS_T1.bval`	`20191213_FA_MS_T1.bval`
`20191125_HA_MS_T0.bvec`	`20191213_HA_MS_T1.bvec`	`20191213_FA_MS_T1.bvec`

With the `ANAT` files containing the T1-weighted anatomical scans, see Fig.3.1. The files ending in `_T0` and `_T1` represent scans before and after alcohol withdrawal, respectively. More information about the NIfTI file type (`.nii`) can be found in Appendix B.2.

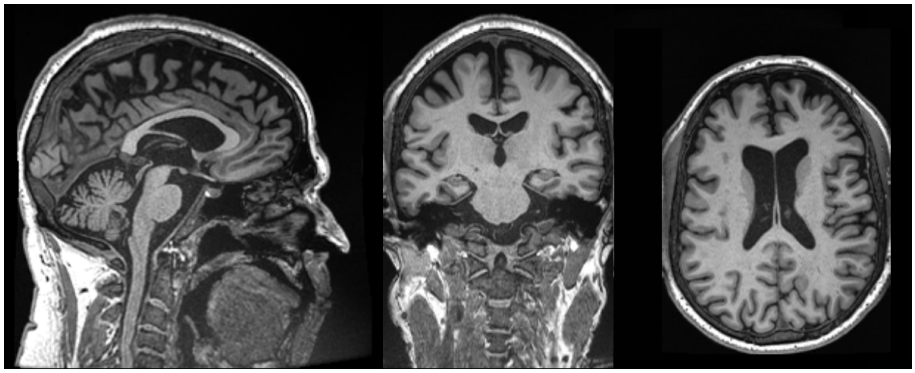

Fig 3.1: *Anatomical slices in the sagittal (Left), coronal (Middle) and axial (Right) view.*

3.1.1 Multi-shell diffusion MRI

The data was acquired with a sequence containing 4 different b-values (see Section 1.2.1 for more details about the b-value), the b-values used were 0, 1000, 2000, 3000 and 5000 [s/mm^2]. The Delta Δ and delta δ values were 35.66 and 23.824 [ms] respectively. G was 30.8, 43.55, 53.34 and 68.86 [mT/m], see Section 1.2.1 for more information about these values. Sequences using several b-values are called "multi-shell". These shells can be represented on a 3D sphere (see Fig.3.2) with each b-value being linked to the radius of the sphere and the position of the points on the sphere being characterized by the b-vectors. The complete b-value (`bval`) and b-vector (`bvec`) files are available in Appendix. C.1,C.2.

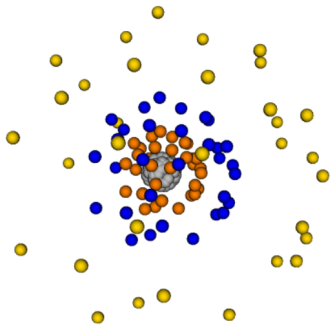

Fig 3.2: *Visual representation of the four shells used : 1000 (grey), 2000 (orange), 3000 (blue) and 5000 (yellow) [s/mm^2].*

There were 64 direction gradients for the 1000 shell and 32 for the other shells. The in-plane resolution was 0.8594 [mm]. The slice thickness was 2 [mm]. TR was 4842 [ms] and TE 77.4 [ms].

3.2 Data preprocessing

The acquired diffusion data has to go through a data processing timeline in order to extract the variables of interest. This section covers the different aspects of this pipeline, from raw data to corrected volumes and extracted diffusion values.

3.2.1 Movement correction

Movement correction is necessary to reduce the impact of the patient's movement during the scan. Using a movement correction algorithm, a new DWI set without this interference can be created. The two main programs providing motion correction used during this thesis were *ExporeDTI* and *FSL*.

With ExploreDTI

The movement correction can be achieved using `ExploreDTI`, a graphical toolbox developed by Alexander Leemans, for exploratory diffusion (tensor) MRI and fiber tractography [53].

RGB slices of the patient before (left) and after (right) movement correction are displayed in Fig.3.3. The volume post correction is visually more coherent and presents less noise. This can be seen in regions such as the corpus callosum, where the corrected slice displays a brighter and more homogeneous red. When analyzing the main output values (such as FA an MD) the corrected volume displays a smaller standard deviation across all values compared to the uncorrected version.

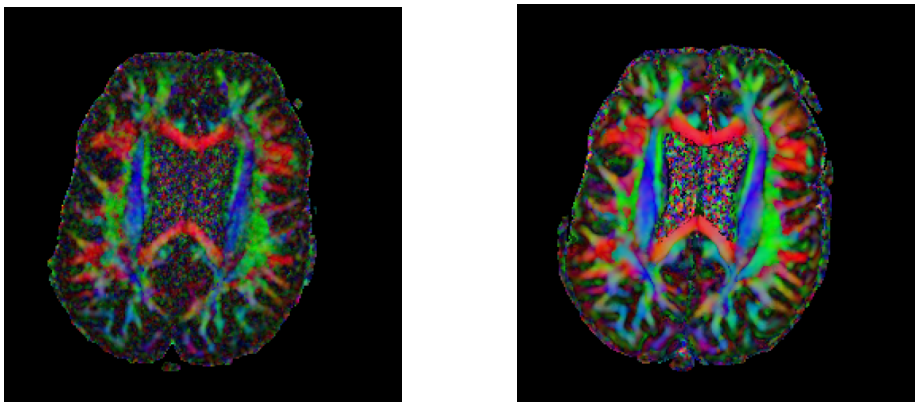

Fig 3.3: *RGB image of the diffusion before (Left) and after (Right) movement correction using `ExploreDTI`.*

When using programs such as `ExploreDTI`, one has to be careful of the different conventions when it comes to orientations and directions. In `ExploreDTI`, the orientations and directions have to be manually encoded and it falls on the user to

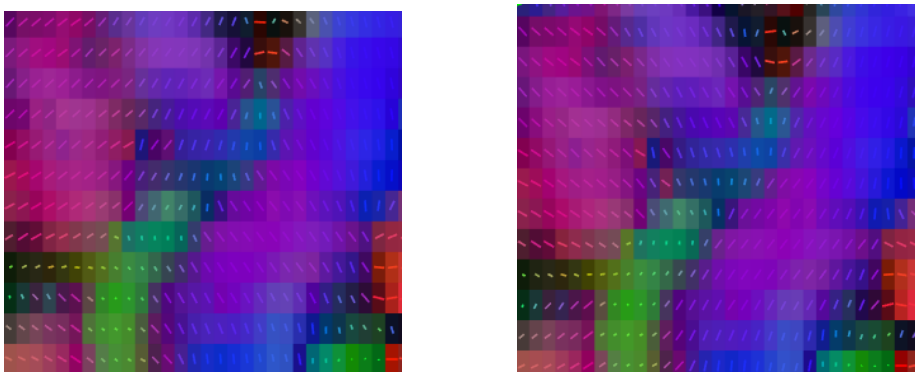

Fig 3.4: *Orientation of the tensors in a slice with a : wrong orientation (Left) and correct orientation (Right).*

check that the data is correctly oriented. This can be seen by plotting the glyphs on a slice with high directionality, see Fig.3.4.
As displayed in Fig.3.4, using the inadequate input parameters for the orientation of the scan can lead to visual inconsistencies throughout the fiber paths. In the left figure, the *purple* (purple is mix between the *blue* representing a top/bottom direction with respect to the head of the patient and the *red* associated to directions from left side of the head to the right side or from right to left) tensors seems to cut across the general direction of the fiber while in Fig.3.4 (Right), they seem to be parallel to the fiber direction.

`ExploreDTI` also allows for the visualization of the movement of the patient during the scan and the corrective transformation applied, see Fig.3.5. The AUD patient never moved more than 2 [mm] in any direction.

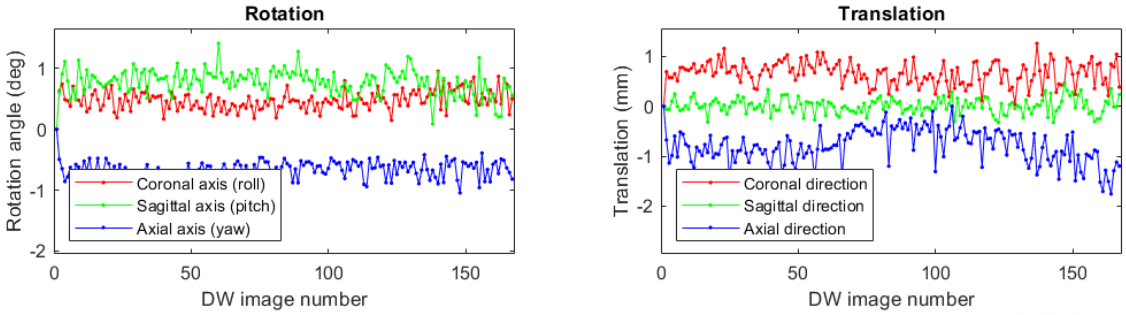

Fig 3.5: *Motion correction applied with ExploreDTI*

The complete movement graphs for all scans can be found in Appendix D.1.

A problem arose when exporting the new b-values and b-vectors from *ExploreDTI*. Indeed, the movement correction also has an impact on the b-vectors, a new file should thus be created to adapt to the modified diffusion volume.
The b-values and b-vectors returned by *ExploreDTI* varied too greatly, some b-values went from 1000 to around 200. While approximated results could be found using the

original b-values and b-vectors files, this software was therefore abandoned in favor of an alternative toolbox for motion correction.

With FSL

FSL, short for FMRIB Software Library, is a library of analysis tools for FMRI, MRI and DTI brain imaging data created by Analysis Group.
This program can be used for movement correction using the `eddy_correct` function, the main objective of this algorithm is to correct the distortions due to eddy currents but it also does some movement correction. The output of this function are the corrected diffusion volumes (a `.nii.gz` file) and the list of transformations applied to correct for movement (a `.ecclog` file).
The b-vectors have been rotated to fit the transformations applied to the diffusion volumes (recorded in `ecclog`) using the `fdt_rotate_bvecs` function.

A way to rapidly check if the new b-vectors are correct is to compute the correlation between the b-vectors before and after correction. The b-vectors should be slightly modified by the movement correction but should not present any major changes that would greatly decrease the correlation between the two.
The correlation between the two b-vector files being 0.99, the new b-vectors appear to be correct. For comparison the b-vectors returned by *ExploreDTI* had a correlation coefficient varying between 0.16 and 0.0029.

FSL also has a function (`fslorient`) to force the orientation of the diffusion volume to either neurological or radiological. This is useful to correctly make use of other programs further down the pipeline as they might require a neurological or radiological input, or they might detect it automatically. An example is *DSI Studio* which requires a volume in the neurological orientation.

While the corrections of the diffusion volume using *ExploreDTI* were smoother, due to a more adapted movement correction algorithm, the unexpected values returned for the b-values and b-vectors files made the visually inferior movement correction provided by FSL a better choice, since it was more methodologically correct.

3.2.2 Registration

To see which regions of the brain are the most impacted by alcohol consumption, it can be useful to compare the entirety of the volume directly without pre-selecting a region of interest.
The volumes, obtained before and after the abstinence period, then need to be registered into the same space, even if the two scans are from the same patient. The following section will cover the transformations used to register two volumes of the same patient at different times. The method followed comes from `DIPY` tutorials.

The first step is to load the two scans and to extract a b0 (with a b-value of 0) volume in each scan. The b0 volumes, with a brain mask applied, will be used to register the two volumes. A first translation based on the center of mass will roughly center both volumes, see Fig.3.6.

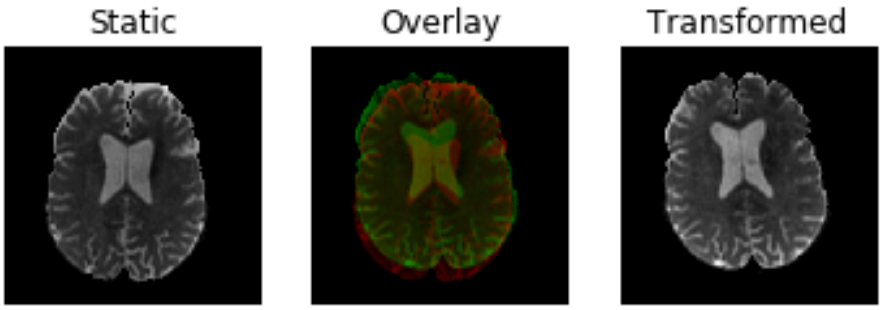

Fig 3.6: *Slices of the volumes to be registered after the center of mass translation, T0 (left) and T1 (right).*

A metric, such as Mutual Information (MI), can then be used to further improve the initial translation (see Fig.3.7). Since we are working with volumes, the optimization process has to be computed in the three dimensions.

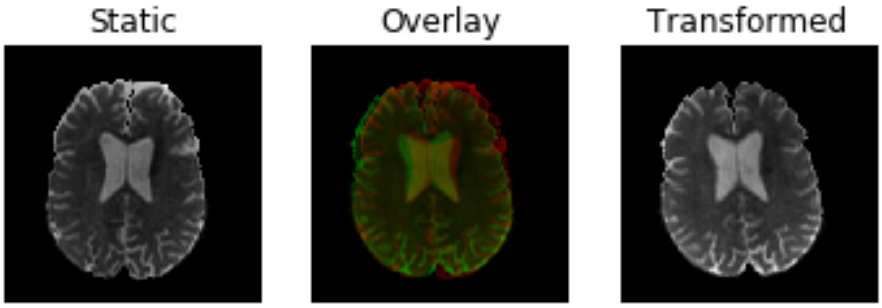

Fig 3.7: *Slices of the volumes to be registered after the rigid transform, T0 (left) and T1 (right).*

The next step is a rotation to fine tune the orientation of the volumes (see Fig.3.8). The same metric, MI, can be used.

The resulting registration is fairly accurate for scans of the same patient but additional steps could be applied to register scans of different patients. These steps would include affine transformations such as translation, rotation, scale and shear. Once the registration process is applied, the registration parameters can be saved to prevent from going over the whole optimization process the next time a registration, with the same volumes, is needed.

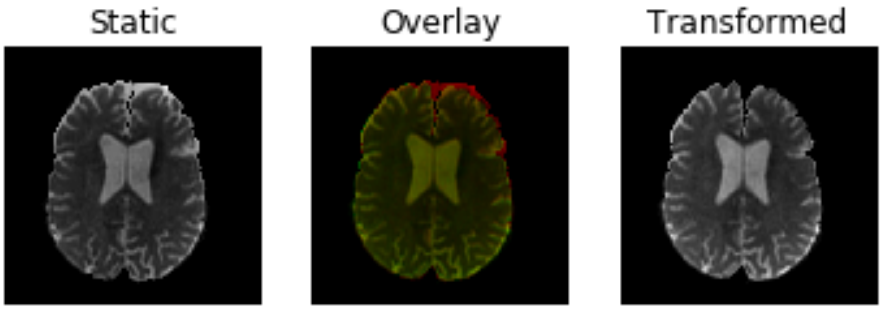

Fig 3.8: *Slices of the volumes to be registered after the rotation step, T0 (left) and T1 (right).*

3.2.3 Creation of volumes of interest

To analyze the diffusion of a specific brain region, also known as region of interest (ROI) or volume of interest (VOI), different ways of segmenting the brain are possible. The first is to use the automated atlases readily available in a visualisation program such as the *HCP1021* template in *DSI Studio*. The second is to download MNI spaces and the pre-drawn regions associated to it (available online in *NatBrainLab* [54], for example) then to register it to the scan of the patient of interest. Lastly, the other option is to directly draw the VOI in the anatomical scan of the patient using programs such as *MRIcron*.

Software-based automated atlas

The automated atlases available in *DSI Studio* are based on averaged "standard" brains in which regions have already been segmented. The template used by *DSI Studio* is *HCP1021* but many other exist such as HCP842 or SPM 96 and SPM 99 which use standard brains from the Montreal Neurological Institute (MNI).
The templates are registered to the brain under study with two steps: first an affine transform then a non-linear transform.

The regions segmented using this method were a decent fit to the anatomical scan. However, upon visual inspection, small regions like the fornix were often out of bounds due to their small size and larger regions, such as the corpus callosum, often included part of the neighbouring structure (CSF, etc.). This inclusion of the neighbouring structures and occlusion of certain part of the region led to an increase of the standard deviation of the variables analyzed in DTI and other models (see Table.3.1 for the comparison in FA values between the different methods).

MNI spaces available online

Another method of segmenting brain regions is to use pre-segmented regions on MNI spaces available online. The site *NatBrainLab* [54] was suggested to me by Laurence Dricot. The package of each brain region can be downloaded as well as an "averaged"

brain template used as MNI space.
DSI Studio allows the use of MNI spaces, so the MNI space was loaded and fitted to the patient data (using affine and non-linear transformation, as mentioned previously) and the MNI VOI was then loaded on top.

It does however suffer from the same limitations as the automated atlases mentioned in the previous section (see Table.3.1 for the comparison in FA values between the different methods).

Hand-drawn VOI

In this section, the regions were hand-drawn using *MRIcron*. The regions were drawn in the the anatomic T1-weighted images slice by slice then registered to the diffusion volume data. This registration step is necessary because the anatomical and diffusion volumes are not the same size : the anatomical images have a higher solution (256x256x156) in the z direction than the diffusion datasets (256x256x66). Although this is time consuming, the resulting VOIs were closer to the anatomical truth than both other methods, especially for small volumes like the fornix. The three regions obtained using the different methods are displayed in Fig.3.9, and although they are similar, there are some shape variations due to the arbitrary process of hand-drawn segmentation by different people.

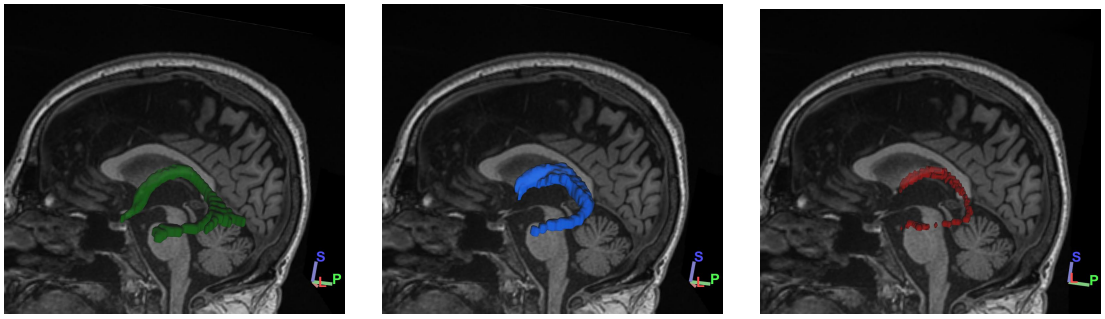

Fig 3.9: *VOI of the fornix using : automated atlas in DSI Studio (left, in green), NatBrainLab atlases (middle, in blue) and hand-drawn (right, in red).*

The mean and standard deviation of FA of the three regions displayed in Fig.3.9 are available in Table 3.1, as well as the number of voxels in each VOI. Although the standard deviations are similar, the hand-drawn region has the highest FA and the lowest voxel count. It was hypothesized that the lower FA in the other two regions was due to the inclusion of CSF in the fornix VOI and that the standard deviation stayed similar due to a higher number of voxels.

Going forward, the regions will be segmented with hand-drawn VOI whenever possible as they seem to fit better the anatomical truth.

	Automated	NatBrainLab	Hand-drawn
FA mean	0.48	0.50	0.52
FA standard deviation	0.21	0.21	0.21
Voxel count	2677	3946	981

Table 3.1: *Display of the fractional anisotropy (FA) values of the fornix with different VOI segmentation methods*

3.2.4 Tractography

As mentioned previously, tractography is a useful tool to visualize the estimated fiber tracts in the brain, but it can also be used for segmentation and defining VOIs.

A tractography algorithm needs three input : diffusion data, seed points and white matter region mask. The data is acquired from a diffusion sequence. The seed points are user-defined voxels from which the tracking process will start. They are usually placed in the region of interest (ROI) or can be randomly placed in a volume of interest. The white matter region mask is used to determine the regions in which the tracts will propagate from the seed points.
A method to obtain the orientations from the diffusion data and the tracking stopping criterion also needs to be specified when implementing the code.

There are two approaches to fiber tracking: deterministic or probabilistic tractography algorithms.
Deterministic tractography assigns a single orientation estimate to each voxel resulting in tracking errors due to noise or crossing fibers, as there is only a single pathway available for each seed point.
Probabilistic tracking algorithms, on the other hand, use a collection or distribution of possible orientations for each voxel, leading to multiple trajectories for each seed point. The strengths of probabilistic tracking are thus linked to zones in which deterministic tracking has issues to connect tracts, such as zones with high orientation uncertainty and regions with high fiber tract density.
For these reasons, probabilistic tractography will be used in this report, instead of deterministic tracking [55].

It is important to note that both approaches are impacted by the same limitations. Although tractography is a useful tool to visualize the connectivity between brain regions, these fiber tracts are virtual and have little quantitative or biological meaning. Short and straight tracts are also more prevalent in a tractography due to tracking algorithms encountering regions of complex fiber configuration (such as crossing and fanning) [55].

Deterministic approach (with DSI Studio)

As mentioned previously, the deterministic approach assigns a single orientation estimate to each voxel. This is the approach implemented in *DSI Studio*. As can be

seen on Fig.3.10 (Left), the fiber tracking is limited in the number of tracts found in the corpus callosum region and the tracts do not match what was expected (see Fig.2.5 for reference). This is due to the "single orientation" rule in the approach which limits the number of tracts passing through a region. If the region is composed of several crossing fibers regions, voxels with several of these fiber orientations will not be linked due to the tracts selecting the direction with the greatest diffusion.

In Fig.3.10, is an illustration of the tractography results found with a deterministic (Left) and probabilistic (Right) method. The seed points used were on a plane passing through the mid-section of the corpus callosum (in between the left and right hemispheres).

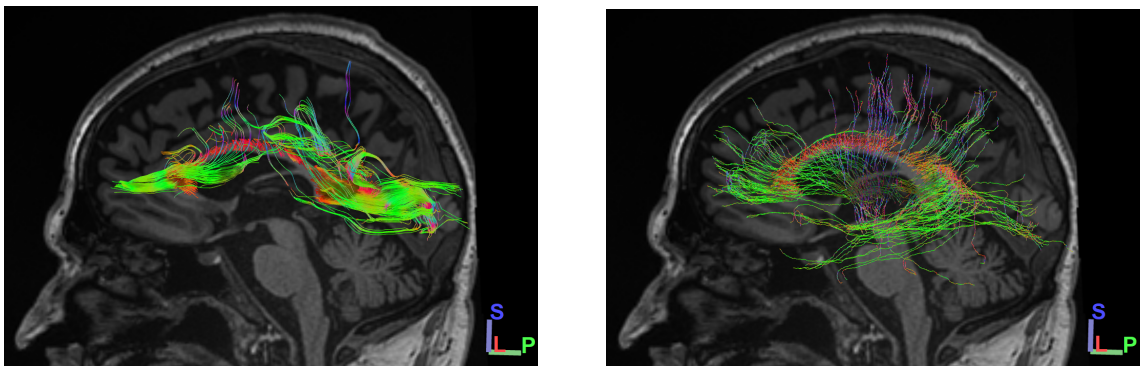

Fig 3.10: *Fiber tracking of the corpus callosum using a: deterministic (left) and probabilistic (right) approach.*

Probabilistic approach (with the CSD model in Python)

The probabilistic approach is put in place by the `DIPY` library in Python. Using the "*Probabilistic Direction Getter*" method in *DIPY*, the data can be loaded and fitted with a Constrained Spherical Deconvolution (CSD) model.

The CSD model by Tournier & al. [56] is based on the hypothesis that if it is possible to estimate the response function of a single fiber then it should be possible to deconvolve the measured signal and to obtain the underlying fiber distribution. This would allow the creation of a fiber orientation distribution function (fODF) for each voxel.
The ODF thus represents the distribution of water diffusion as a function of the direction. The peaks of the ODFs can be used as estimates for the main orientations of a tract segment at each voxel. The ODF is then used by the used by the `Probabilistic Direction Getter` method (available in `DIPY`) as a probability mass function (PMF) for sampling tracking directions.

The tracking obtained with this probabilistic tractography is shown in Fig.3.10 (Right).
It is also possible to select only certain sections of the tract (saved in a `.trk` file)

obtained in Python, such as the front fibers of the corpus callosum (as displayed in Fig.3.11-Left). The remaining tracts can then be converted into a VOI (shown in Fig.3.11-Right) with *DSI Studio* and analyzed in the same manner as the regions created via other means (see Section 3.2.3 for more information about VOI/ROI creation).

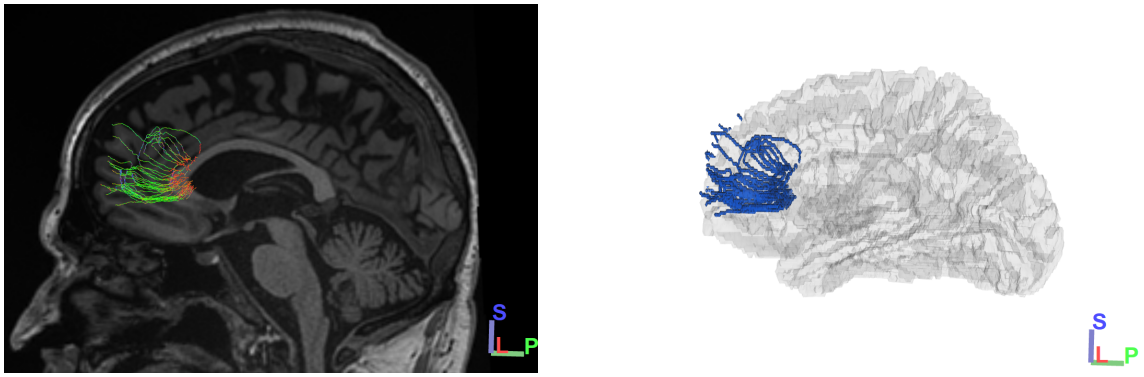

Fig 3.11: *Fiber tracking of the front of the corpus callosum (Left) and the resulting VOI (Right).*

This method of creating VOI was not used during this thesis but could be used to segment fiber tracts, such as the corticospinal tract, in patients where the automated atlases would be obsolete, such as children with highly damaged brain structures.

3.2.5 Region-based analysis

Using the methods mentioned previously, the brain can be segmented and the diffusion parameters can be extracted from these regions. This allows to see which regions are most impacted by alcohol consumption habits, by using these regions as masks during our DWI analysis.

Based on our biological knowledge of AUD (see Section 2) and the availability of the regions in *DSI Studio*, the following regions were selected for region-based analyses:

- Amygdala (Left & Right)
- Brain Stem
- Cerebral White Matter (Left & Right)
- Corpus Callosum
- CorticoSpinal Tract (Left & Right)
- Fornix (Left & Right)
- Hippocampus (Left & Right)
- Inferior Cerebellar Peduncle
- Insula (Left & Right)
- Middle Cerebellar Peduncle
- Occipitopontine Tract (Left & Right)
- Putamen (Left & Right)
- Superior Cerebelar Peduncle

Due to time constraints all regions but the corpus callosum (which was hand drawn) were obtained from the automated *HCP1065* atlas in *DSI Studio*. The results obtained from these atlases will have to be handled with caution as they do not perfectly overlap the anatomical regions, a disadvantage all automated registered

atlases share. This trade-off between speed and accuracy will have the biggest negative impact on small regions surrounded by a very different microstructure, since the small translation errors can lead to regions that are completely outside the anatomical truth. An example of such a region is the fornix, for which caution will have to be exercised when interpreting the results.

The diffusion parameters, or diffusion metrics, can be obtained using the `DIPY` library [57] and implementing the code in Python. In the following sections (Section 3.3.1 to 3.3.4), the models used to extract those parameters and the possible output parameters are listed. Most of the codes used were adapted from the tutorials available on the `DIPY` website [57].

Since the different models, programs and codes sometimes use different orientations and left/right conventions, extra care has been taken to make sure that the region of interest matches the volumes output from the different model. Visual checks such as the one presented in Fig.3.12 were incorporated throughout the pipeline to prevent left/right inversions from going unnoticed. In Fig.3.12, the corpus callosum is highlighted in orange on volumes coming from different models, such as : the models available in DIPY, NODDI, DIAMOND and microstructure fingerprinting (respectively, from left to right).

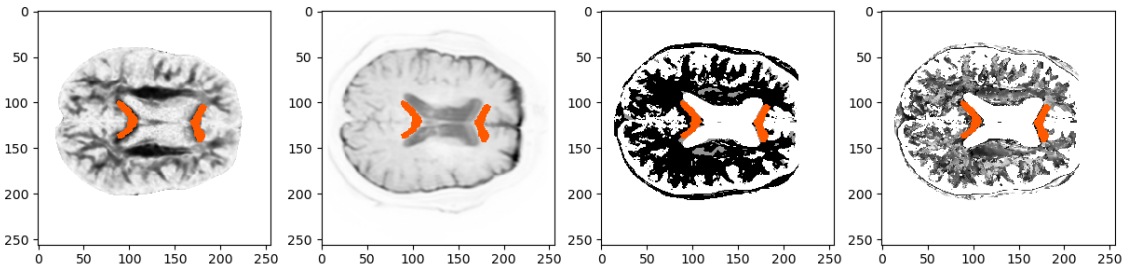

Fig 3.12: *Corpus callosum mask (in orange) visual position check on a volume from: DIPY (Far-Left), NODDI (Left), DIAMOND (Right) and fingerprint (Far-Right).*

3.3 Microstructure estimation

This section covers the different models used for the microstructure estimation. The DTI, DKI, MSDKI and WMTI models were implemented in Python following the *DIPY* tutorials [57]. The NODDI model was applied to the data through the Quantitative Imaging Toolkit (QIT) software. DIAMOND was installed using Benoit Scherrer's GitHub repository. The microstructure fingerprinting model was performed using the Python code provided by Rensonnet G.

3.3.1 DTI (using DIPY)

Diffusion tensor imaging (DTI) and the diffusion tensor model are one of the classic ways of characterizing the diffusion within voxels. See Section 1.2.2 for more information about DTI.
Here are the outputs:

`FA`	fractional anisotropy
`MD`	mean diffusivity
`AD`	axial diffusivity
`RD`	radial diffusivity
`RGB`	RGB map representation of the tensors

FA (Fig.3.13 (left)) is widely considered to be an indirect measure of axonal integrity, even if some find it more accurate to consider FA as an indication of the density of packing of fibers in a voxel, and the amount of myelin wrapping these axons [57]. The value of FA ranges from 0 (completely isotropic diffusion) to 1 (completely anisotropic diffusion). The MD (Fig.3.13 (middle)) represents the diffusion of the water molecules in the brain' structures and is a weighted average of the axial (AD) and radial diffusivity (RD). MD is considered to be an indicator of white matter damage and ranges roughly from 0 to 3.10^{-3} [mm^2/s], which corresponds to the diffusivity in the CSF.

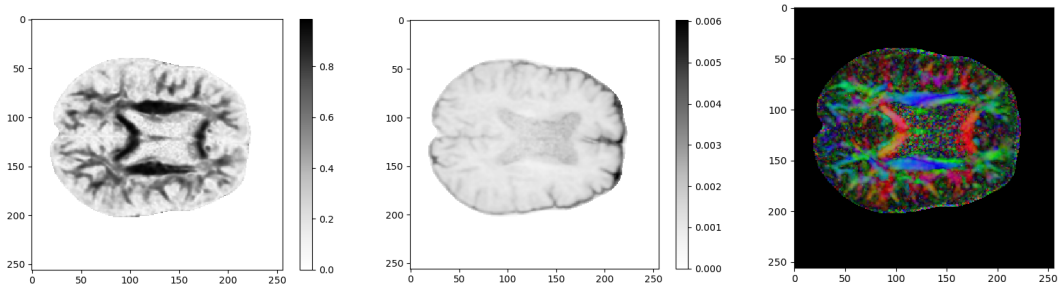

Fig 3.13: *Fractional Anisotropy (Left), Mean Diffusivity (Middle) and RGB diffusion tensor map (Right).*

3.3.2 DKI (using DIPY)

In order to quantify the degree of non-gaussianity of the diffusion in tissues, DKI was also estimated. The measurements made with the kurtosis tensor model can characterize the microstructural heterogeneity of tissues and provide putative measures of density of axonal fibers density and the diffusion tortuosity.
The metrics that were obtained with DTI, such as FA and MD, can also be obtained via the diffusion tensor model, as well as the following metrics:

`FA`	fractional anisotropy
`MD`	mean diffusivity
`AD`	axial diffusivity
`RD`	radial diffusivity
`MK`	mean kurtosis
`RK`	radial kurtosis
`AK`	axial kurtosis
`MKT`	mean of the kurtosis tensor
`KFA`	kurtosis fractional anisotropy

Observing the differences between axial and radial diffusivity (see Section 1.2.2 for more information about AD and RD) can prove to be more informative than looking only at the MD. In Fig.3.14, the MD (in the middle) seems to be somewhat uniform throughout the white matter, whereas AD (left) and RD (right) both provide additional patterns with varying diffusivity. In the corpus callosum (CC) for example, the AD is high while the RD is low, this means that the diffusivity in the CC is much higher along the direction of the axons compared to perpendicularly to it.

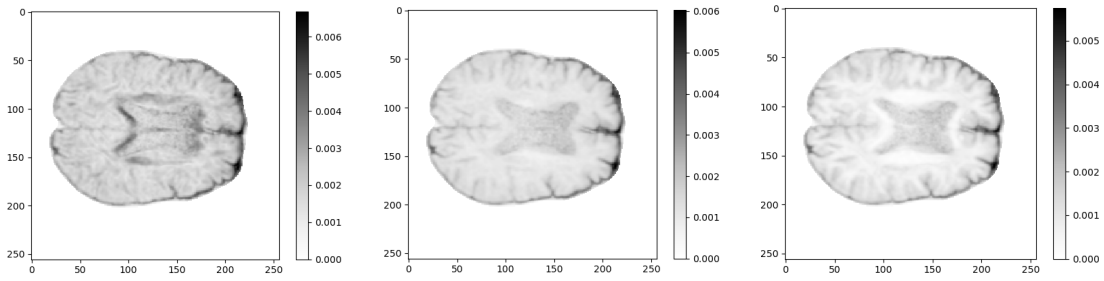

Fig 3.14: *Axial Diffusivity (Left), Mean Diffusivity (Middle) and Radial Diffusivity (Right).*

The MK measures the degree of restricted diffusion and is considered to be an indicator of microstructural complexity. MK (see Fig.3.15 (middle)) is composed of RK (right) and AK (left) which represent the radial and axial components respectively. The values of kurtosis in this report are contained between 0 and 3.
As can be seen in Fig.3.15, some artefacts appear in regions with well-aligned fibers. This is due to the DKI model finding negative values in regions of "deep white matter": the low radial diffusivity of well-aligned white matter regions makes it hard to capture non-Gaussian information in the radial direction due to its low diffusion decays [57].

In addition to the values displayed above that take into account the diffusivity and the kurtosis, values that only take the kurtosis into account can also be extracted: those values are the mean kurtosis tensor (MKT) and the kurtosis fractional anisotropy (KFA). Both of these values are displayed in Fig.3.16. The MKT produces results that are visually similar to the MK.

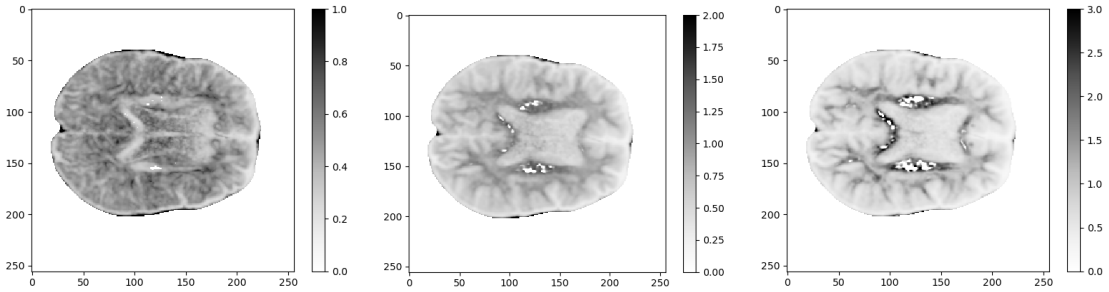

Fig 3.15: *Axial Kurtosis (Left), Mean Kurtosis (Middle) and Radial Kurtosis (Right).*

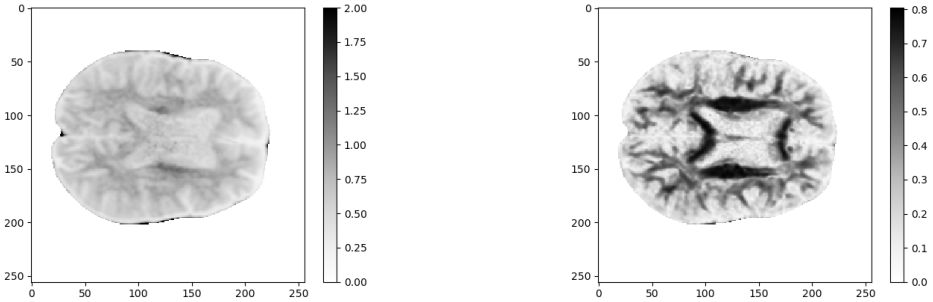

Fig 3.16: *Mean kurtosis tensor (Left) and kurtosis fractional anisotropy (Right).*

3.3.3 MSDKI (using DIPY)

Mean signal diffusion kurtosis imaging (MSDKI) is used to obtain a characterization of non-Gaussian diffusion independently of the degree of fiber organization. Indeed, "classic" DKI measures (see section above) are impacted by properties such as fiber dispersion or the intersection angle of crossing fibers.
The output variables are:

`MSD` mean signal diffusivity
`MSK` mean signal kurtosis

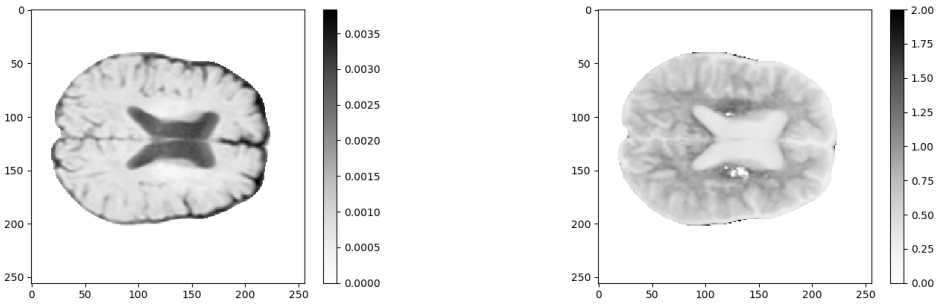

Fig 3.17: *Mean Signal Diffusivity (Left) and Mean Signal Kurtosis (Right).*

3.3.4 WMTI (using DIPY)

The white matter tract integrity (WMTI) model is built upon DTI and DKI and provides two parameters that are considered to represent intra- and extra-axonal compartments.
The output variables are:

`AWF`	axonal water fraction
`TORT`	diffusion hindered tortuosity

Diffusion extra-cellular tortuosity (TORT) is thought to help distinguish processes of axonal loss from processes of myelin degeneration [57].
The values of AWF and TORT are not available throughout the whole volume as these values can only provide useful information in regions with well aligned fibers. On Fig.3.18, are displayed the AWF and TORT in the regions selected as well aligned following the instructions in `DIPY` : regions with selected values based on diffusion sphericity, planarity and linearity.

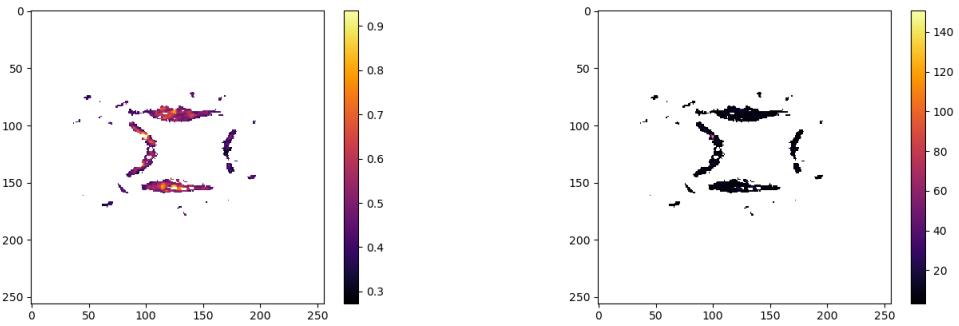

Fig 3.18: *Limited region of analysis of axonal water fraction (left) and tortuosity (right).*

3.3.5 NODDI

The NODDI model was applied to the data using the "Quantitative Imaging Toolkit" (*QIT*) program [58].

The model outputs 5 volumes:

`baseline`	a base volume similar to a b0 scan
`noddi_fibredirs_*vec`	three files containing the fiber directions along the x, y and z axis
`ficvf`	intracellular volume fraction, *NDI* (neurite density index) equivalent
`fiso`	free water volume fraction
`irfrac`	restricted compartment volume ratio/isotropic restricted fraction
`odi`	fiber orientation dispersion index

The `irfrac` volumes generated are zero, they will not be taken into account during the analysis process.
The `odi` parameter is linked to the κ parameter (see Section 1.3.1). It ranges between [0,1] and increases with higher orientation dispersion of the neurites.
The different outputs are displayed in Fig.3.19. A visual inspection tells us that the results obtained are coherent with the biological truth: the neurite density is higher in regions where there are major white matter tracts (such as the corpus callosum), the free volume fraction is at its highest in the CSF and the fiber orientation dispersion index is low in the white matter.

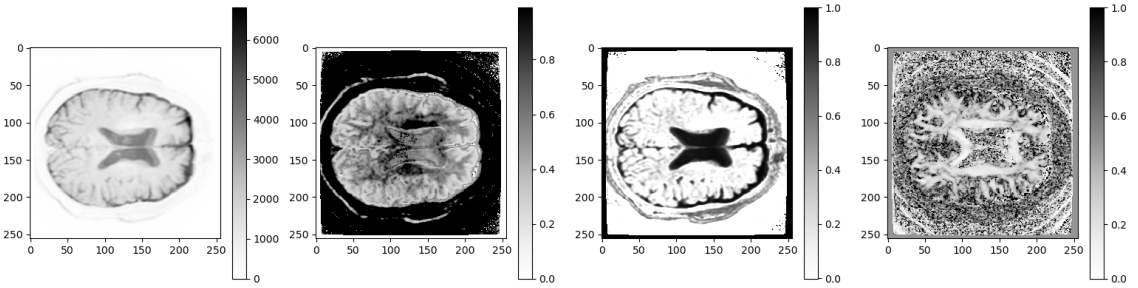

Fig 3.19: *NODDI output : baseline (Extreme Left), intracellular volume fraction (Left), isotropic restricted fraction (Right) and fiber orientation dispersion index (Extreme Right).*

3.3.6 DIAMOND

This section covers the input parameters and ouputs of the DIAMOND model by Benoit Scherrer [21]. More information about the concepts behind DIAMOND can be found in Section 1.3.2.

Here are the input parameters used:

`-m`	Mask of the region to be analyzed, in this case a white matter mask was used as DIAMOND is not made to fit grey matter.
`-n`	Maximum number of tensor to be fit in each voxel, `2` was used.
`-automose`	Model selection parameter. The DIAMOND model will decide the number of effective tensors in each voxel, `aicu` was used. If no input model is specified, each voxel will have `n` tensors regardless.
`-p`	number of processors to be used
`-predictedsignal`	reconstruction of the original input signal (output)
`-omtm`	intermediate tensor estimation (output)
`-mosemask`	mask specifying the number of tensor in the volume

An example of the full command line can be found in Appendix C.3. The output files received are:

`aicu`	Automose model selection map. Grey and white matter correspond to positive values and CSF to negative values
`b0`	Volume with a b-value of 0
`dti`	DTI estimate
`fractions`	Fraction of voxel attributed to each compartment, $\sum = 1$
`freewater_diffusivity`	Diffusivity of the free water compartment
`hei`	The respective heterogeneity indexes for each layer
`kappa`	Concentration/Homogeneity index
`logKappa`	Log of `kappa`
`mosemap`	Number of fascicles in each voxel (<=`n`)
`mtm_fractions`	Intermediary step of the `fractions` output
`mtm_t0`	Intermediary step of the `t0` output
`mtm_t1`	Intermediary step of the `t1` output
`t0`	Tensors of the first fiber population
`t1`	Tensors of the second fiber population

`hei` and `kappa` both represent the fiber's orientation heterogeneity of a compartment although their correlation are inverted : hei increases with the heterogeneity and kappa κ decreases with increasing heterogeneity.
Hei and kappa are linked by the formula

$$HEI = \frac{2}{\pi} arctan(\frac{1}{\kappa}). \tag{3.1}$$

Additionally, other classic variables such as FA, MD, RD and AD can be extracted from the `t0` and `t1` values using *MisterI*, a software also developed by Benoit Scherrer to display the output of DIAMOND (available at [59]).
These values differ from the values obtained using the DTI model since the different fiber populations existing in a single voxel are taken into account rather than deriving the FA from the "mean" signal output of a voxel. For instance, if two identical, but perpendicular, fiber populations are crossing each other in a voxel, the FA derived from DTI models will most likely deduce that the FA is 0, whereas the total FA derived from DIAMOND will display values closer the "real" FA values of the fibers present in the voxel.

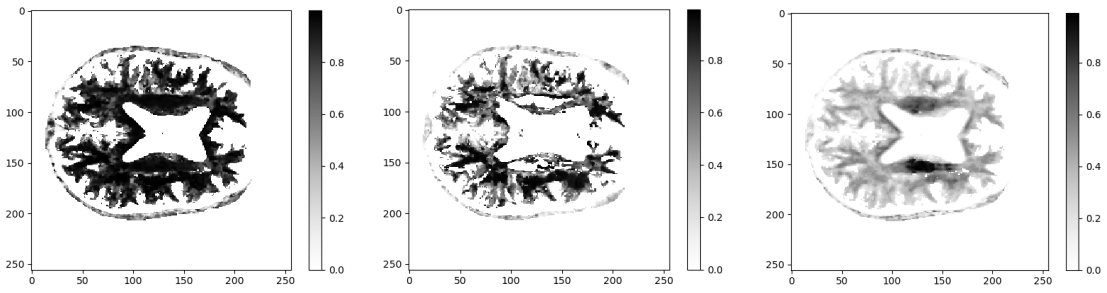

Fig 3.20: *FA of : the first fiber population (Left), the second fiber population (Middle) and the proportional sum with the extra-axonal compartment set to FA=0 (Right).*

The resulting FA, which will be called mFA in this report, is thus obtained from the following equation:

$$mFA = cFA_{pop.1} * fraction_{pop.2} + cFA_{pop.2} * fraction_{pop.2} \tag{3.2}$$

The FA of two fiber population compartments can be seen in Fig.3.20 as well as a sum of all FA values across the two fiber populations plus an extra-axonal compartment (the FA value of this last compartment is set to 0).

3.3.7 Microstructure Fingerprinting

The model requires several inputs in addition to the classic data, b-values and b-vectors triad. The additional inputs can be obtained from the DIAMOND model, namely the fractions of the each compartments and the tensors of the fiber populations. The required inputs are listed below:

`DWIfile`	motion corrected file containing the diffusion data
`bvalfile`	file containing the b-values
`bvecfile`	file containing the b-vectors
`maskfile`	a binary brain mask
`tensor_files`	tensor files obtained from `DIAMOND`
`fractions_file`	fractions file obtained from `DIAMOND`

It has to be noted that the number of fascicles per voxel will not be exactly the same as DIAMOND despite having the fiber population tensors of DIAMOND as an input. This is due to a "fascicle clean up" by the microstructure fingerprinting model which will set the fraction of a fiber population to 0 if it is close to 0.
The output of the microstructure fingerprinting model are the following files:

`D_ear`	diffusivity in the extra-axonal restricted compartment
`frac_ear`	fraction of the extra-axonal restricted compartment
`frac_f0`	fraction of the first fascicle compartment
`frac_f1`	fraction of the second fascicle compartment
`fvf_f0`	fiber volume fraction of the first fascicle (the fraction of water inside the simulated cylinders)
`fvf_f1`	fiber volume fraction of the first fascicle
`fvf_tot`	total fiber volume fraction of both fascicles
`M0`	the multiplicative constant of the signal, magnetization just after the 90° RF impulse
`MSE`	mean squared error in each voxel between the predicted and measured signals: $\sum_i^N (y_i - y_{pred,i})^2/N$
`R2`	coefficient of determination R^2 in each voxel (squared correlation)
`rad_f0`	axonal radius of the first fascicle (radius of the simulated cylindres)
`rad_f1`	axonal radius of the second fascicle

The total fiber volume fraction of both fascicles (`fvf_tot`) (displayed in Fig.3.21-Right) is computed with the formula

$$\texttt{fvf\_tot} = \texttt{fvf\_f0} * \texttt{frac\_f1} + \texttt{fvf\_f1} * \texttt{frac\_f1}. \tag{3.3}$$

The radii output (`rad_f0` and `rad_f1`) should be interpreted with caution as the diffusion sequences used in our experiments do not provide sufficient sensitivity to this parameter.
Some of the metrics output from the microstructure fingerprinting model are shown in Fig.3.21. In the left side of the figure, the diffusivity in the extra-axonal restricted compartment (`D_ear`) is represented. The values range from 0 to 3.10^{-9} [m^2/s], which corresponds to the diffusivity value of the CSF. The fraction of the extra-axonal restricted compartment (`frac_ear`) is represented in the middle of the figure, there is a sharp contrast in values due to the fact that voxels that were not considered as white matter by the *DIAMOND* model (from which the tensors used in this model were extracted) are considered to be entirely modeled by an isotropic diffusion, with a fraction of 1.

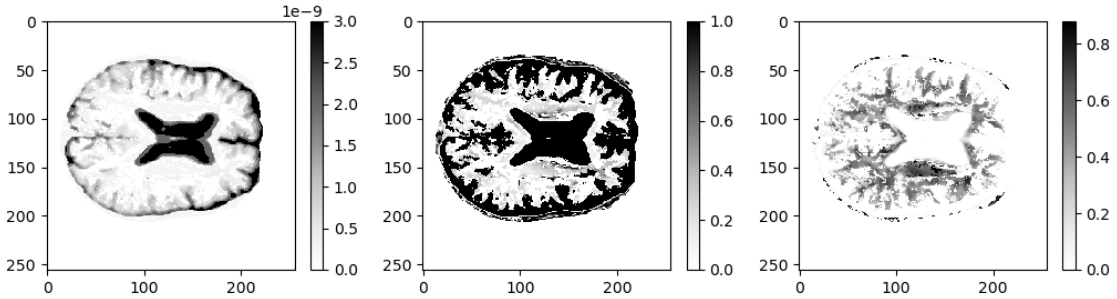

Fig 3.21: *Microstructure fingerprinting output: diffusivity in the extra-axonal restricted compartment (Left); fraction of the extra-axonal restricted compartment (Middle); total fiber volume fraction of both fascicles (Right).*

Chapter 4

Results

This chapter covers the evolution of the mean values of the metrics described in the previous chapter, in the 22 regions listed in Section 3.2.5, during alcohol abstinence. An additional analysis of the DIAMOND model on children with cerebral palsy can be found in Appendix A.
Visual representations of the values obtained were used throughout this chapter to make it more readable. However, due to the nature of the results presented, this chapter is rather repetitive.

4.1 Single-compartment models (DKI, MSDKI, WMTI)

The models available in the `DIPY` library were implemented to obtain volumes of the different metrics (FA, MD, MK, ...) described in Section 3.2. Since the patient was scanned before and after the two-week abstinence period from alcohol, those volumes can be compared and the evolution of the different metrics can be observed.

The comparison between the two volumes was conducted in two main approaches: a visual comparison of the whole white matter volume after registration and a region-based analysis.
The first comparison is mostly visual, it displays the differences in values throughout the white matter, either using a white matter mask or with an equivalent (more details about the mask will be provided in the following sections).
The region-based analysis provides a more quantitative analysis, with the evolution of the values in specific brain regions (specified in Section 3.2.5).

White matter mask

The white matter mask was made by keeping the intersection of the two registered volumes after having applied a FA threshold on both volumes. This means that the visual differences were only visible in regions where the FA was above 0.3 in both volumes (this specific value was chosen based on the visual output it produced and can be modified as necessary). The advantage of this method is that it allows to "clean up" the figures by visually removing the sections where the white matter

regions do not exactly overlap, therefore avoiding noise to come up at the borders of these sections. Ideally the white matter mask would be done by hand using `MRIcron`, or any other program that can draw regions of interest, but this tasks is time consuming and has to be repeated for each different scan. The method used is automated and thus bypasses this manual step while keeping some biological relevance. Indeed, white matter regions are characterized by higher FA values than grey matter or cerebral fluids.
An example of such a *FA skeleton* mask can be seen in Fig.4.1. As desired, the mask created is roughly equivalent to the white matter area.

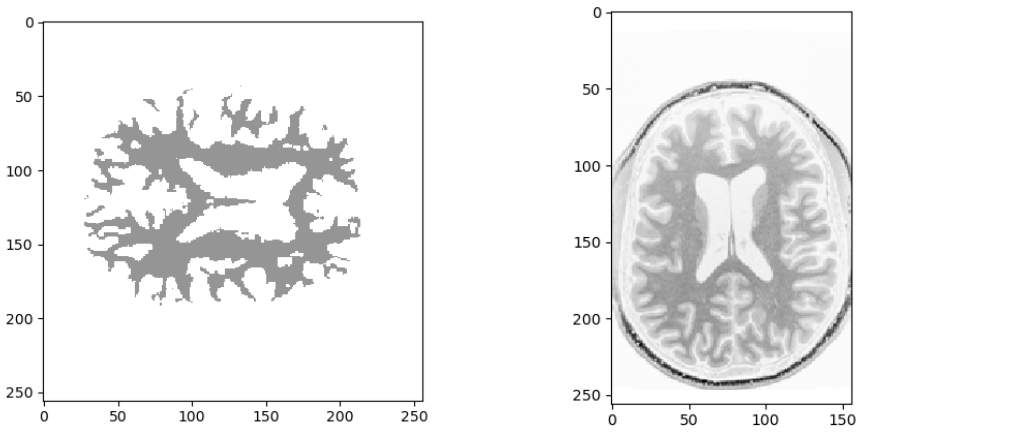

Fig 4.1: *White matter mask equivalent created by selecting regions with FA values above a threshold (Left) compared to anatomical view (Right).*

4.1.1 Fractional anisotropy (FA)

FA is often considered to be a measure of axonal integrity. However, FA should be interpreted carefully due to the different tissue properties that it encompasses. It may be an indication of the density of packing of fibers in a voxel, and the amount of myelin wrapping these axons. However, FA may decrease in locations in which there is a crossing of white matter fibers. It is thus not limited to a measure of tissue integrity. For more information about the computation of FA, see Section 1.2.2. The FA presented here was obtained with the DKI model.

In Fig.4.2 is displayed the evolution of the FA after the two-week abstinence period. The difference in values was calculated by subtracting the values before abstinence (T0) from the values obtained after (T1)

$$\Delta FA = FA(T1) - FA(T0). \tag{4.1}$$

The values are thus positive (represented in orange/red) if the metric has increased after abstinence and negative (in blue) if the metric has decreased. Areas with a low amount of changes are characterized by a grey coloration.
As observed in Fig.4.2, the FA values increased throughout the white matter regions. The possible value of FA being between 0 and 1, the observed change of values being

close to 0.4 could prove to be quite significant.

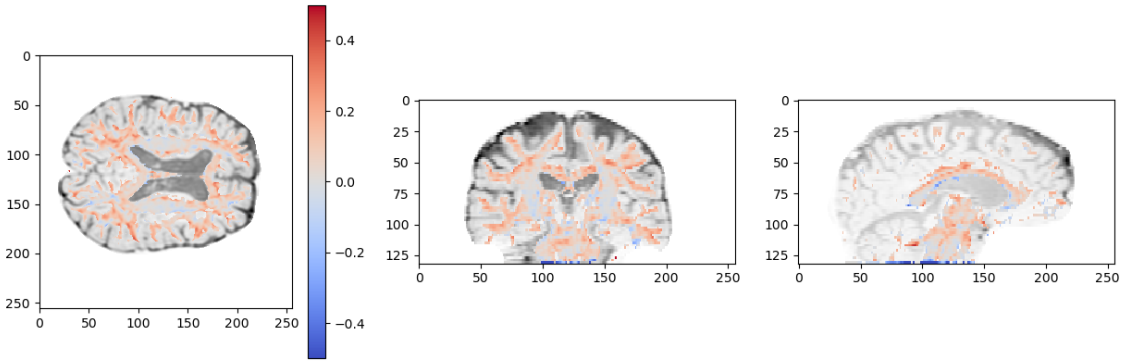

Fig 4.2: *Difference in FA values in the white matter before and after abstinence, superimposed on a b0 scan. Axial view (Left), coronal view (Middle) and sagittal view (Right). Red pixels correspond to an increase and blue pixels to a decrease after abstinence.*

During the rest of this section, figures such as Fig.4.2 will display the slices at x=115, y=115 and z=30 unless specified otherwise. The initial dimensions of the volume were x:256, y:256, z:66/68. The z direction was stretched by duplicating each line in the figures to better represent the shape of the brain.

When looking at a region-based analysis (see Section 3.2.5), similar results are found: the FA increased or stagnated in all of the 22 regions studied, as displayed in Fig.4.3. The complete table of the means and standard deviations for every region in every metric is available in Appendix C.4.

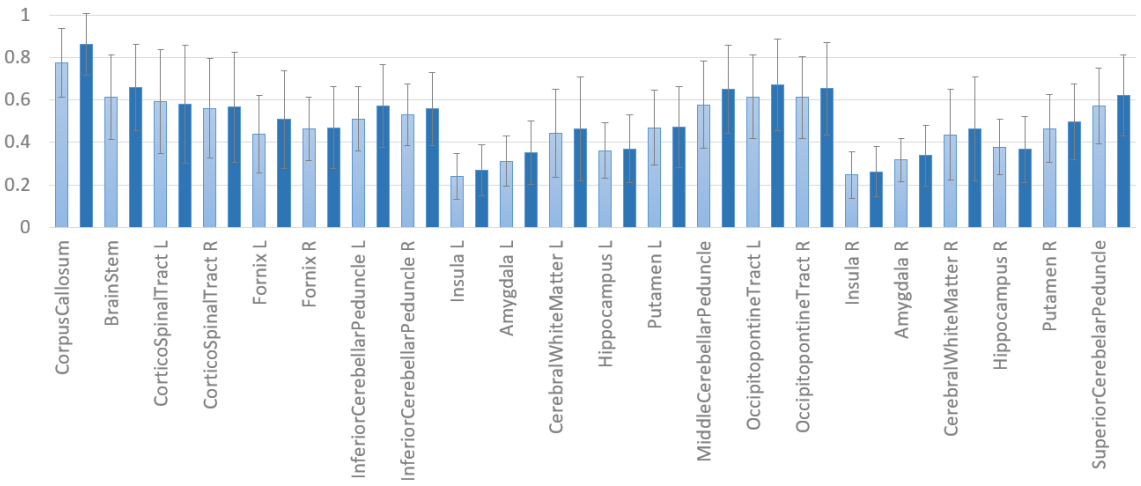

Fig 4.3: *Mean of the fractional anisotropy within each region before (T0, light blue) and after (T1, dark blue) abstinence.*

To make the results stand out more, it is possible to extract the difference between T0 and T1 from each region and divide it by the initial value (in T0) to obtain the percentage change of the means. The percentage change is thus given by the formula

$$\text{FA Percentage change} = \frac{FA(T1) - FA(T0)}{FA(T0)}\text{x}100. \tag{4.2}$$

The percentage changes for FA are displayed in Fig.4.4.

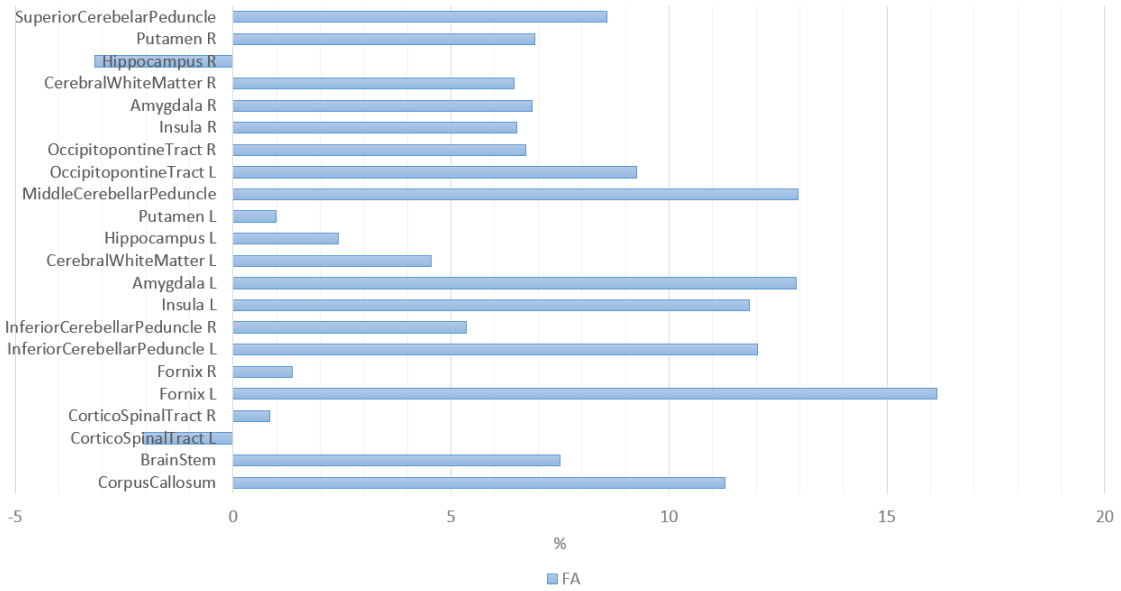

Fig 4.4: *Percentage change in FA values between before and after abstinence.*

From these graphs, it can be extracted that FA did indeed increase throughout most of the whole white matter volume, especially in the fornix (left), corpus callosum, the inferior cerebellar peduncle (left), the insula (left), amygdala (left) and the middle cerebellar peduncle.
As mentioned in Section 3.2.5, caution has to be applied when extracting conclusions from these regions due to the inaccuracies of the masks used for the small regions. As displayed in Fig.4.4, the large differences between left and right hemispheres (such as in the fornix region) might have been an indicator of these inaccuracies rather than the biological truth.

4.1.2 Diffusivity

The three metrics listed in this section all characterize the diffusion of the water molecules in a voxel. The more the molecules move around, the higher the diffusion. MD is thus often considered to white-matter damage. AD represents the water diffusivity parallel to the axonal fibers, which means that altered AD values may reflect axonal swelling, degeneration or deletion. RD represents the water diffusivity perpendicular to the axonal fibers. Altered RD may reflect myelin disruption.
For more information about the computation of these three metrics, see Section 1.2.2. The metrics MD, RD and AD presented here were obtained with the DKI model.

Axial diffusivity (AD)

In similar fashion, a white matter map with the differences in axial diffusivity can be obtained, see Fig.4.5. Visually, the AD seemed to decrease in most areas.

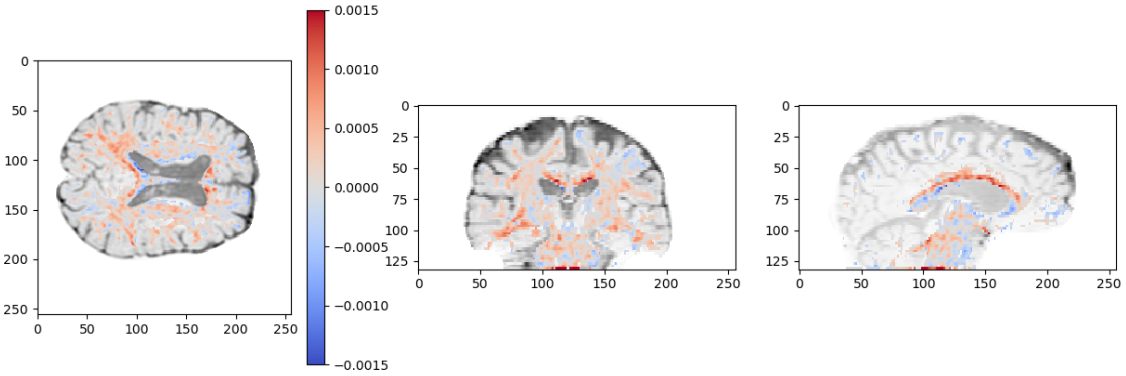

Fig 4.5: *Difference in AD values in the white matter before and after abstinence, superimposed on a b0 scan. Axial view (Left), coronal view (Middle) and sagittal view (Right). Red pixels correspond to an increase and blue pixels to a decrease after abstinence.*

Radial diffusivity (RD)

The radial diffusivity evolution was less homogeneous with some regions showing an increase and others a decrease. Visually, the main tendency seemed to be a decrease in RD, as displayed in Fig.4.6.

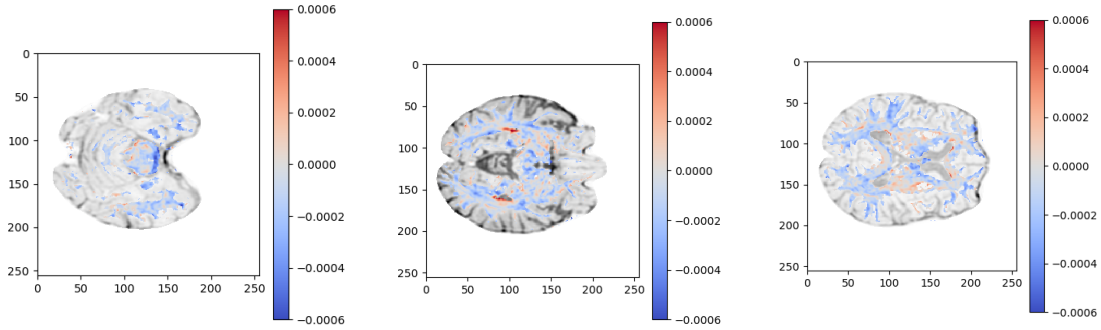

Fig 4.6: *Difference in RD values in the white matter before and after abstinence, superimposed on a b0 scan. z=10 (Left), z=17 (Middle) and z=25 (Right). Red pixels correspond to an increase and blue pixels to a decrease after abstinence.*

Mean diffusivity (MD)

The mean diffusivity differences are displayed in Fig.4.7.
However, since MD is a combination of AD and RD (see Section 1.2.2 for more info), it gave out less information than AD and RD separately. This phenomenon is illustrated in Fig.4.8, where the percentage change of MD was close to 0 in the

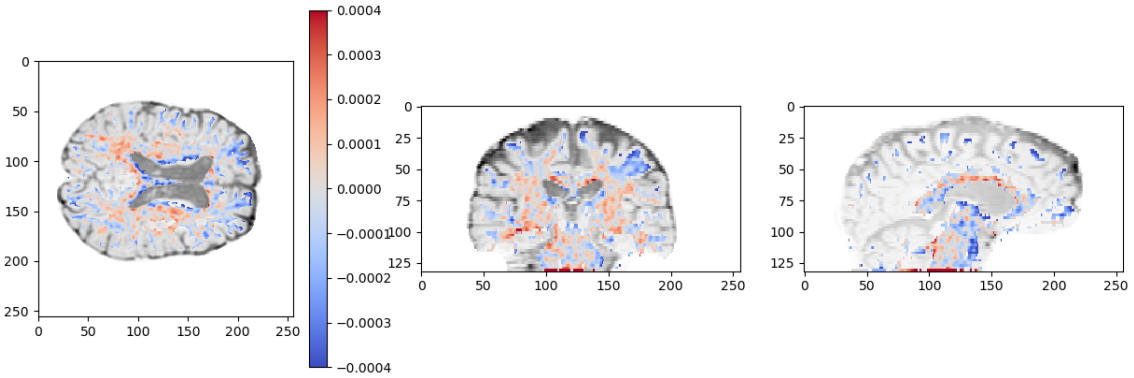

Fig 4.7: *Difference in MD values in the white matter before and after abstinence, superimposed on a b0 scan. Axial view (Left), coronal view (Middle) and sagittal view (Right). Red pixels correspond to an increase and blue pixels to a decrease after abstinence.*

CC but significantly higher when the evolutions of AD and RD were compared individually.

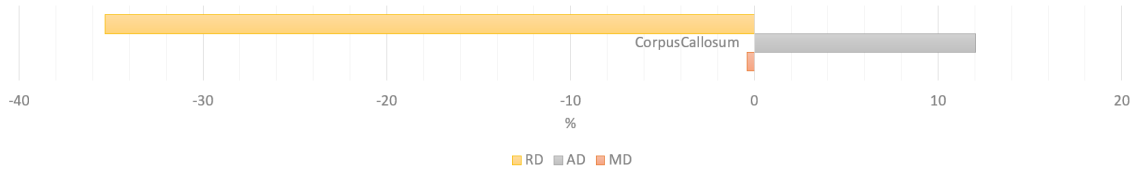

Fig 4.8: *Percentage change in MD, AD and RD values between before and after abstinence in the corpus callosum.*

For this reason, the MD was not included in Fig.4.9 with AD and RD, as the percentage change was always less than either AD or RD.
From Fig.4.9 it can be observed that the AD increased in most regions, especially in the CC, fornix (left), inferior cerebellar peduncle (inferior, middle and superior) and occipitopontine tracts.
Whereas the RD increased in the left corticospinal tract and decreased in the CC, brain stem and middle cerebellar peduncle.

4.1.3 Kurtosis

As mentioned in Section 3.3.2, kurtosis represents the non-Gaussian behaviour of the diffusion signal, which is expected to be higher when tissue water is confined by multiple compartments. MK is, therefore, higher in white matter since it is highly compartmentalized by myelin sheaths. This restricted water diffusion is expected to be more pronounced perpendicularly to white matter fibers.The RK maps thus present higher amplitudes than the AK maps.
The mean kurtosis depends on the information of both diffusion and kurtosis tensor.

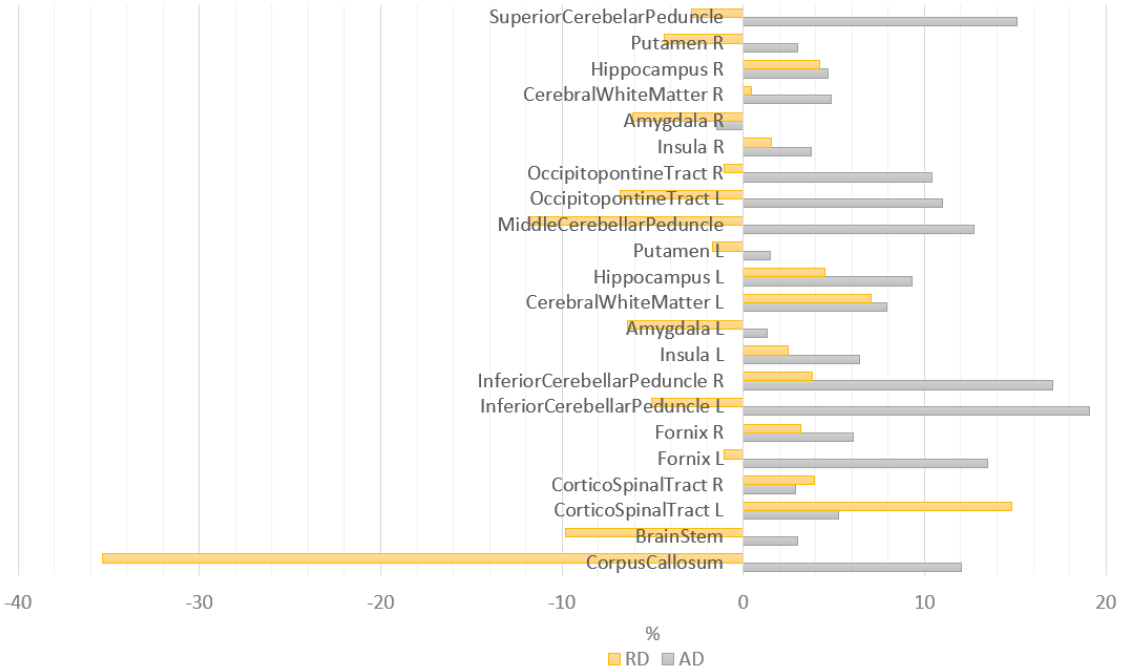

Fig 4.9: *Percentage change in AD and RD values between before and after abstinence.*

Axial kurtosis (AK)

The differences in axial kurtosis are displayed in Fig.4.10.

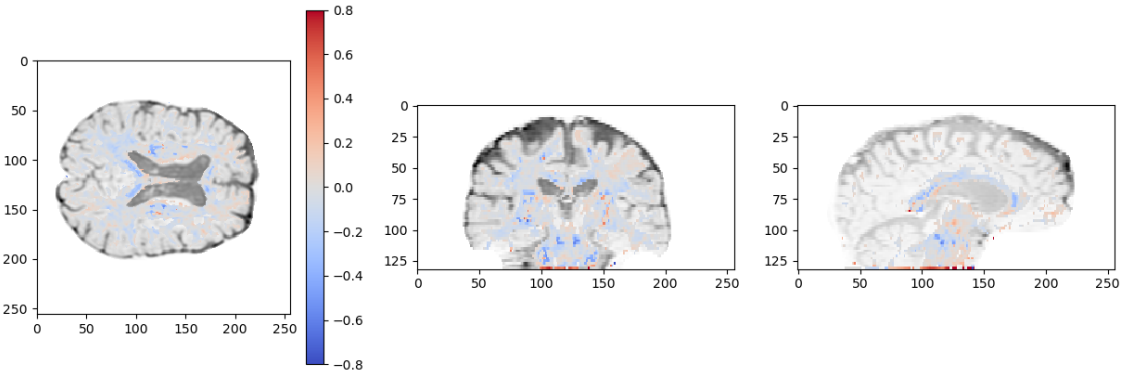

Fig 4.10: *Difference in AK values in the white matter before and after abstinence, superimposed on a b0 scan. Axial view (Left), coronal view (Middle) and sagittal view (Right). Red pixels correspond to an increase and blue pixels to a decrease after abstinence.*

Radial kurtosis (RK)

Since the RK volumes presented zones where the values were missing/inaccurate due to the algorithm used to compute these values (see Fig.3.15-Middle), caution has to be exercised when using these results. As shown in Fig.4.11, regions with such artefacts (the corpus callosum for example) were characterized by large variations

(up to 2.5 of difference between T0 and T1 when the kurtosis values are in a [0,3] range) and thus had to be removed when interpreting the results.

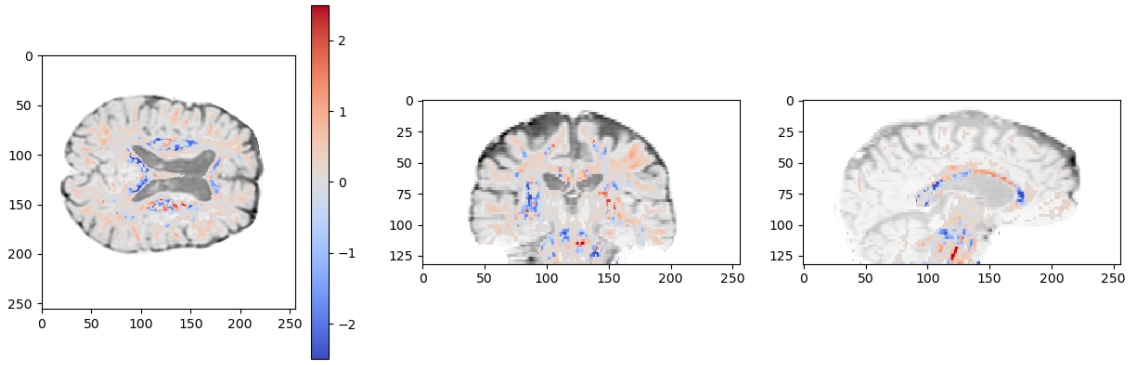

Fig 4.11: *Difference in RK values in the white matter before and after abstinence, superimposed on a b0 scan. Axial view (Left), coronal view (Middle) and sagittal view (Right). Red pixels correspond to an increase and blue pixels to a decrease after abstinence.*

Mean kurtosis (MK)

The MK (displayed in Appendix D.2, Fig.D.3) suffers from the same disadvantages as MD as well as the artefacts from the RK values. Its significance is thus rather low compared to other metrics.

Mean kurtosis tensor (MKT)

The mean kurtosis tensor is another output of the DKI model. The maps representing the difference after abstinence in Fig.4.12 showed that some regions experienced an increase whereas others displayed a decrease.

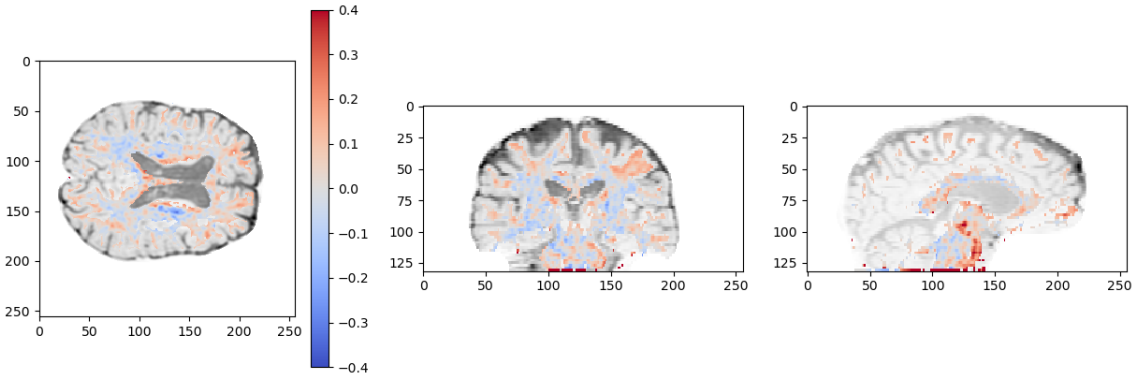

Fig 4.12: *Difference in MKT values in the white matter before and after abstinence, superimposed on a b0 scan. Axial view (Left), coronal view (Middle) and sagittal view (Right). Red pixels correspond to an increase and blue pixels to a decrease after abstinence.*

The visual comparison of the other metrics output from the DIPY models are available in Appendix D.2. They were not included in the main document because they were either redundant with other metrics (such as MK, KFA) or less clear overall.

Region-based analysis

As seen in Fig.4.13, most regions displayed a decrease in AK and an increase in RK. The region with the biggest percentage change in AK was the left inferior cerebellar peduncle. On the other hand, the biggest changes in RK were observed in the corpus callosum and the middle cerebellar peduncle. The MKT percentage change was not included in the graph as the observed changes were less significant than for the other two metrics.

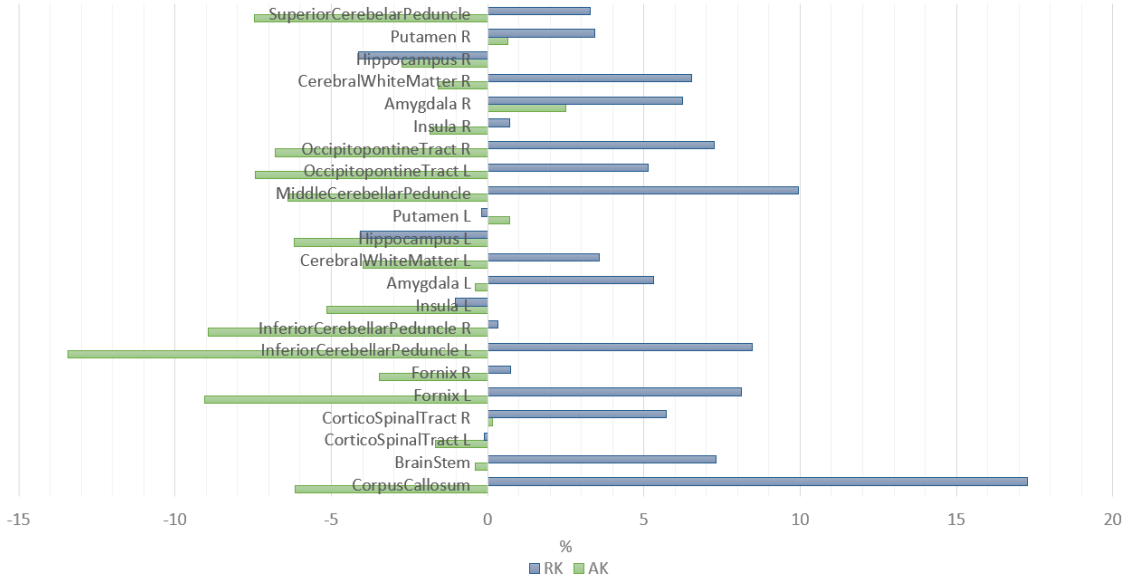

Fig 4.13: *Percentage change in AK and RK values between before and after abstinence.*

4.1.4 Axonal water fraction (AWF)

The two metrics of the WMTI model are limited in the regions where they can be extracted since they only provide accurate information in voxels with well-aligned fibers (see Section 3.3.4 and Fig.3.18).
Furthermore, the tortuosity metric TORT was not taken into account during this analysis since it presented a standard deviation up to ten times its mean value in most regions.

One of the few regions where the AWF could be analyzed was the corpus callosum, the results are shown in Table 4.1.

	Corpus callosum	
	T0	**T1**
AWF mean	0.497	0.553
AWF standard deviation	0.115	0.109

Table 4.1: *Mean and standard deviation of axonal water fraction (AWF) before (T0) and after (T1) abstinence in the corpus callosum.*

4.2 NODDI

White matter mask

Similarly to Section 4.1 a white matter mask equivalent was made to compare the metric values throughout the whole white matter volume.
This time the mask was made by intersecting two registered binary masks keeping values that were below a certain orientation dispersion index (`odi`, see Fig.3.19, far right) threshold. The fiber orientation dispersion index is low in regions where fibers are well aligned, making it a white matter mask equivalent.

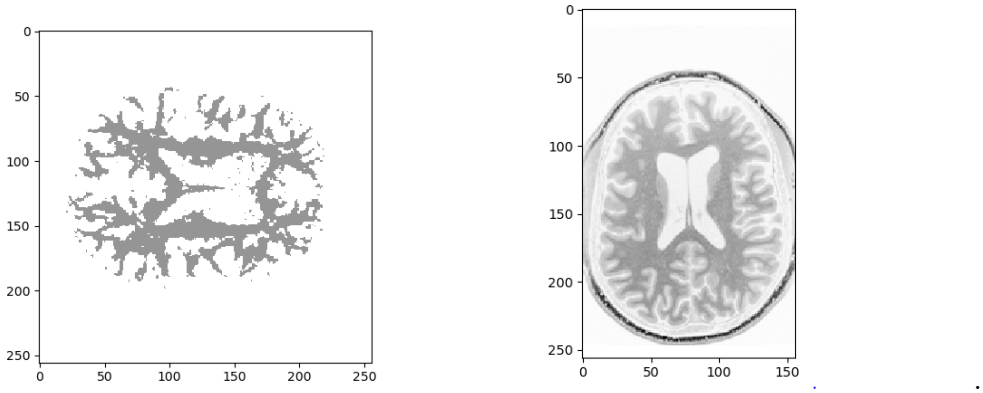

Fig 4.14: *White matter mask equivalent created by selecting regions with ODI values below a threshold (0.5) (Left) compared to anatomical view (Right).*

4.2.1 Intracellular volume fraction

The intracellular compartment can be interpreted as the space bounded by the membrane of neurites. The intracellular volume fraction difference before and after abstinence is displayed in Fig.4.15, the red areas indicate an increase after the abstinence period and the blue ones a decrease of the metric.
Overall the intracellular volume fraction seemed to have increased throughout the whole volume (such as in the corpus callosum) but some areas did present a decrease (such as to the left and right of the CSF).

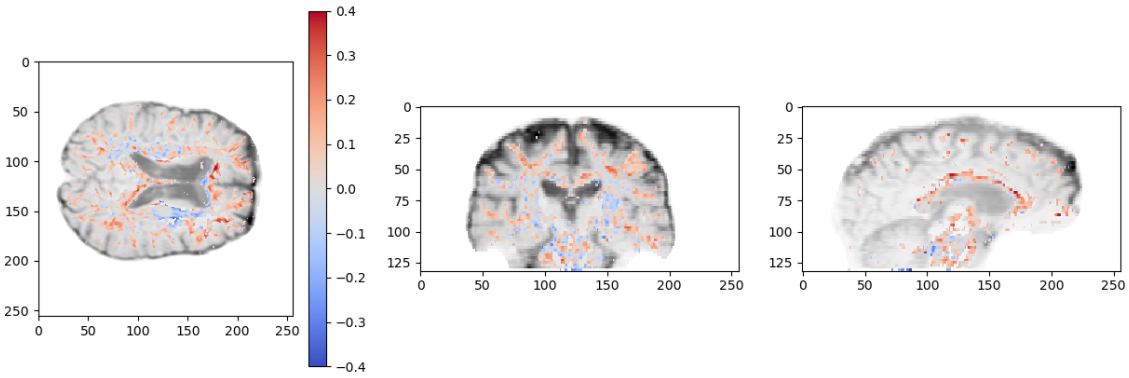

Fig 4.15: *Difference in intracellular volume fraction values in the white matter before and after abstinence, superimposed on a b0 scan. Axial view (Left), coronal view (Middle) and sagittal view (Right).*

4.2.2 Free water volume fraction

The free water compartment models the space with an isotropic diffusion and is thus modeled as isotropic Gaussian diffusion with diffusivity d_{iso}.
The free water volume fraction differences are displayed in Fig.4.16. The fraction seemed to increase in most areas and decreased in others such as the CC and part of the brain stem.

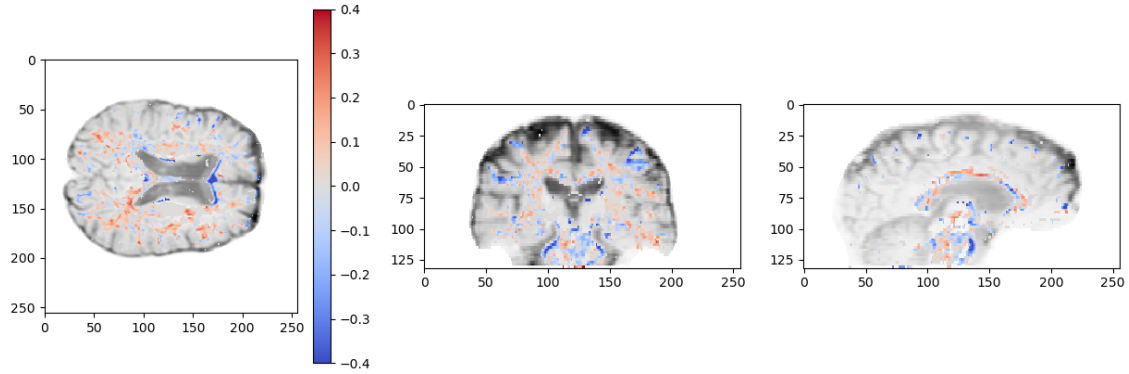

Fig 4.16: *Difference in free water volume fraction values in the white matter before and after abstinence, superimposed on a b0 scan. Axial view (Left), coronal view (Middle) and sagittal view (Right).*

The region-based analysis yielded similar results: the free water volume fraction increased greatly in the amygdala, insula and hippocampus, decreased in the CC, brain stem and parts of the cerebellar peduncle, whereas the intracellular volume fraction increased in the CC, insula and amygdala.

4.2.3 Fiber orientation dispersion index

When looking at the fiber Orientation Dispersion Index (ODI) of the neurites, it can be observed that most regions experienced a decrease in orientation dispersion, as

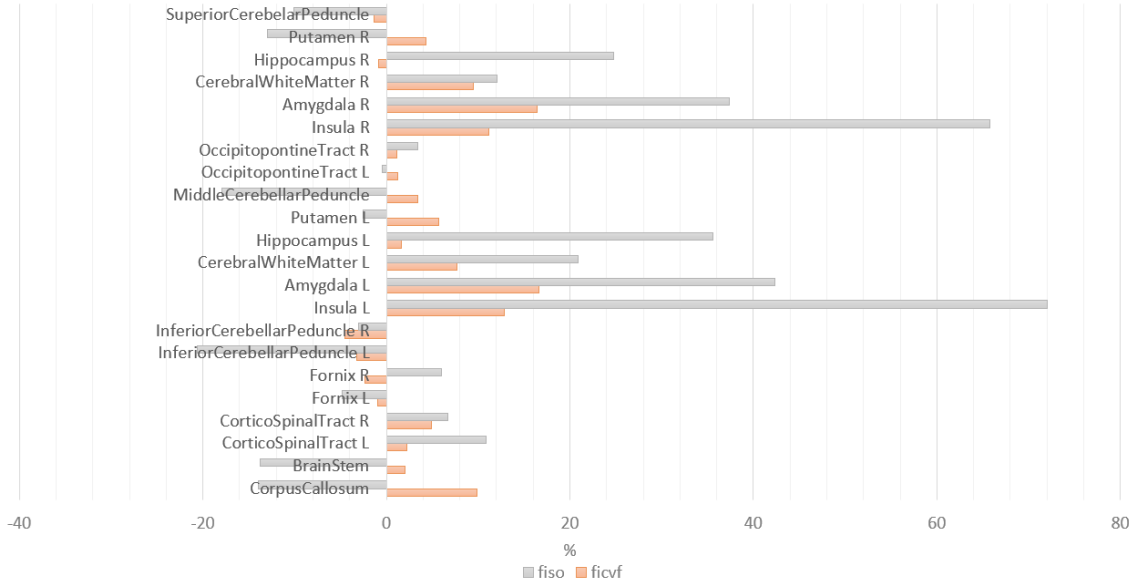

Fig 4.17: *Percentage change in free water volume fraction (fiso) and intracellular volume fraction (ficvf) values between before and after abstinence.*

displayed in Fig.4.18. For more information on the ODI metric please see Section 1.3.1 and 3.3.5.

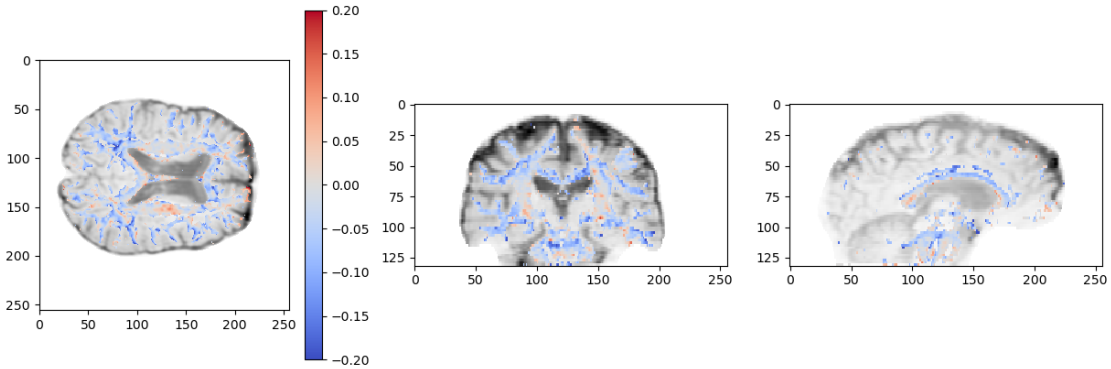

Fig 4.18: *Difference in fiber orientation dispersion index values in the white matter before and after abstinence, superimposed on a b0 scan. Axial view (Left), coronal view (Middle) and sagittal view (Right).*

This decrease is coherent with the percentage change graph (displayed in Fig.4.19), where a strong decrease in ODI was found in the Corpus Callosum (CC), cerebellar peduncles (superior, middle and left side of the inferior) and occipitopontine tracts. There was also a slight increase in the corticospinal tracts, which could correspond to the small orange area on the axial view in Fig.4.18.

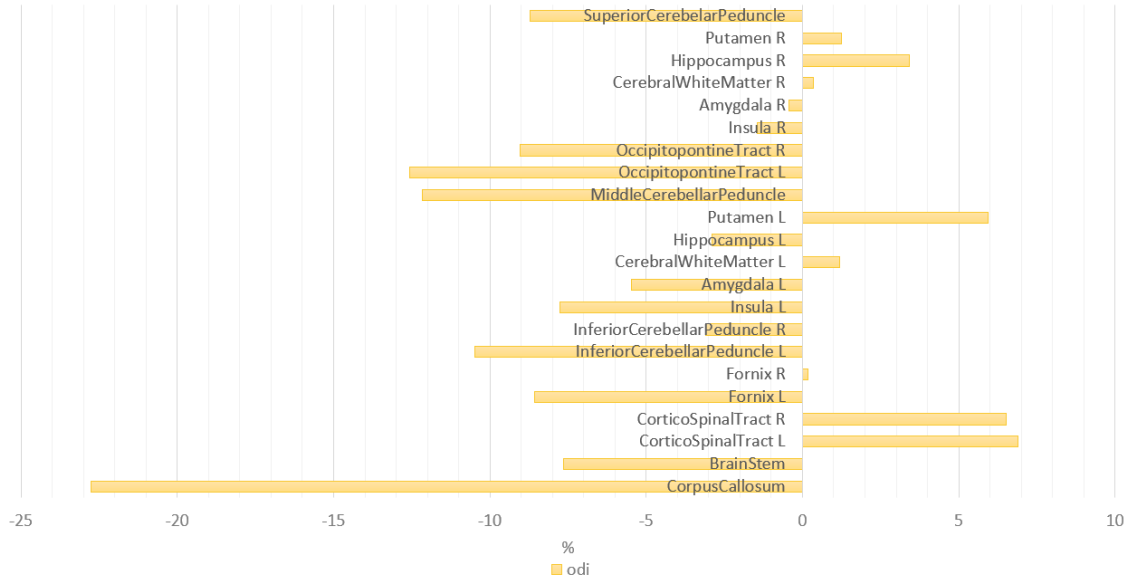

Fig 4.19: *Percentage change in fiber orientation dispersion index (ODI) values between before and after abstinence.*

4.3 DIAMOND

4.3.1 Attributed number of fascicle per voxel

The DIAMOND model outputs a `mosemap` (short for "model selection map") which allows to see the number of fascicles attributed to each voxel, see Fig.4.20. These values vary between 0, 1, 2 and 3, with the maximum number of fascicle depending on the input parameters (see Section 3.3.6). Looking at the mosemaps, it can be seen that a "single fascicle" model was selected by DIAMOND to represent the diffusion in most of the corpus callosum. This observation allows us to check that, at a first glance, the DIAMOND model has biologically sound results. Since the corpus callosum is characterized as a region with a fairly homogeneous fiber orientation, the fiber population should be mostly represented as having a single direction. It is also possible to check that the number of fascicles per region stays in the same range across scans. As shown in Table.4.2, these values remained more or less constant before (T0) and after abstinence (T1) in the selected regions: for example, the CC and superior cerebellar peduncle. Most of the regions analyzed during this section had a mean number of fascicle close to 2, with the CC having the lowest region mean at 1.27.

	T0	**T1**
Corpus callosum	1.27	1.31
Superior Cerebellar peduncle	1.98	1.99

Table 4.2: *Table of the mean number of fascicle per voxel attributed in a region.*

Contrarily to the "before" scan, the registered volume of the patient after the abstinence period (Fig.4.20 (right)) did not only display integer values (0, 1 and 2) but

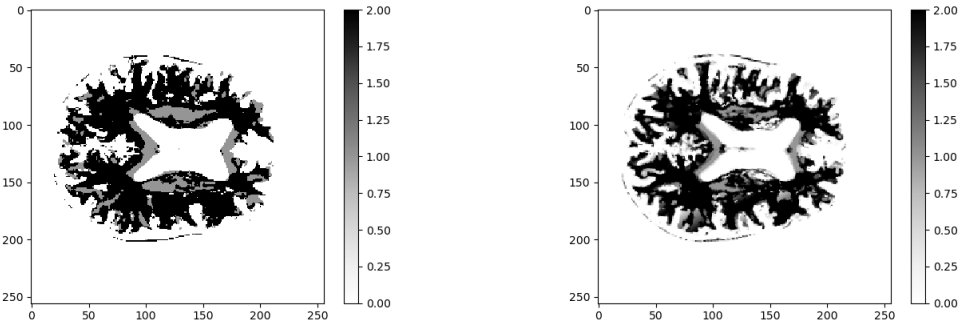

Fig 4.20: *Mosemaps of the same patient before (left) and after abstinence from alcohol (right). The "after" scan has been registered into the same space as the "before" scan.*

also values such as 1.28 or 0.79 due to the registration process. This will have to be handled with care when comparing the two volumes.

White matter mask

Since Diamond only fits tensors in regions where it detected white matter, the maps created (more specifically, `mosemap`) can be used to create a white matter mask equivalent. Once again, by intersecting two registered masks, the zones where the mosemaps do not exactly overlap each other can be avoided (see Fig.4.21-Left).
The mask created was visually smaller than what would be expected of the intersection of the two mosemaps in Fig.4.20, represented in Fig.4.21-Right. This is due to the fact that the voxels which lost some of their "intensity" after the registration process were removed.

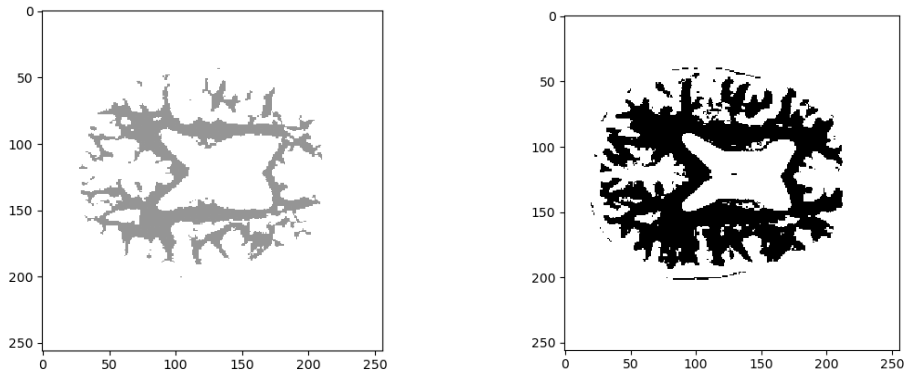

Fig 4.21: *White matter masks with: only the pixels had values above or equal to 1 after the registration process (Left) and all pixels presenting values different from 0 after registration.*

The registration process used to register the volumes can find solution where the

voxels do not lend exactly where there previously was another voxel, they can thus lend in between two voxels (see Fig.4.22). The voxel values on the edges of the binary mask will then be "diluted" within the neighboring voxels. As displayed in the right side of Fig.4.22, the registered mask can thus show values between 0 and 1.

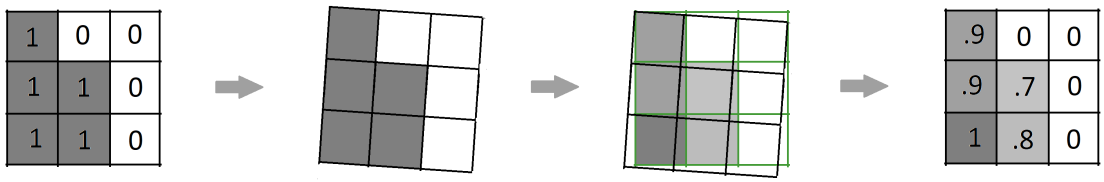

Fig 4.22: *Illustration of the "dilution" phenomenon due to the registration process. A binary mask pre-registration (Left) can obtain non-binary values after registration (Right) due to the pixels overlapping their boundaries.*

Since the analysis done in this subsection is purely visual, all the values under 1 were set to 0. This ensured that the metrics displayed were not be affected by this "dilution" effect and that the regions where the values were visually compared did not include variations due to the registration process.
Another solution would have been to set all values below 0.5 to 0 and above to 1, which would have increased the size of the mask and subsequently the area of visual comparison.

4.3.2 Freewater diffusivity

The difference in the freewater diffusivity in the white matter after alcohol withdrawal is displayed in Fig.4.23.

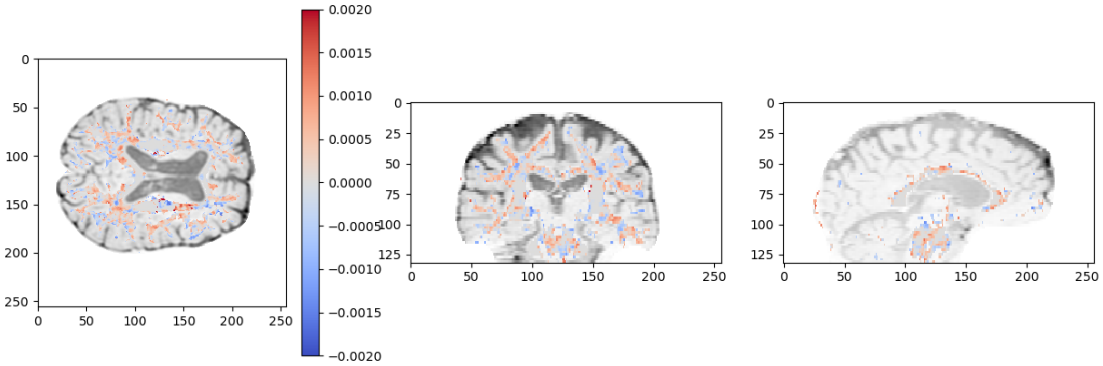

Fig 4.23: *Difference in isotropic diffusivity values in the white matter before and after abstinence, superimposed on a b0 scan. Axial view (Left), coronal view (Middle) and sagittal view (Right).*

The percentage change is displayed in Fig.4.24. The free water diffusivity seemed to decrease in the amygdala, putamen and hippocampus.

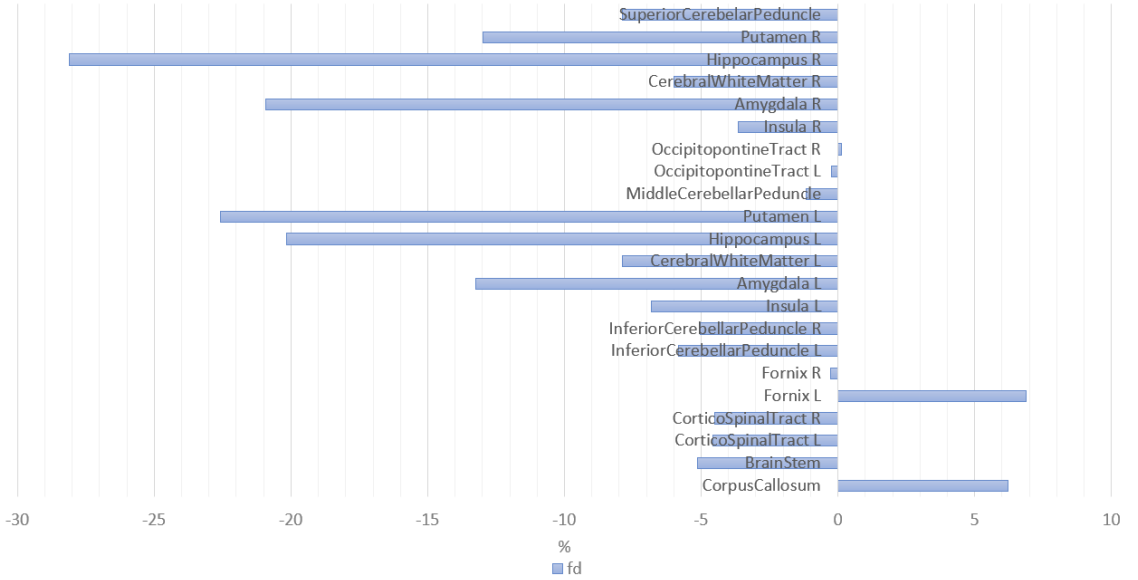

Fig 4.24: *Percentage change in free water diffusivity (fd) values between before and after abstinence.*

4.3.3 Adjusted FA

As mentioned in section 3.3.6, it is possible to compute a new FA volume (called mFA in this report) from the tensors of the two fiber populations (`t0` and `t1`). The difference in the volumes obtained before and after withdrawal are displayed in Fig.4.25. The results were similar (a global increase throughout the volume) to the ones obtained with FA, at the exception of a zone to the left (and less visibly at the right) of the CSF, which showed a decrease in mFA.
There is a clear limitation to keep in mind when interpreting those results, since DIAMOND does not output a tensor for the extra-axonal compartment, the FA of this third compartment was assumed to be null in the computation of mFA. This means that the mFA values varied when the fraction of extra-axonal compartment changed. This is visible when comparing the mFA evolution after abstinence (Fig.4.25) with the evolution of the fraction of extra-axonal compartment (Fig.4.26). They were inversely correlated, when the fraction of extra-axonal compartment increased, the mFA decreased due to a larger percentage of the mFA being set to 0.

4.3.4 Fractions of each compartment

When selecting a maximum of two fascicles and a compartment for isotropic diffusivity per voxel, a difference in the fractions of each compartment attributed in each voxel was observed. As seen in Fig.4.26, the fraction attributed to the first fiber population has increased after abstinence in regions such as the corpus callosum and decreased in the area left to the CSF. The opposite evolution happened in the the isotropic compartment with a decrease in the corpus callosum and an increase in the area to the left of the CSF. The second fiber population saw less changes overall.

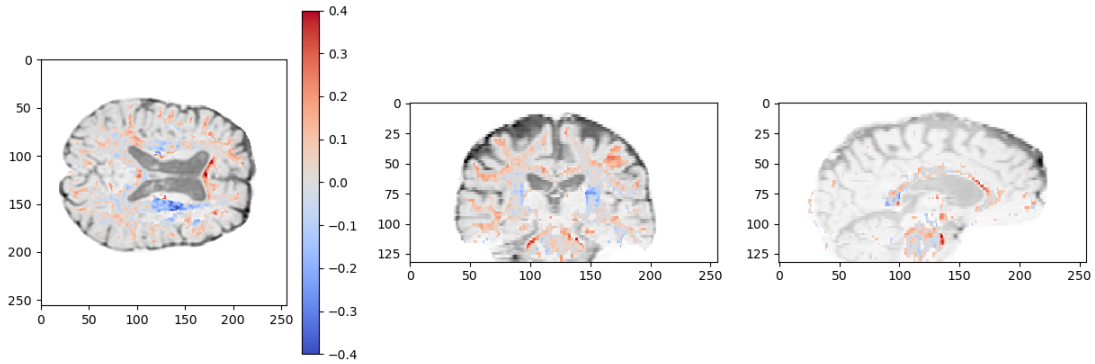

Fig 4.25: *Difference in re-computed fractional anisotropy values in the white matter before and after abstinence, superimposed on a b0 scan. Axial view (Left), coronal view (Middle) and sagittal view (Right).*

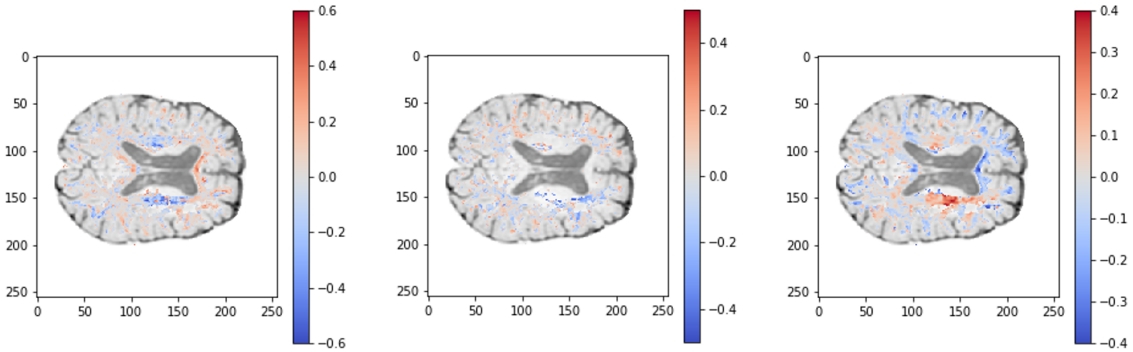

Fig 4.26: *Difference in compartment fractions before and after abstinence : fiber population 1 (left), fiber population 2 (middle) and free water (right).*

It has to be noted that the fraction of a compartment does not increase and decrease without impacting the other compartments. For example, in the corpus callosum (Fig.4.27), the increase of the fraction of the first fiber population after abstinence induces a decrease in the fraction of the other compartments. In this case, it is the extra-axonal compartment which saw its fraction reduced after the 2-week period.

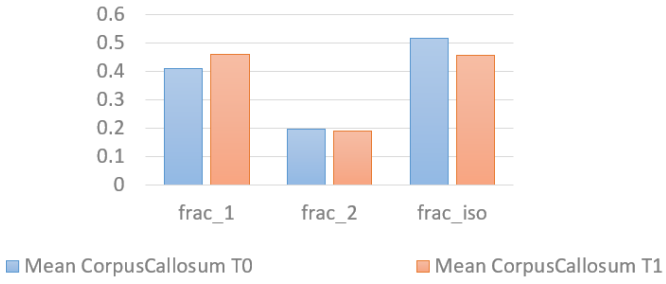

Fig 4.27: *Mean of each fraction (fraction of the first fiber population [frac_1], second fiber population [frac_2] and extra-axonal compartment [frac_iso]) in the corpus callosum before (T0) and after (T1) withdrawal.*

When looking at the percent change (displayed in Fig.4.28), it can be observed that

most analyzed regions experienced a significant increase in the fraction attributed to the first fiber population and that fractions attributed to the other two compartments mostly decreased.

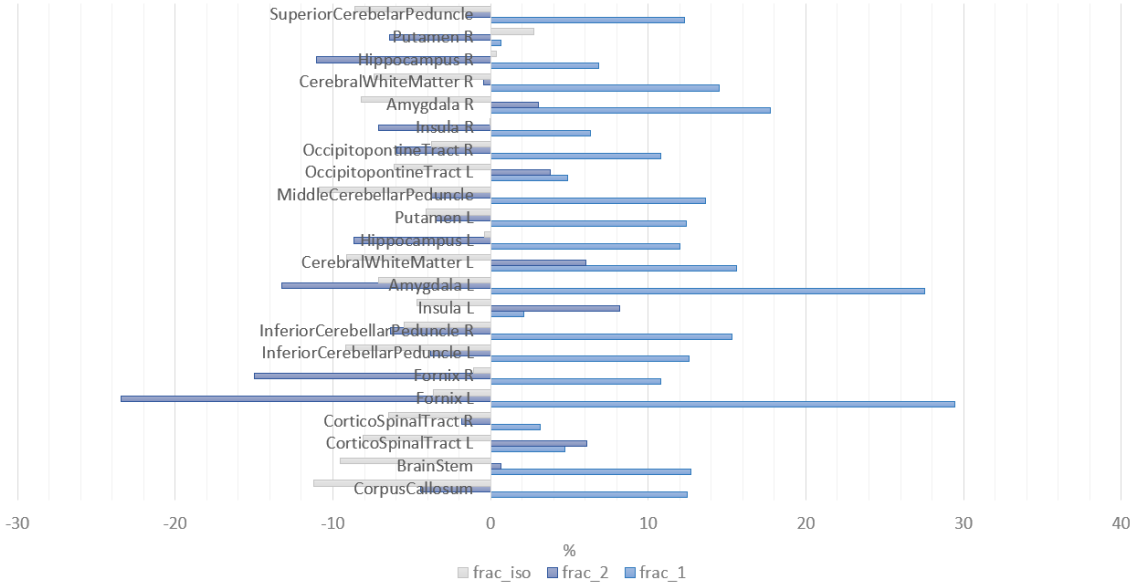

Fig 4.28: *Percentage change in the fraction of the first fiber population [frac_1], second fiber population [frac_2] and extra-axonal compartment [frac_iso] values between before and after abstinence.*

4.3.5 Heterogeneity of the compartments (HEI)

The difference in heterogeneity of the different compartments after abstinence presented a lot a of noise/variation (see Fig.4.29), rendering it difficult to identify visually which regions were the most impacted.

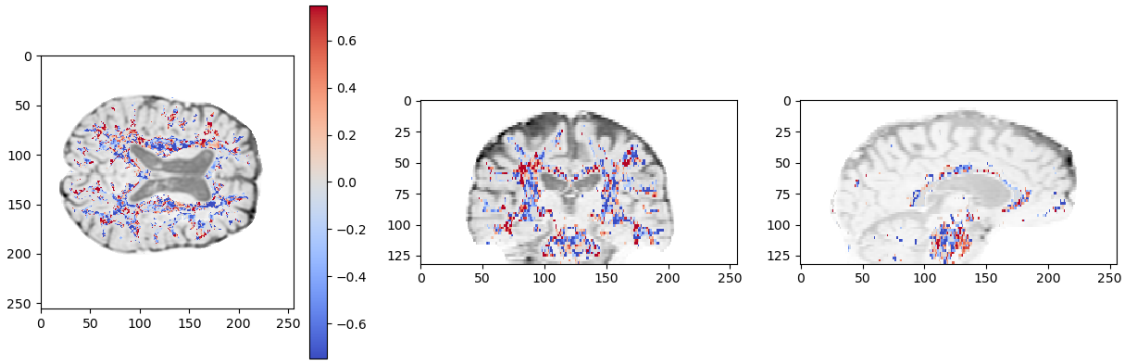

Fig 4.29: *Difference in HEI values on the first fiber population before and after abstinence. Axial view (Left), coronal view (Middle) and sagittal view (Right).*

The percentage changes in heterogeneity is displayed in Fig.4.30. Globally, the HEI seemed to have decreased in the first compartment and increased in the second. Since the extra-axonal compartment does not provide a HEI value, the change was null.

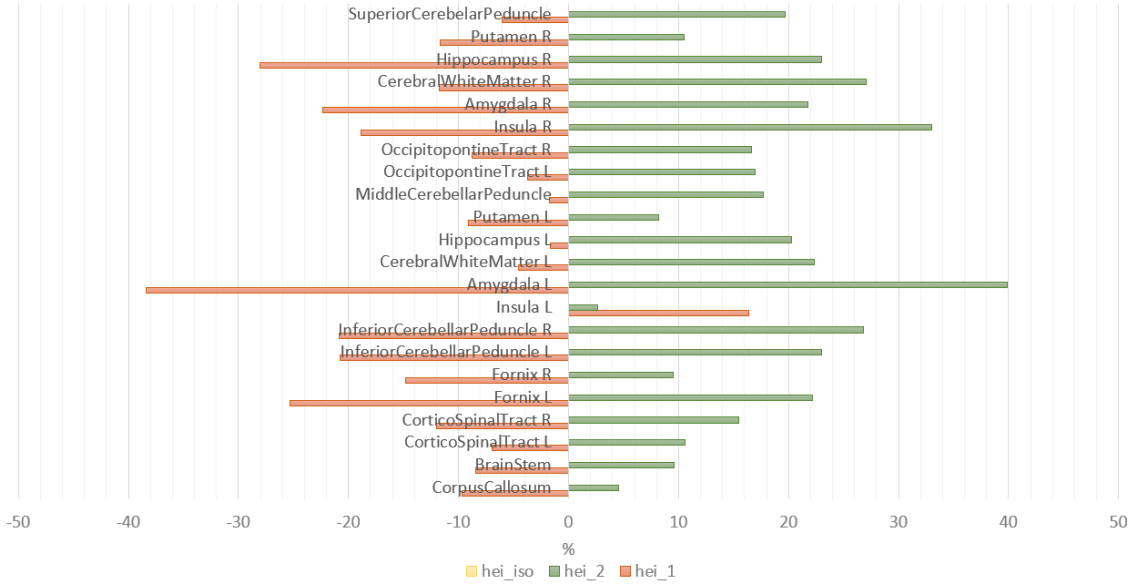

Fig 4.30: *Percentage change of heterogeneity in the first fiber population [hei_1], second fiber population [hei_2] and extra-axonal compartment [hei_iso] values between before and after abstinence.*

A limitation of this metric is its high standard deviation, which diminishes the significance of the changes observed, see Appendix D.3, Fig.D.8. Indeed, since only one patient was studied, the changes in the means observed could be due to the high variation of the values rather than an underlying microstuctural change.

4.4 Microstructure fingerprinting

The mask used for the visual comparison of the volumes was the same as the one used in the DIAMOND analysis since the microstructure fingerprinting model can re-use the tensors `t0` and `t1` found by the DIAMOND model.

4.4.1 Extra-axonal restricted compartment diffusivity

The extra-axonal restricted compartment includes the freewater and neurites such as microglia.
The difference in extra-axonal diffusivity is represented in Fig.4.31. It was not clear visually which regions present a decrease and which present an increase.

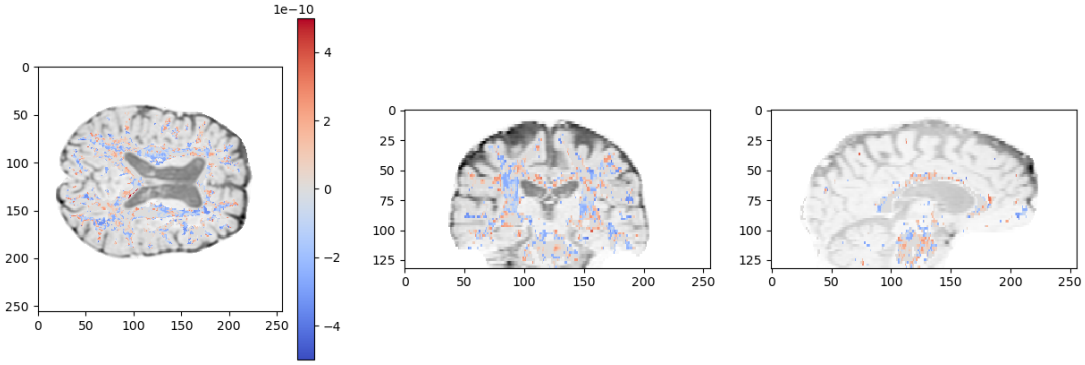

Fig 4.31: *Difference in extra-axonal diffusivity values in white matter before and after abstinence. Axial view (Left), coronal view (Middle) and sagittal view (Right).*

In Fig.4.32 is displayed the percentage change in extra-axonal diffusivity and the fraction attributed to the extra-axonal compartment. The two metrics seemed to be correlated.

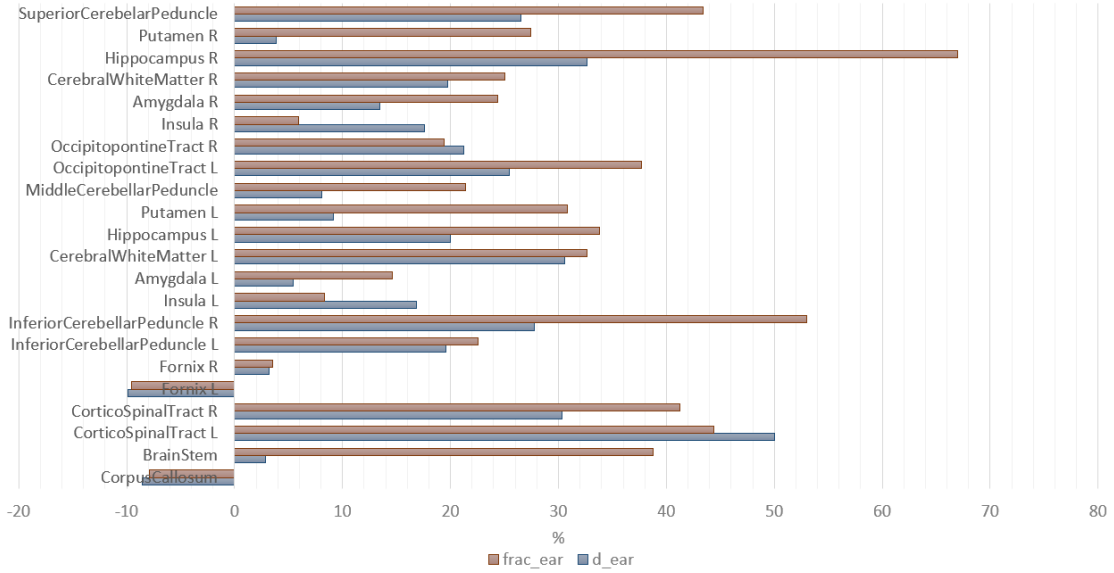

Fig 4.32: *Percentage change of extra-axonal diffusivity (d_ear) and fraction attributed to the extra-axonal compartment (frac_ear) values between before and after abstinence.*

4.4.2 Fractions of each compartment

Similarly to the DIAMOND model, the fractions of each compartment were also computed with the microstructure fingerprinting model. The difference in the fractions attributed to each compartment is represented in Fig.4.33. The evolution of the fractions of the three compartments seemed to differ between the microstructure fingerprinting model (Fig.4.33) and DIAMOND model (Fig.4.26).

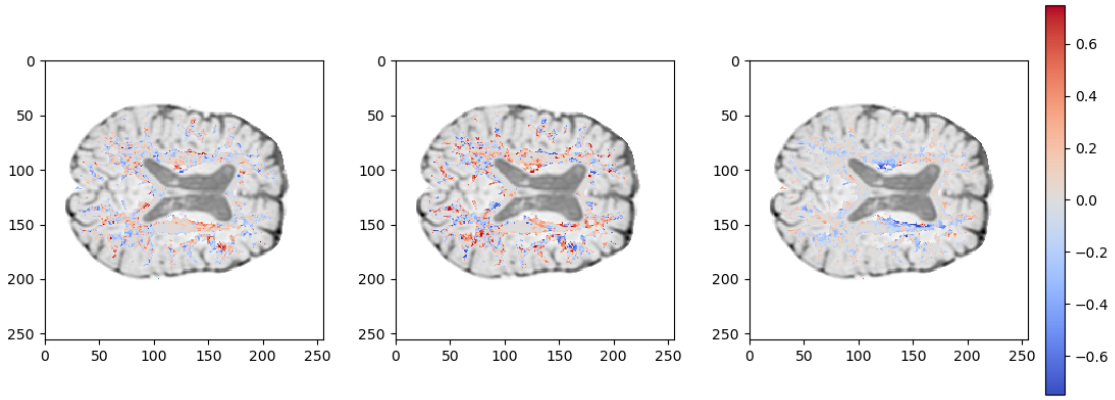

Fig 4.33: *Difference in fraction attributed to each compartment in white matter before and after abstinence. Fraction of the first fiber population (Left), second fiber population (Middle) and extra-axonal compartment (Right).*

In Fig.4.34 is displayed the percentage change in the fractions attributed to the two fiber population compartments.

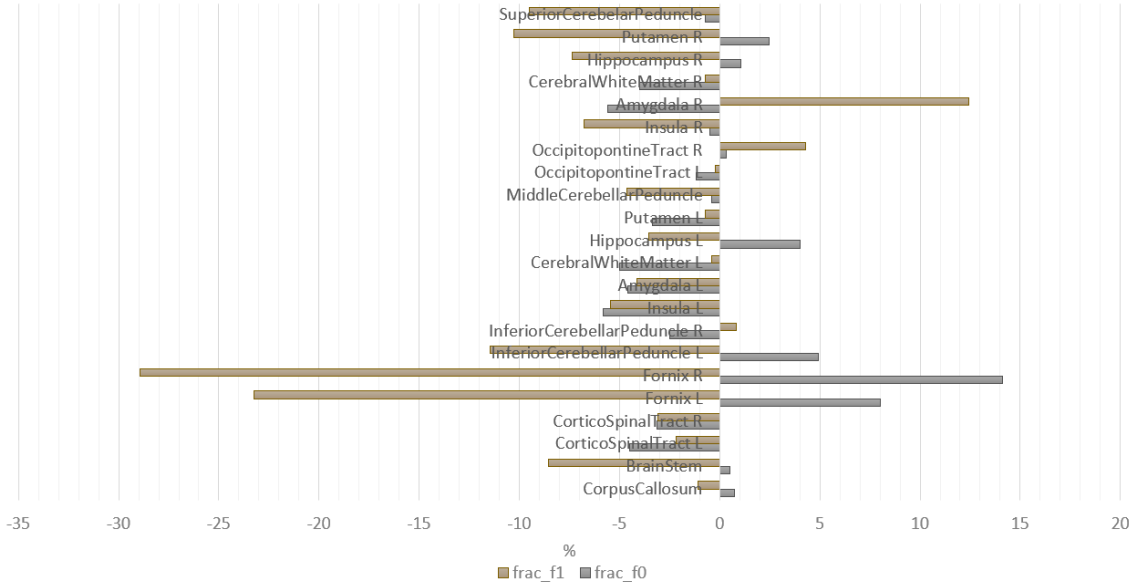

Fig 4.34: *Percentage change of the fraction attributed to the first fiber population (frac_f0) and fraction attributed to the second fiber population (frac_f1) values between before and after abstinence.*

4.4.3 Fiber fascicle volume fractions

The fiber volume fraction of a fiber fascicle represents the water fraction inside of the cylinders (modeling the axons) within a fascicle.
The difference in the total fiber volume fraction is represented in Fig.4.35. The figures for the fiber volume fraction of the first and second fiber population individually are available in Appendix D.2 Fig.D.6 and Fig.D.7, respectively. The volume in the fibers seemed to increase after abstinence throughout the whole volume.

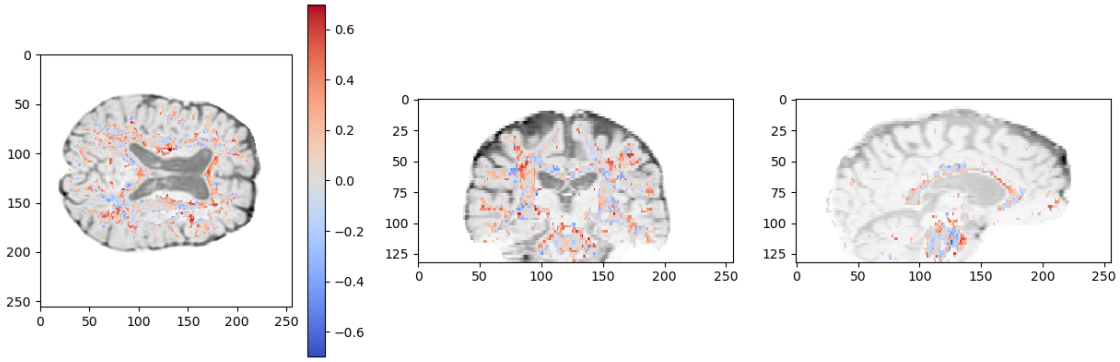

Fig 4.35: *Difference in total fiber volume fraction in white matter before and after abstinence. Axial view (Left), coronal view (Middle) and sagittal view (Right).*

This increase also stood out in the percentage change analysis (Fig.4.36), where most regions displayed an increase, especially in the insula, amygdala, putamen and CC.

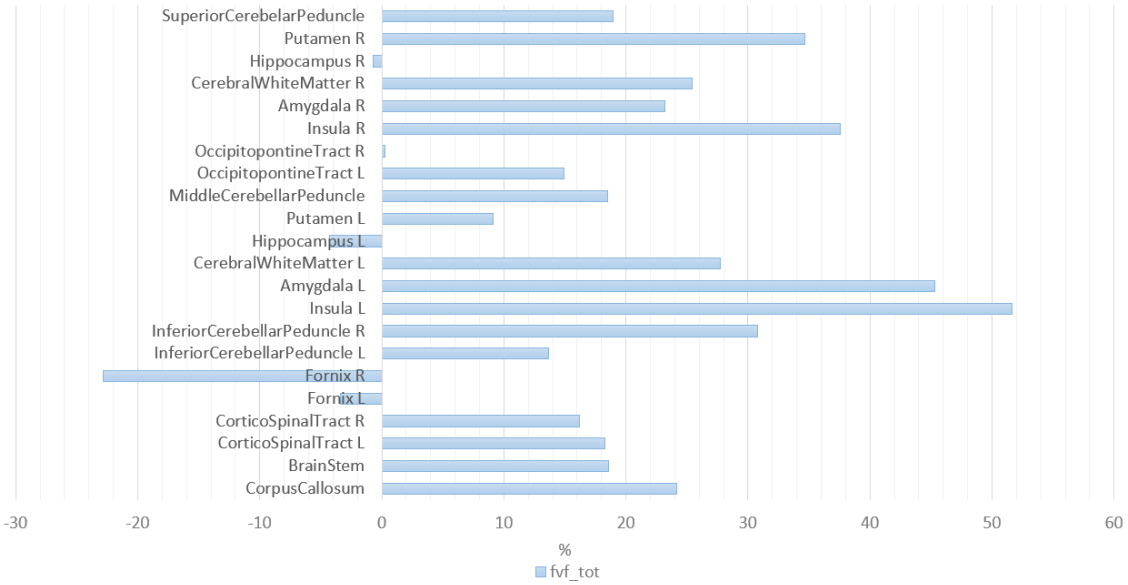

Fig 4.36: *Percentage change of the total fiber volume fraction attributed to both fiber populations (fvf_tot) values between before and after abstinence.*

4.4.4 Axonal radii

The change in radius of the two fiber populations are represented in Fig.4.37. Due to the noise and high variation, it was not clear which regions presented an increase or decrease of radius.

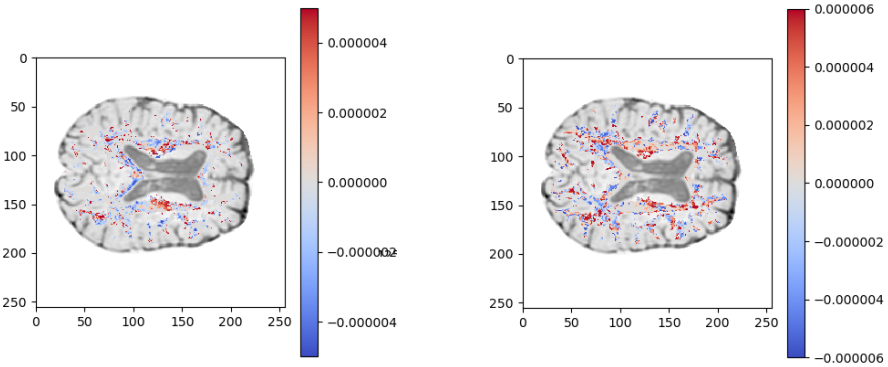

Fig 4.37: *Difference in axonal radius attributed to both fiber populations in white matter before and after abstinence. First fiber population (Left) and second fiber population (Right).*

As displayed in Fig.4.38, the main change was a decrease of the radius of the first fiber population, especially in the CC, brain stem and fornix.

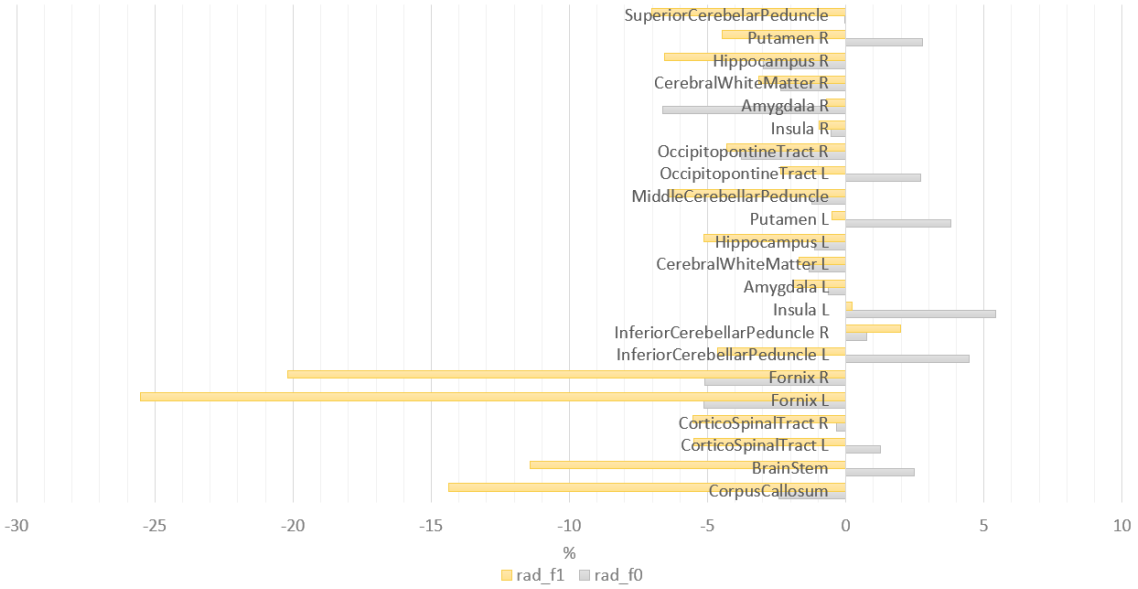

Fig 4.38: *Percentage change of the radius of both fiber populations (fiber pop. 1 [rad_f0] and fiber pop. 2 [rad_f1]) values between before and after abstinence.*

However, caution has to be applied when interpreting those results, as there was a large variation (as seen in Fig.4.37). Indeed, when plotting the means of the radius per region as well as their respective standard deviations (see Fig.4.39), it was noticed that the means were very similar across the regions studied and that the standard deviations were rather large. This led us to not consider the radius as a relevant metric for interpretation as the changes observed were most likely due to noise.
When this last graph (Fig.4.39) was compared to the graph of the means and standard deviations of the total fiber volume fraction attributed to both fiber populations (see Fig.4.40), it was noticed that the variation of the maximum value between regions was larger in the total fiber volume fraction attributed to both fiber populations

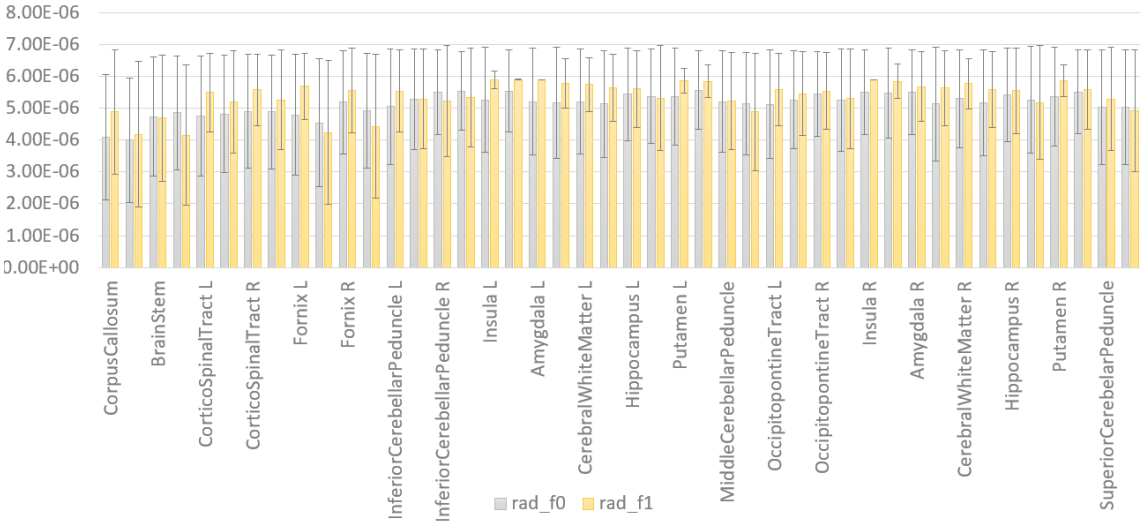

Fig 4.39: *Means and standard deviations of the radii of the two fiber populations (rad_f0 and rad_f1) across regions, before (T0) and after (T1) abstinence.*

(fvf_tot). Which meant that the fvf_tot metric was more likely to be dependent on the microstructure of the regions and that fvf_tot was probably more relevant than the radius computed with microstucture fingerprinting.

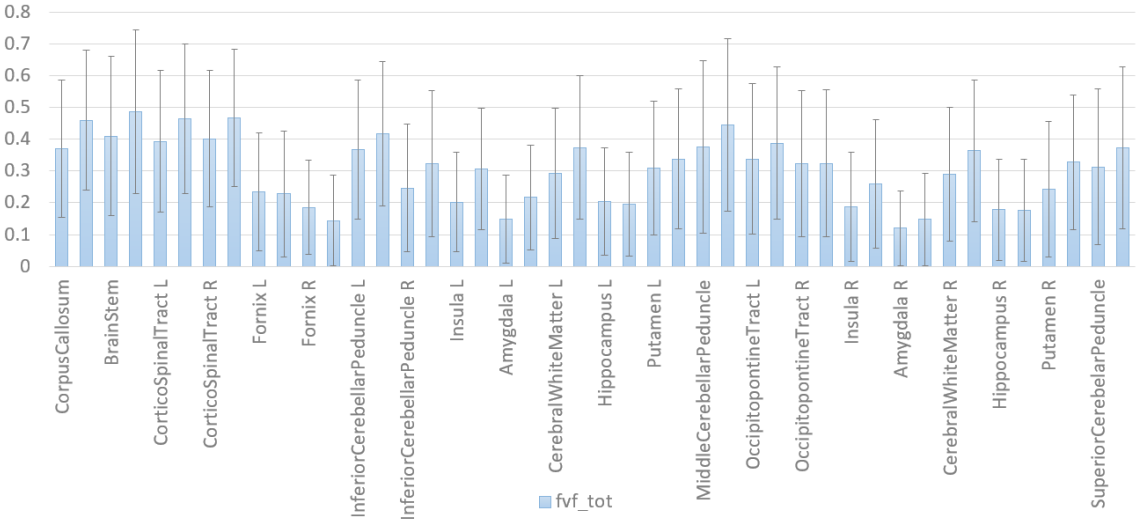

Fig 4.40: *Means and standard deviations of the total fiber volume fraction attributed to both fiber populations (fvf_tot), before (T0) and after (T1) abstinence.*

Chapter 5

Discussion

Two main effects are thought to be at play during abstinence: the inflammation process (with a link to depression) and the osmotic effects. The inflammation is thought to be present in areas such as the insula and the anterior cingulate cortex. The osmotic effects are mostly visible during early abstinence [60].

5.1 Most impacted regions

From the previous section, we can extract the regions that were significantly impacted (with more than 10% of percentage change) by the withdrawal period through the scope of different metrics. The impact of alcohol abstinence on these regions is discussed in the sections below, as well as the general impact on all white matter regions.

5.1.1 Corpus Callosum

The corpus callosum (CC) is one of the brain regions in which many metrics were significantly impacted after the two-week abstinence period. The FA and AD (from the DKI model) increased, meaning that the integrity of the axons in the CC might have improved. The RD decreased greatly, which could be due to a loss of inflammation or a change in the myelin sheaths.
From NODDI, the intracellular volume fraction metric (representing the fraction of the space bounded by the membranes of neurites) increased slightly, while the fraction of free water volume decreased. The changes in these two metrics could be the sign of an increased neurite density or an increase in myelination [61]. The orientation dispersion index also decreased.
Similar results were found with DIAMOND, as the fraction attributed to the main fiber population increased, while the fraction attributed to the isotropic volume decreased. The heterogeneity of the main fiber population also decreased, whereas the heterogeneity of the second fiber population increased. It could be hypothesized that the increased heterogeineity of the second fiber population corresponds to the change of shape of the microglia after deactivation (see Section 2.1 for more information about microglial activation).

From the microstructure fingerprinting model, an increase of the total fiber volume fraction, representing the water fraction inside of the axons, was observed in the CC. The radius attributed to the second fiber population decreased.

The corpus callosum (see Fig.5.1-Left) connects the two hemisphere of the brain. Changes in the microstructure of the CC can represent an altered connectivity between the right and left side of the brain. A decrease in connectivity has been linked to a "behavioral" depression. This depression increases during early abstinence and then decreases [60].

Furthermore, a region that was not isolated in this report but which could correspond to a region of interest where changes were detected visually in Section 4 is the forceps major. The forceps major is linked to the CC and the visual area. Changes in the microstructure of the forceps major could be linked to hallucinations seen by highly alcoholic patients undergoing a strict abstinence period. This pathology is named *delirium tremens* and one of the effects is hallucinations involving animals (also known as *zoopsies* in french) [60].

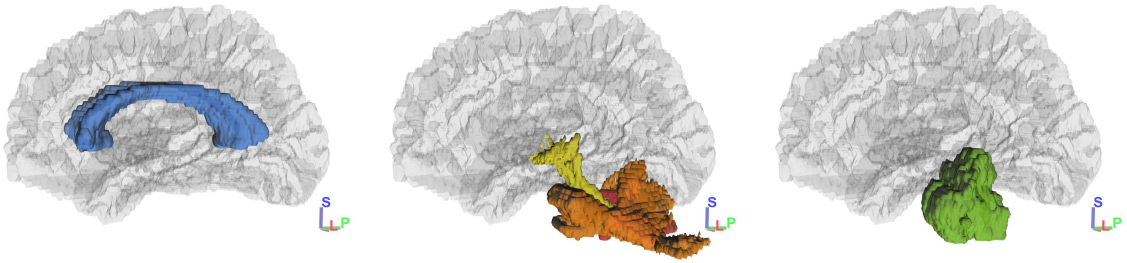

Fig 5.1: *Representation of the : corpus callosum (in blue) [Left]; cerebellar peduncle (superior in yellow, middle in orange and inferior in red) [Middle]; brainstem (in green) [Right].*

5.1.2 Cerebellar peduncle

The three parts of the cerebellar peduncle (inferior, middle and superior, see Fig.5.1-Middle) all presented an increase in FA and AD. This increase could be a sign of improved axonal integrity. In the middle cerebellar peduncle, the RD decreased while the AK decreased. This decrease in AK may be due to water being less confined by multiple structures in the axial orientation after abstinence.
The fraction of free water volume decreased in all three sections, but more so in the left side of the inferior peduncle than the right side. The orientation dispersion index also decreased in a similar fashion, although on a smaller scale.
Using the DIAMOND model, the significant changes were an increase of the fraction attributed to the first fiber population (linked mainly with a small decrease in the fraction of the isotropic compartment) and its homogeneity, and a decrease in homogeneity of the second fiber population.

With the microstructure fingerprinting model, the significant changes were an increase in the fraction attributed to the extra-axonal restricted compartment and an increase in its diffusivity. The total fiber volume fraction, representing the water fraction inside of the axons, also increased in all three sub-regions.

The cerebellar peduncles contain tracts carrying proprioceptive sensory input to the cerebellum, this input is integrated with motor vestibular functions such as balance and posture maintenance in the cerebellum, and then sent to the midbrain. Changes in the cerebellar tracts or the cerebellum are linked with addiction comportment [60].

5.1.3 Brain stem

The brain stem (displayed in Fig.5.1-Right) seemed to be less impacted by the withdrawal period than the two regions above. The observed changes using DTI and DKI are not as significant as the two previous regions. Using NODDI, a decrease of the free water compartment fraction was observed. With DIAMOND, an increase of the fraction attributed to the first fiber population and its homogeneity was observed. Whereas, the homogeneity of the second fiber population decreased. The microstructure fingerprinting model displayed an increase of the fraction of the extra-axonal restricted compartment and of the total fiber volume fraction.

The brain stem in a key element in a multitude of functions from regulating cardiac and respiratory function to the regulation of the central nervous system and the sleep cycle. It is also pathway of motor and sensory inputs between the rest of the brain and the body. An impact on the brain stem (composed of the midbrain, pons and medulla) and the cerebellum can be linked to behaviors presenting cravings [60].

5.1.4 Amygdala

The amygdala (shown in Fig.5.2-Left) was also one the most impacted regions with an increase of FA in the left hemisphere.
With the NODDI model, the fraction attributed to the intracellular volume increased, suggesting an increase of neurite density. The fraction of the free water volume also increased. Using DIAMOND, the isotropic diffusivity increased. The fraction attributed to the first fiber population increased greatly. Once again, the homogeneity of the first fiber population increased while the homogeneity of the second decreased. The microstructure fingerprinting model displayed an increase of the fraction of the extra-axonal restricted compartment and of the total fiber volume fraction.

The primary role of the amygdala is the processing of memory, decision-making and emotional responses. These emotional responses include fear, anxiety, and aggression. The amygdalae are considered part of the limbic system, which was found to be impacted by alcohol consumption (see Section 2).

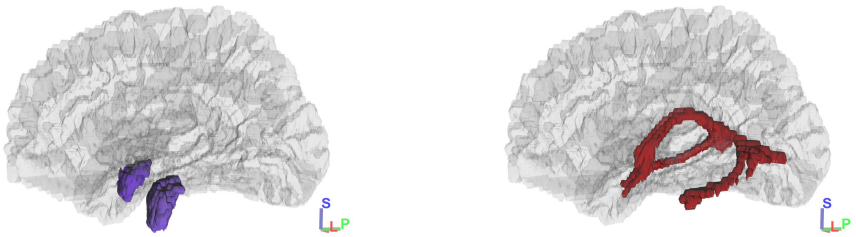

Fig 5.2: *Representation of the : amygdala (in purple) [Left]; fornix (in red) [Right].*

5.1.5 Fornix

The left part of the fornix displayed an increase in FA and AD, suggesting an increased axonal integrity. The fraction and homogeneity of the first fiber population increased, while the fraction and homogeneity of the second decreased. Both of these changes were larger in the left side of the fornix. The difference in fractions was also found using the microstructure fingerprinting model: the first fiber population fraction increased and the second decreased. The total fiber volume fraction increased in the left fornix. The radius evolution after abstinence displayed the biggest percentage change of all regions in the fornix, with a large decrease in the estimated radius of the second population.

The fornix is also part of the limbic system and is considered to be the main output tract of the hippocampus. Damage to the fornix has been linked to memory loss, more specifically *recall memory*.

5.1.6 Cerebral white matter

Overall, the results were different from the evolution of the metrics observed by De Santis & al. where a decrease of FA and an increase of RD were found through most white matter tracts during early abstinence (2-3 weeks) [30].
In this report, the cerebral white matter (which includes the regions discussed above) displayed an increase of the mean fraction attributed to the free water compartment, especially in regions such as the insula, amygdala and hippocampus.
According to the results of the DIAMOND model, the volume fraction attributed to the first fiber population increased, as well as its homogeneity. The homogeneity of the second fiber population decreased.
With the microstructure fingerprinting model, an increase of the diffusivity and volume fraction of the extra-axonal restricted compartment was found (especially in the corticospinal tract, hippocampus and occitopontine tract). The total fiber volume fraction per voxel also increased, especially in the insula. An increase of the total fiber volume fraction, while the fascicle's volume fractions remains more or less constant, could be an indicator of axonal recovery (as there are more axons per square micrometer).

Regions with an increased intracellular volume fraction (NODDI) or an increased

total fiber volume fraction (microstructure fingerprinting) after abstinence could be linked to osmotic changes observed in the brain. Ethanol is known to get into the extra-cellular space, which in turn will decrease the intracellular water volume by osmosis [60]. The abstinence process would then restore the osmosis equilibrium, leading to an increased intracellular volume.

A simplified table is available in Fig.5.3 with the percentage change of all regions analyzed with most of the metrics. The metrics that are not included in this table either displayed no significant percentage change across regions (such as MK), offered similar information (such as KFA with respect to FA) or displayed artefacts in the visual analysis (such as TORT from WMTI and RK from DKI).

	DKI				NODDI			DIAMOND						Microstructure fingerprinting				
	FA	AD	RD	AK	ficvf	fiso	odi	fd	frac_1	kap_1	frac_2	kap_2	frac_iso	d_ear	frac_ear	frac_f0	frac_f1	fvf_tot
Acoustic Radiation	13.2	16.0	-13.0	-10.4	2.8	4.1	-19.0	4.4	11.9	10.8	-10.3	-51.1	-0.2	-3.8	1.4	2.6	-0.7	3.6
Amygdala L	12.9	1.3	-6.4	-0.4	16.6	42.4	-5.5	-13.3	27.5	39.2	-13.2	-52.1	-7.1	5.4	14.6	-4.6	-4.1	45.3
Amygdala R	6.9	-1.5	-6.1	2.5	16.5	37.3	-0.4	-20.9	17.8	16.6	3.0	-37.5	-8.2	13.5	24.4	-5.6	12.4	23.2
Anterior Commissure	11.0	10.8	-3.4	-6.8	0.2	3.8	-12.6	-4.6	5.6	3.0	0.0	-42.7	-3.9	24.7	24.6	-0.7	-0.6	21.0
BrainStem	7.5	3.0	-9.8	-0.4	2.0	-13.7	-7.6	-5.1	12.7	10.3	0.7	-58.6	-9.5	2.9	38.8	0.5	-8.6	18.6
Cerebral White Matter L	4.5	7.9	7.1	-4.0	7.7	20.9	1.2	-7.9	15.6	5.2	6.1	-47.2	-9.2	30.6	32.6	-5.0	-0.4	27.8
Cerebral White Matter R	6.4	4.8	0.5	-1.6	9.5	12.1	0.4	-6.0	14.5	23.8	-0.4	-53.3	-7.4	19.7	25.0	-4.0	-0.7	25.4
Corpus Callosum	11.3	12.0	-35.3	-6.1	9.9	-13.9	-22.7	6.2	12.5	29.5	-4.4	-33.0	-11.2	-8.6	-7.9	0.7	-1.1	24.2
Cortico Spinal Tract L	-2.1	5.3	14.8	-1.7	2.2	10.8	6.9	-4.6	4.7	17.3	6.1	-43.7	-8.1	50.0	44.4	-4.5	-2.2	18.3
Cortico Spinal Tract R	0.8	2.9	3.9	0.2	4.9	6.7	6.5	-4.5	3.2	34.6	-1.8	-48.3	-6.4	30.3	41.3	-3.2	-3.1	16.2
Fornix H	10.5	0.6	-9.3	1.8	6.2	0.2	-4.9	3.4	22.7	19.0	-18.9	-74.6	-3.4	-3.8	-0.9	0.3	-18.0	5.2
Fornix L	16.1	13.5	-1.1	-9.1	-1.0	-4.8	-8.6	6.9	29.4	22.1	-23.4	-74.8	-3.6	-9.9	-9.5	8.0	-23.3	-3.4
Fornix R	1.4	6.1	3.1	-3.5	-2.3	6.0	0.2	-0.3	10.8	19.7	-15.0	-26.2	-1.1	3.2	3.5	14.1	-29.0	-22.8
Hippocampus L	2.4	9.3	4.5	-6.2	1.6	35.5	-2.9	-20.2	12.0	0.4	-8.7	-50.7	-0.4	20.0	33.8	4.0	-3.5	-4.3
Hippocampus R	-3.2	4.7	4.2	-2.7	-0.9	24.8	3.4	-28.1	6.9	20.4	-11.1	-56.4	0.4	32.6	66.9	1.1	-7.4	-0.7
InferiorCerebellarPeduncle L	12.0	19.1	-5.0	-13.4	-3.3	-20.7	-10.5	-5.8	12.6	31.4	-3.8	-60.9	-9.2	19.6	22.5	4.9	-11.5	13.7
InferiorCerebellarPeduncle R	5.4	17.1	3.8	-8.9	-4.5	-3.0	-3.1	-5.0	15.3	39.5	-6.3	-60.1	-5.5	27.8	53.0	-2.5	0.8	30.8
Insula L	11.8	6.4	2.4	-5.1	12.8	72.0	-7.8	-6.8	2.1	-18.9	8.2	-10.1	-4.7	16.9	8.3	-5.8	-5.4	51.7
Insula R	6.5	3.7	1.5	-1.9	11.1	65.7	-1.4	-3.6	6.4	27.9	-7.1	-41.0	0.0	17.6	5.9	-0.5	-6.8	37.6
Middle Cerebellar Peduncle	13.0	12.7	-11.8	-6.4	3.4	-18.0	-12.2	-1.2	13.6	10.1	-3.7	-60.2	-10.9	8.1	21.4	-0.4	-4.6	18.5
Occipitopontine Tract L	9.3	11.0	-6.8	-7.4	1.2	-0.5	-12.6	-0.2	4.9	1.3	3.8	-49.8	-6.1	25.4	37.7	-1.2	-0.2	15.0
Occipitopontine Tract R	6.7	10.4	-1.0	-6.8	1.1	3.4	-9.0	0.1	10.8	21.1	-6.0	-51.9	-3.7	21.2	19.4	0.3	4.3	0.3
Putamen L	1.0	1.5	-1.7	0.7	5.7	-2.6	5.9	-22.6	12.4	18.3	-3.5	-25.2	-4.1	9.2	30.9	-3.4	-0.7	9.1
Putamen R	6.9	3.0	-4.3	0.6	4.3	-13.0	1.3	-13.0	0.6	15.8	-6.4	-26.1	2.7	3.9	27.4	2.5	-10.3	34.6
Superior Cerebelar Peduncle	8.6	15.1	-2.9	-7.5	-1.3	-10.1	-8.7	-7.9	12.3	12.6	-1.5	-51.4	-8.6	26.5	43.4	-0.7	-9.5	18.9

Fig 5.3: *Summarized table of the percentage changes (in %) observed before and after abstinence. Blue represents a decrease and orange an increase after withdrawal. See Section 3.2 for more information on the metrics of each model.*

Another aspect that was not studied in this report but which could be of interest is a volumetric analysis of the white and grey matter. A volumetric inversion is often observed in AUD patient during abstinence. The volume increases in the grey matter and decreases in the white matter after abstinence. This is thought to be due to the increased proportion of cells in the grey matter. This increase in proportion leads to more important osmotic effects. The volume increases at the end of abstinence [60]. In the ventricular system, the volume increases in the beginning of the abstinence period and decreases towards the end [60].

5.2 Most impacted metrics

In Table 5.3 are also displayed the metrics from the different models which provided useful insight on the evolution of microstructure parameters during abstinence. As explained in Section 4, some metrics were not included due to either a lack of changes in values after abstinence (such as MD and MKT), visual artefacts in the metric maps obtained (such as AWF and RK) or redundancy with other metrics (such as KFA and MSD).

Some metrics such as the fraction of the first fiber population increased in all analyzed regions (`frac_1` in the DIAMOND model) while others decreased in every region, such as the homogeneity of the second fiber population (`kap_2`, also in the DIAMOND model). Other metrics such as `fiso` increased in some regions and decreased in others.

In some regions, such as the hippocampus and the putamen, the single-compartment models (DTI, DKI, MSDKI) did not find any significant percentage changes before and after abstinence, while the multi-compartments models (NODDI, DIAMOND and microstructure fingerprinting) displayed some significant changes. The mutli-compartments models thus seem to have the ability to detect microstructures variations that are not highlighted by the single-compartment models. Looking at the fornix, this time it is the NODDI model that did not display significant changes while the other models did find some variations in their metrics.

However, there are inconsistencies between models, while both DIAMOND and microstructure fingerprinting models have a compartment linked to extra-axonal isotropic diffusion, the evolution of the diffusivity of the extra-axonal compartment after abstinence increases in the microstructure fingerprinting model and decreases in the DIAMOND model (see Fig.5.4).

There is no clear evidence suggesting that one of the models used during this thesis is better in every aspect than the others. The models seem to be complementary and a clear selection of a few distinct models is probably a wiser choice than to base all analyses on a single model. On the opposite hand, using many similar models (such as DTI and DKI) would be inefficient time-wise as the output metrics are similar and while the values found for each metric are not exactly the same, the evolution of these values before and after abstinence seemed to go in a similar direction in this study.
While the selection of models may change based on the study and personnal preference, the combination of DKI, NODDI, DIAMOND and microstructure fingerprinting models was found to be effective at quantifying the microstructrural changes in an AUD patient in this study.

The exact biological interpretation of the metrics used in this thesis is still being debated. As mentioned previously, metrics such as FA can vary due to a multitude of microstructural changes, ranging from the amount of crossing fibers to axonal integrity, as well as the density of fiber or the amount of myelination [61].

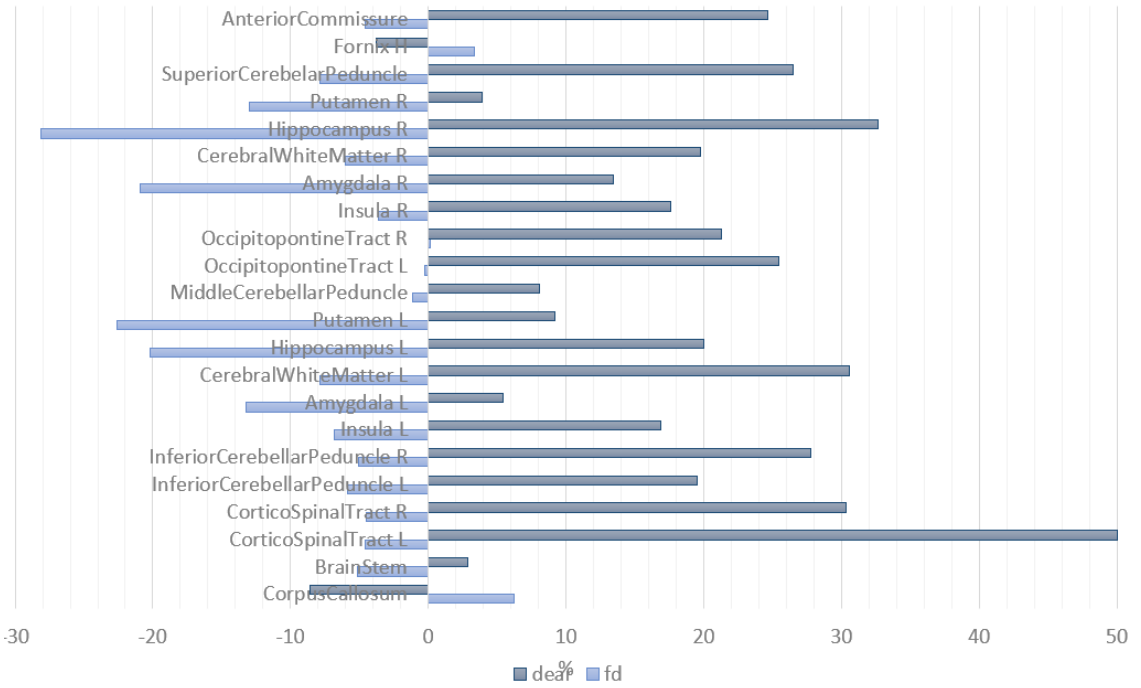

Fig 5.4: *Percentage change of the diffusivity of the extra-axonal compartment in the DIAMOND (fd) and microstructure fingerprinting model (dear) after abstinence.*

Furthermore, more "advanced" metrics from the compartment-based microstructural models (NODDI, DIAMOND and microstructure fingerprinting) also present some grey areas when interpreting the observed changes. An example are the changes linked to the microglia (see Section 2.1 for more information about the expected microglial changes), studies on microglial density have found that changes in density impacted several compartments, such as the intra-cellular and extra-cellular compartments of NODDI [61]. Another example is in the microstructure fingerprinting model, where the impact of myelin changes on the radius metric is unknown. The impact that cells such as microglia and astrocytes have on the diffusion signal is thus still up for discussion. Further research is thus needed to assign a clear interpretation of these metrics.

5.3 Limitations

The analysis presented in this report is not exhaustive with respect to the microstructural impact of alcohol abstinence and presents some limitations.

First of all, the regions studied were selected based on their availability in online automated atlases and their relevance in the literature review (see Section 2). Further research should include a broader range of regions.
Some metrics were also not used due to visual artefacts, including these metrics could provide additional information.

Another limitation was the number of patients studied, a single patient going through withdrawal did not provide sufficient data for a statistical analysis and the changes observed in this patient could be outliers in a larger population. The length of the abstinence period could also be increased, with a higher number of scans throughout the abstinence period.

Furthermore, some metrics presented large standard variations within a region. This could be due to the use of automated atlases, signal errors or non-optimal parameters used throughout the data processing pipeline. Reducing this variation would increase the confidence that a metric correctly translates the microstructural changes in a region.

Finally, as mentioned in Section 5.2, the interpretation of the metrics still has to be refined before the biological impact of alcohol consumption habits on the the brain microstructure can be confidently assessed.

5.4 Going further

As mentioned in the previous section, increasing the number of scans, patients, metric used and brain regions would allow the use of relevant statistics. A commonly used tool, TBBS (see Appendix B.3 for more information), could then be used to extract the impact of each metric on the major white matter tracts.
The metrics could also be ranked to see which are most correlated with the microstructural changes occurring during alcohol withdrawal.

A volume reduction analysis could also be of interest to observe the osmotic changes between the white and grey matter. The grey matter was not studied in this report, but it could provide some additional information about the microstructural changes in the cortex, although some models such as DIAMOND might not give accurate results in the grey matter.

It would also be of interest to cross the results obtained during this thesis with results from other fields in order to obtain more information about the microstructural changes at play during alcohol abstinence. Streamlining the process of extracting the variables and measures representing the brain microstructure from the raw data and providing clear displays of the information would be interesting for the medical professionals. The data processing pipeline should also include denoising before motion correction.

Conclusion

Quantifying the microstructural changes of the brain due to neuropathologies, such as alcohol disorder, via diffusion MRI is an ongoing challenge. The developments of multi-compartments models in the past few years have opened the way to a more precise characterization of these microstructural changes.

This thesis presents a literature review on the impact of alcohol consumption on diffusion-based metrics, obtained from different microstructural models. A data processing pipeline is described to get from raw diffusion data acquired in a real-life setting to a visual and region-based analysis with free and available software.
Advanced multi-compartments models such as NODDI, DIAMOND and microstructure fingerprinting have also been applied to this case-study of a patient with alcohol use disorder undergoing abstinence from alcohol consumption.
The DIAMOND model was also used to characterize the microstructural changes in the corticospinal tract in children with cerebral palsy.

The goal of this thesis was to identify which metrics would best describe the microstructural changes observed during abstinence in different brain regions, to determine which brain regions were the most impacted and to compare the different microstructural changes that can be observed by each model.
The most impacted regions of an AUD patient before and after alcohol abstinence were found to be : the corpus callosum, cerebellar peduncles and structures of the limbic system (such as the fornix and amygdala). These regions are associated with specific brain functions such as memory, emotional responses, cravings, addiction and behavioral depression.
Comparing the models and the observed percentage changes of their metrics allowed the selection of models which could cover a broad range of microstructural changes. The selected models were DKI, NODDI, DIAMOND and microstructure fingerprinting. Within those models, some metrics were deemed more useful than others when quantifying the microstructural changes during early alcohol abstinence due to some metrics presenting redundant information, visual artefacts or high standard deviations.

The metrics used for the region-based analysis also suffer from other limitations such as the fact that the exact interpretation of the biological changes they represent is still being debated. Furthermore, a statistical analysis across a larger population of AUD patients is necessary to assess with certitude the impact of the metrics in every region. Increasing the number of scans along the abstinence period will also improve our understanding of the dynamic microstructural changes at play during alcohol withdrawal.
Nevertheless, streamlining the data processing pipeline presented in this report could provide medical professionals with a useful tool to apply region-based analyses with multiple models to a larger patient population. Comparing the results obtained in other medical fields to the microstructural changes observed via diffusion MRI could also further improve our understanding of alcohol use disorder.

Bibliography

[1] Leclercq S., de Timary P., Delzenne N. M., and Stärkel P. The link between inflammation, bugs, the intestine and the brain in alcohol dependence. *Translational Psychiatry*, 7(2), 2017. doi:10.1038/tp.2017.15.

[2] Kasler B. Comprendre l'irm, manuel d'auto-apprentissage, 2011. 7th edition, 390 pages.

[3] e-mri. `https://www.imaios.com/en/e-Courses/e-MRI/NMR/Net-magnetization`.

[4] Questions and answers in MRI. Why is t1 longer than t2? `https://mri-q.com/why-is-t1--t2.html`. [Accessed 21/5/2020].

[5] Wikipedia. Bloch equations. `https://en.wikipedia.org/wiki/Bloch_equations`. [Accessed 21/5/2020].

[6] Radiopaedia. Mri artifacts. `https://radiopaedia.org/articles/mri-artifacts-1?lang=us`. [Accessed 2/6/2020].

[7] T.A.G.M Huisman. Diffusion-weighted and diffusion tensor imaging of the brain. *Cancer Imaging*, 10, 2010. doi:10.1102/1470-7330.2010.9023.

[8] Alain Niyigaba Ishimwe. *The influence of spherical pores within the white matter on Diffusion-Weighted MRI signals : a numerical study using Monte-Carlo simulations. Dissertation presented by Alain NIYIGABA ISHIMWE for obtaining the Master's degree in Electrical Engineering.* PhD thesis, Ecole polytechnique de Louvain, Université catholique de Louvain, 08 2017. doi:10.13140/RG.2.2.25945.42087.

[9] R. Gruetter. Fundamentals of biomedical imaging. Course : PHYS-438, EPFL, Lausanne, April 2019.

[10] G. Rensonnet. In vivo diffusion magnetic resonance imaging of the white matter microstructure from dictionaries generated by monte carlo simulations : development and validation, 2019. Thesis no.8497.

[11] Lauren O'Donnell and Carl-Fredrik Westin. An introduction to diffusion tensor image analysis. *Neurosurgery clinics of North America*, 22:185–96, viii, 04 2011. doi:10.1016/j.nec.2010.12.004.

[12] W. Van Hecke, L. Emsell, and S. Sunaert. Diffusion tensor imaging. Ed. Springer, ISBN 978-1-4939-3117-0, 2016.

[13] Tucana. Tensor field in a diffusion mri image. `https://en.wikipedia.org/wiki/File:DiffusionMRI_glyphs.png`.

[14] J. H. Jensen, J. A. Helpern, A. Ramani, H. Lu, and K. Kaczynski. Diffusional kurtosis imaging: The quantification of non-gaussian water diffusion by means of magnetic resonance imaging. *Magnetic Resonance in Medicine*, 53(6):1432–1440, 2005. doi:10.1002/mrm.20508.

[15] R. Neto Henriques. Advanced methods for diffusion mri data analysis and their application to the healthy ageing brain (doctoral thesis), 2018. doi:10.17863/CAM.29356.

[16] E. Fieremans, A. Benitez, J. H. Jensen, M. F. Falangola, A. Tabesh, R. L. Deardorff, and J. A. Helpern. Novel white matter tract integrity metrics sensitive to alzheimer disease progression. *American Journal of Neuroradiology*, 34(11):2105–2112, 2013. doi:10.3174/ajnr.a3553.

[17] H. Zhang, T. Schneider, C. A. Wheeler-Kingshott, and D. C. Alexander. Noddi: Practical in vivo neurite orientation dispersion and density imaging of the human brain. *NeuroImage*, 61(4):1000–1016, 2012. doi:10.1016/j.neuroimage.2012.03.072.

[18] Md. Hasnat. Unsupervised 3d image clustering and extension to joint color and depth segmentation., 2014.

[19] Yablonskiy DA, Bretthorst GL, and Ackerman JJ. Statistical model for diffusion attenuated mr signal. *Magnetic Resonance Med*, 50:664–669, 2003.

[20] David Tuch, Timothy Reese, Mette Wiegell, Nikos Makris, John Belliveau, and Van Wedeen. High angular resolution diffusion imaging reveals intravoxel white matter fiber heterogeneity. *Magnetic resonance in medicine : official journal of the Society of Magnetic Resonance in Medicine / Society of Magnetic Resonance in Medicine*, 48:577–82, 10 2002. 10.1002/mrm.10268.

[21] B. Scherrer, A. Schwartzman, M. Taquet, M. Sahin, S. Prabhu, and S.K. Warfield. Characterizing brain tissue by assessment of the distribution of anisotropic microstructual environments in diffusion-compartment imaging (diamond). *Magnetic Resonance in Imaging*, 76(3):963–77, 2015. `http://onlinelibrary.wiley.com/doi/10.1002/mrm.25912/abstract`.

[22] Gaëtan Rensonnet. Generation of a dictionary of dw-mri signals from arbitrary brain microstructure configurations (master thesis). *Universite catholique de Louvain*, 2015.

[23] Wikipedia. Alcoholism. `https://en.wikipedia.org/wiki/Alcoholism`, [Consulted on 02.12.2019].

[24] Sophie Leclercq, Patrice Cani, Audrey Neyrinck, Peter Stärkel, Francois Jamar, Moïra Mikolajczak, Nathalie Delzenne, and Philippe Timary. Role of intestinal permeability and inflammation in the biological and behavioral control of alcohol-dependent subjects. *Brain, behavior, and immunity*, 26:911–8, 04 2012. 10.1016/j.bbi.2012.04.001.

[25] Rawan Barakat and Zoran Redzic. The role of activated microglia and resident macrophages in the neurovascular unit during cerebral ischemia: Is the jury still out? *Medical principles and practice : international journal of the Kuwait University, Health Science Centre*, 25, 08 2015. doi:10.1159/000435858.

[26] Nicola Kalk, Qi Guo, D Owen, R Cherian, David Erritzoe, Ashley Gilmour, Andre Santos Ribeiro, J McGonigle, Adam Waldman, P Matthews, J Cavanagh, I McInnes, kk Dar, Roger Gunn, Eugenii Rabiner, and A Lingford-Hughes. Decreased hippocampal translocator protein (18kda) expression in alcohol dependence: A [11c]pbr28 pet study. *Translational Psychiatry*, 7:e996, 01 2017. 10.1038/tp.2016.264.

[27] Silvia De Santis, Patrick Bach, Laura Pérez-Cervera, Alejandro Cosa-Linan, Georg Weil, Sabine Vollstädt-Klein, Derik Hermann, Falk Kiefer, Peter Kirsch, Roberto Ciccocioppo, Wolfgang H. Sommer, and Santiago Canals. Microstructural White Matter Alterations in Men With Alcohol Use Disorder and Rats With Excessive Alcohol Consumption During Early Abstinence. *JAMA Psychiatry*, 76(7):749–758, 07 2019.

[28] GetBodySmart. Unmyelinated and myelinated axons. `https://www.getbodysmart.com/nervous-system/unmyelinated-myelinated-axons`, [Consulted on 02.12.2019].

[29] L. K. McEvoy, C. Fennema-Notestine, J. A. Elman, L. T. Eyler, C. E. Franz, D. J. Hagler, and W. S. Kremen. Alcohol intake and brain white matter in middle aged men: Microscopic and macroscopic differences. *NeuroImage: Clinical*, 18:390–398, 2018. doi:10.1016/j.nicl.2018.02.006.

[30] Silvia De Santis, Patrick Bach, Laura Perez-Cervera, Alejandro Cosa-Linan, Sabine Vollst adt-Klein Georg Weil, Derik Hermann, Falk Kiefer, Peter Kirsch, Wolfgang H. Sommer Roberto Ciccocioppo, , and Santiago Canals. Microstructural white matter alterations in men with alcohol use disorder and rats with excessive alcohol consumption during early abstinence. *JAMA Psychiatry*, 76(7):749–758, 2019. doi:10.1001/jamapsychiatry.2019.0318.

[31] L. M. Kong, J. Y. Zeng, W. B. Zheng, Z. W. Shen, and R. H. Wu. Effects of acute alcohol consumption on the human brain: Diffusional kurtosis imaging and arterial spin-labeling study. *American Journal of Neuroradiology*, 2019. doi:10.3174/ajnr.a5992.

[32] X. Chen, J. Zeng, Z.-W. Shen, L. Kong, and W. Zheng. Diffusion kurtosis imaging detects microstructural changes in the brain after acute alcohol intoxication in rats. *BioMed Research International*, pages 1–6, 2017. doi:10.1155/2017/4757025.

[33] L. M. Kong, W. B. Zheng, G. P. Lian, and H. D. Zhang. Acute effects of alcohol on the human brain: Diffusion tensor imaging study. *American Journal of Neuroradiology*, 33(5):928–934, 2012. doi:10.3174/ajnr.a2873.

[34] N. M. Zahr and A. Pfefferbaum. Alcohol's effects on the brain: Neuroimaging results in humans and animal models. *Alcohol Research: Current Reviews*, 38(2):1–24, 2017.

[35] N. M. Zahr. Structural and microstructral imaging of the brain in alcohol use disorders. *Alcohol and the Nervous System*, pages 275–290, 2014. doi:10.1016/b978-0-444-62619-6.00017-3.

[36] Wang Y, Li X, Zhang C, Wang H, Li Z, Zhu J, and Yu Y. Selective microstructural integrity impairment of the isthmus subregion of the corpus callosum in alcohol-dependent males. *BMC Psychiatry*, 19(1), 2019. doi: 10.1186/s12888-019-2079-6.

[37] I.-C. Liu, C.-H. Chiu, C.-J. Chen, L.-W. Kuo, Y.-C. Lo, and W.-Y. I. Tseng. The microstructural integrity of the corpus callosum and associated impulsivity in alcohol dependence: A tractography-based segmentation study using diffusion spectrum imaging. *Psychiatry Research: Neuroimaging*, 184(2):128–134, 2010. doi:10.1016/j.pscychresns.2010.07.002.

[38] O. Pasternak, S. Kelly, V. J. Sydnor, and M. E. Shenton. Advances in microstructural diffusion neuroimaging for psychiatric disorders. *NeuroImage*, 2018. doi:10.1016/j.neuroimage.2018.04.051.

[39] E. J. Chumin, G. G. Grecco, M. Dzemidzic, H. Cheng, P. Finn, O. Sporns, and K. K. Yoder. Alterations in white matter microstructure and connectivity in young adults with alcohol use disorder. *Alcoholism: Clinical and Experimental Research*, 2019. doi:10.1111/acer.14048.

[40] Elofson J, Gongvatana W, and Carey KB. Alcohol use and cerebral white matter compromise in adolescence. *Addict Behav*, 38(7):2295–2305, 2013. doi:10.1016/j.addbeh.2013.03.001.

[41] De Bellis MD, Van Voorhees E, Hooper SR, and et al. Diffusion tensor measures of the corpus callosum in adolescents with adolescent onset alcohol use disorders. *Alcohol Clin Exp Res*, 32(3):395–404, 2008. doi:10.1111/j.1530-0277.2007.00603.x.

[42] S. Bava, L. R. Frank, T. McQueeny, B. C. Schweinsburg, A. D. Schweinsburg, and S. F. Tapert. Altered white matter microstructure in adolescent substance users. *Psychiatry research*, 173(3):228–237, 2009. doi:10.1016/j.pscychresns.2009.04.005.

[43] S. F. Tapert, A. D. Schweinsburg, V. C. Barlett, S. A. Brown, L. R. Frank, G. G. Brown, and M. J Meloy. Blood oxygen level dependent response and spatial working memory in adolescents with alcohol use disorders. *Alcoholism, clinical and experimental research*, 28(10):1577–1586, 2004. doi:10.1097/01.alc.0000141812.81234.a6.

[44] Valerie Cardenas, David Greenstein, Jean-Paul Fouche, Helen Ferrett, Natalie Cuzen, Dan Stein, and George Fein. Not lesser but greater fractional anisotropy in adolescents with alcohol use disorders. *NeuroImage : clinical*, 2:804–809, 2013. doi:10.1016/j.nicl.2013.06.002.

[45] E. J. Chumin, J. Goñi, M. E. Halcomb, T. C. Durazzo, M. Dzemidzic, and K. K. Yoder. Differences in white matter microstructure and connectivity in nontreatment-seeking individuals with alcohol use disorder. *Alcoholism: Clinical and Experimental Research*, 42(5):889–896, 2018. doi:10.1111/acer.13629.

[46] J. Wang, Y. Fan, Y. Dong, M. Ma, Y. Ma, Y. Dong, and C. Cui. Alterations in brain structure and functional connectivity in alcohol dependent patients and possible association with impulsivity. *PLOS ONE*, 11(8):e0161956, 2016. doi:10.1371/journal.pone.0161956.

[47] A. Pfefferbaum, M. J. Rosenbloom, W. Chu, S. A. Sassoon, T. Rohlfing, K. M. Pohl, and E. V. Sullivan. White matter microstructural recovery with abstinence and decline with relapse in alcohol dependence interacts with normal ageing: a controlled longitudinal dti study. *The Lancet Psychiatry*, 1(3):202–212, 2014. doi:10.1016/s2215-0366(14)70301-3.

[48] A. Pfefferbaum, M. Rosenbloom, T. Rohlfing, and E. V. Sullivan. Degradation of association and projection white matter systems in alcoholism detected with quantitative fiber tracking. *Biological Psychiatry*, 65(8):680–690, 2009. doi:10.1016/j.biopsych.2008.10.039.

[49] L. S. Morris, N. G. Dowell, M. Cercignani, N. A. Harrison, and V. Voon. Binge drinking differentially affects cortical and subcortical microstructure. *Addiction Biology*, 23(1):403–411, 2017. doi:10.1111/adb.12493.

[50] C. B. Fortier, E. C. Leritz, D. H. Salat, E. Lindemer, A. L. Maksimovskiy, J. Shepel, and R. E. McGlinchey. Widespread effects of alcohol on white matter microstructure. *Alcoholism: Clinical and Experimental Research*, 38(12), 2014. doi:10.1111/acer.12568.

[51] K. S. Sawyer, N. Maleki, G. Papadimitriou, N. Makris, M. Oscar-Berman, and G. J. Harris. Cerebral white matter sex dimorphism in alcoholism: a diffusion tensor imaging study. *Neuropsychopharmacology*, 43(9):1876–1883, 2018. doi:10.1038/s41386-018-0089-6.

[52] Y. Zou, D. E. Murray, T. C. Durazzo, T. P. Schmidt, T. A. Murray, and D. J. Meyerhoff. White matter microstructural correlates of relapse in alcohol dependence. *Psychiatry Research: Neuroimaging*, 281:92–100, 2018. doi:10.1016/j.pscychresns.2018.09.004.

[53] Leemans A, Jeurissen B, Sijbers J, and Jones DK. Exploredti: a graphical toolbox for processing, analyzing, and visualizing diffusion mr data, 2009. In: 17th Annual Meeting of Intl Soc Mag Reson Med, p. 3537, Hawaii, USA.

[54] NatBrainLab. Tractography based atlas of human brain connections. https://www.natbrainlab.co.uk/atlas-maps. [Accessed 23/3/2020].

[55] B. Jeurissen, M. Descoteaux, S. Mori, and A. Leemans. Diffusion mri fiber tractography of the brain. *NMR in Biomedicine*, 2017. e3785. doi:10.1002/nbm.3785.

[56] J.-D. Tournier, F. Calamante, and A. Connelly. Robust determination of the fibre orientation distribution in diffusion mri: Non-negativity constrained super-resolved spherical deconvolution. *NeuroImage*, 35(4):1459–1472, 2007. doi:10.1016/j.neuroimage.2007.02.016.

[57] Garyfallidis E, Brett M, Amirbekian B, Rokem A, van der Walt S, Descoteaux M, Nimmo-Smith I, and Dipy Contributors. Dipy, a library for the analysis of diffusion mri data. https://dipy.org/tutorials/, 2014. [Accessed 13/4/2020].

[58] R. P. Cabeen, D. H. Laidlaw, , and A. W. Toga. Quantitative imaging toolkit: Software for interactive 3d visualization, data exploration, and computational analysis of neuroimaging datasets. *Proceedings of the International Society for Magnetic Resonance in Medicine (ISMRM)*, 2854, 2018.

[59] Benoit Scherrer. Misteri. http://www.benoitscherrer.com/MisterI/index.html.

[60] de Timary P. Interview with de timary p. [08/05/2020].

[61] S. Y. Yi, N. A. Stowe, B. R. Barnett, K. Dodd, and J.-P. J. Yu. Microglial density alters measures of axonal integrity and structural connectivity. *Biological Psychiatry: Cognitive Neuroscience and Neuroimaging*, 2020. doi:10.1016/j.bpsc.2020.04.008.

[62] Yannick Bleyenheuft, Laurence Dricot, Daniela Ebner-Karestinos, Julie Paradis, Geoffroy Saussez, Anne Renders, Anne De Volder, Rodrigo Araneda, Andrew M Gordon, and Kathleen M Friel. Motor skill training may restore impaired corticospinal tract fibers in children with cerebral palsy. *Neurorehabilitation and Neural Repair*, page 1545968320918841, 2020.

[63] Pawel J Winklewski, Agnieszka Sabisz, Patrycja Naumczyk, Krzysztof Jodzio, Edyta Szurowska, and Arkadiusz Szarmach. Understanding the physiopathology behind axial and radial diffusivity changes—what do we know? *Frontiers in neurology*, 9:92, 2018.

[64] Wikipedia. Imagerie par résonnance magnétique. https://fr.wikipedia.org/wiki/Imagerie_par_r%C3%A9sonance_magn%C3%A9tique_fonctionnelle.

[65] Digital imaging and communications in medicine. https://www.dicomstandard.org/.

[66] S. M. Smith, M. Jenkinson, H. Johansen-Berg, D. Rueckert, T. E. Nichols, C. E. Mackay, and T. E. J. Behrens. Tract-based spatial statistics: Voxelwise

analysis of multi-subject diffusion data. *NeuroImage*, 31(4):1487–1505, 2006. doi:10.1016/j.neuroimage.2006.02.024.

Appendix A

Application of the DIAMOND model on children with cerebral palsy

This appendix is an analysis of the corticospinal tract in children with cerebral palsy (CP) through the scope of the DIAMOND model. This section was written in collaboration with Ysaline Leman in the context of her thesis on "*Quantifying anomalies in children with bilateral lesions leading to cerebral palsy via diffusion Magnetic Resonance Imaging*".

A.1 Diamond metrics used in this appendix

Different maps are obtained with the DIAMOND model. In this Appendix, the following metrics are considered:

- Free Water Diffusivity (FD), corresponding to the diffusivity in the extra-axonal restricted part;
- Model selection (Mose) map, a map with the number of fiber populations in each voxel;
- The fraction of each population within each voxel (Frac(Pi), i=0 and i=1 for the two anisotropic compartments and i=2 for the isotropic compartment);
- Fractional Anisotropy (FA), Axial Diffusivity (AD) and Radial Diffusivity (RD) are the same metrics than in the DTI model. As each of them does not make sense for the third population (corresponding to the extra-axonal population), the FA per voxel, called weighted FA (wFA), is normalized on the two anisotropic populations by:

$$wFA = \frac{cFA(P0) \cdot Frac(P0) + cFA(P1) \cdot Frac(P1)}{Frac(P0) + Frac(P1)}$$

  cFA corresponds to the compartment FA. This formula is given for the wFA but similar calculations are done for the wAD and wRD.

- The heterogeneity of each population within each voxel (Hei(i)) . The heterogeneity metric Hei is linked to the concentration parameter κ (described in Section 1.3.2) by the formula :

$$Hei = \frac{2}{\pi} \arctan\left(\frac{1}{\kappa}\right)$$

A.2 Subject information

Two populations were scanned, 7 children with cerebral palsy (CP) and 4 control subjects. The characteristics of these children are presented in this section. It has to be noted that only 4 control subjects were taken into account in this work because 3 subjects with CP were rejected due to their scans being too noisy.

A.2.1 Subjects with cerebral palsy

The subjects with CP have lesions on both hemispheres. The information about the type of lesions and their most affected hand are given in Table A.1.
Early diagnostics of CP are difficult to make, by consequence, both diplegia and quadriplegia cases are considered in this work. The current diagnostic is reported in Table A.1 with WMI corresponding to diplegia and GMI to quadriplegia, but it could evolve with age.

Subject	Age [year]	Lesion Type	Most Affected Hand
1	3	WMI/PVL	RIGHT
2	2	WMI/PVL	LEFT
3	3	WMI/PVL	RIGHT
4	3	GMI	LEFT
5	4	GMI	LEFT
6	1	WMI/PVL	LEFT
7	4	GMI	RIGHT

Table A.1: *Information about the CP subjects: Age at time of MRI acquisition, lesion type (WMI=White mater injury, GMI=Gray mater injury and PVL= periventricular lesion) and the most affected hand.*

A.2.2 Control subjects

The age and handedness of the control subjects are described in Table A.2.

Subject	Age[year]	Handedness
8	9	RIGHT
9	9	RIGHT
10	10	RIGHT
11	8	RIGHT

Table A.2: *Information about control subjects: Age at time of MRI acquisition and handedness.*

A.3 Statistical analysis

Diffusion data of children with CP and control subjects were fitted with the DIAMOND model.
The mean and SD of each metric were computed on the cortico-spinal tract (CST) and statistical analyses were performed on these measurements. A visual comparison was done with boxplots and validated with t-tests.
The objective of this thesis is to investigate the microstructural brain changes in the CST, due to CP with bilateral lesions. The comparison between the control subjects and the children with CP were performed to highlight these changes.
Afterwards, the relation between the two hemispheres was analyzed. Even if the children with CP have bilateral lesions, one side of the body is more affected (see Table A.1). The comparison of the hemispheres was investigated to find the link between this functional asymmetry and the CST structure.
Since the AD, RD and FA parameters were computed by both the DTI model and the DIAMOND model, the results and metrics output of these two models can be compared.
Finally, the behavioural surveys results were evaluated, to find a correlation between the microstructural metrics and the behavioural scores.

A.3.1 Comparison of CP subjects vs. control

The first comparison was between the control subjects and the children with CP. In this section, first the mean and afterwards the standard deviation of the DIAMOND metrics were analyzed.

Mean

The first statistical parameter analyzed between the two populations and for all the DIAMOND metrics was the mean. The comparisons for both hemispheres for the free water diffusivity (FD) and the Mose metrics are shown in Fig.A.1; for the wFA, the wAD and the wRD metrics in Fig.A.2; for the fraction of the different compartments in Fig.A.3; and the heterogeneity of the compartment 0 and 1 in Fig.A.4.

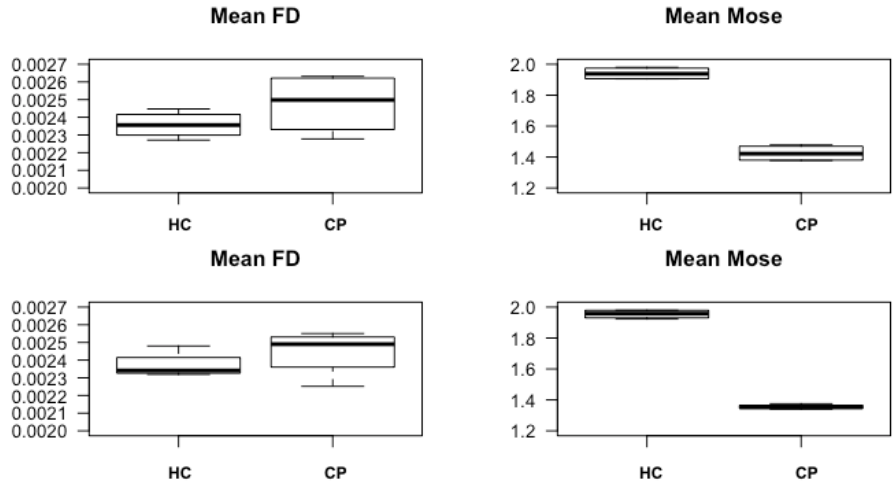

Fig A.1: *Boxplots comparing the FD and the Mose metrics between control subjects (HC) and children with CP (CP) for the dominant hemisphere (on the top) and non-dominant hemisphere (on the bottom).*

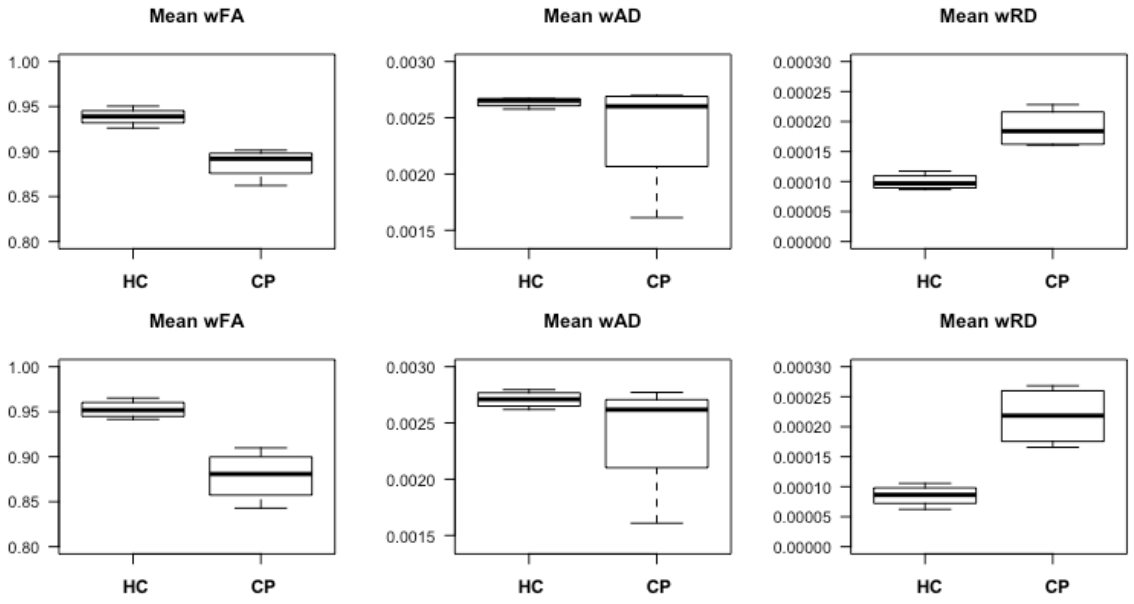

Fig A.2: *Boxplots comparing the wFA, the wAD and the wRD metrics between control subjects (HC) and children with CP (CP) for the dominant hemisphere (on the top) and non-dominant hemisphere (on the bottom).*

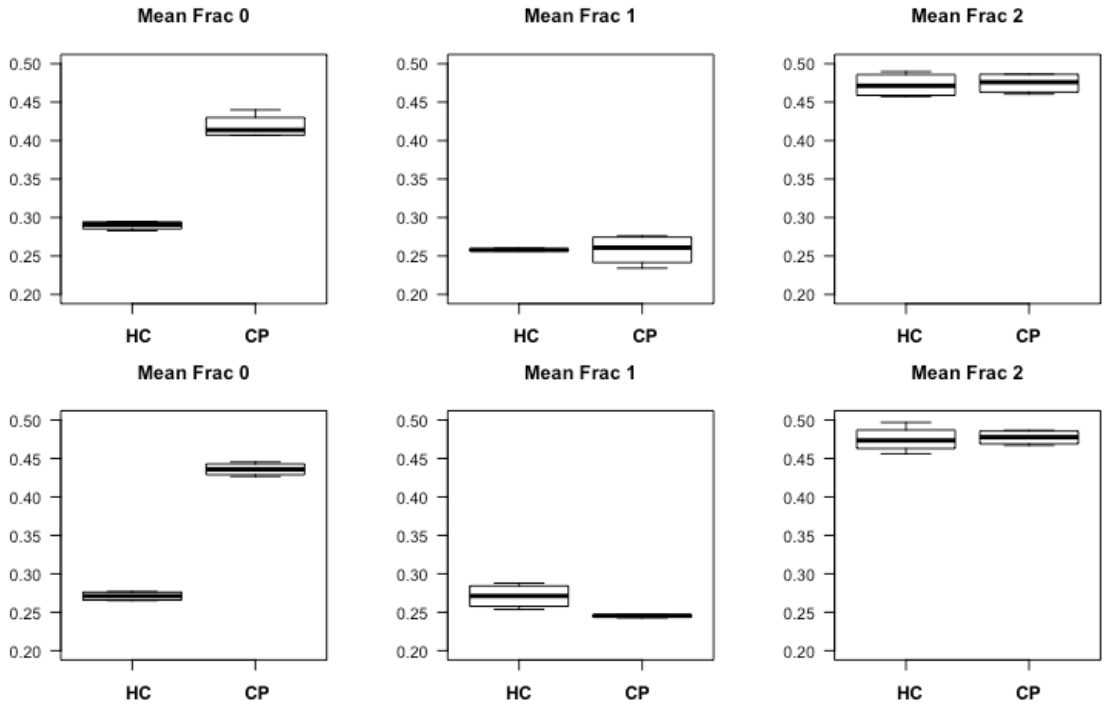

Fig A.3: *Boxplots comparing the fraction of the different compartments between control subjects (HC) and children with CP (CP) for the dominant hemisphere (on the top) and non-dominant hemisphere (on the bottom). 0 corresponding to the main fiber population, 1 to the second population fiber and 2 to the isotropic compartment.*

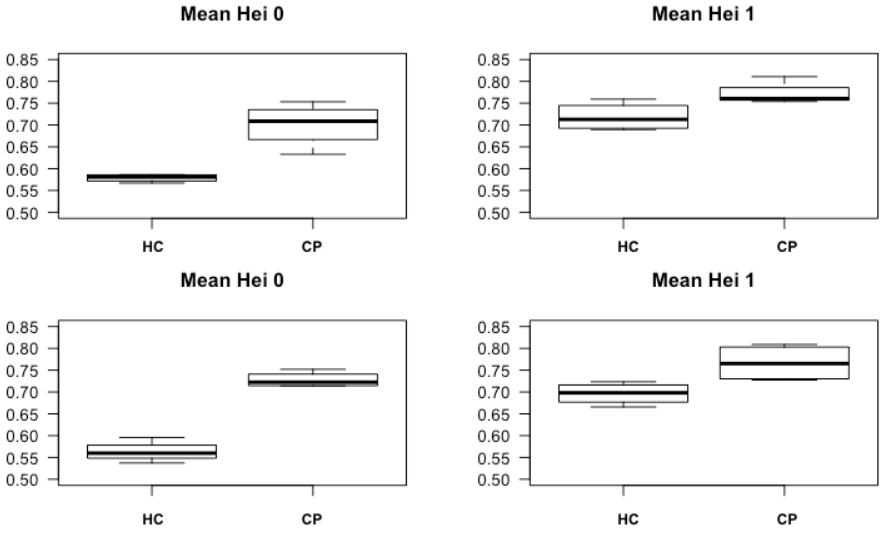

Fig A.4: *Boxplots comparing the heterogeneity of the compartment 0 (the main fiber population) and 1 (the second fiber population) between control subjects (HC) and children with CP (CP) for the dominant hemisphere (on the top) and non-dominant hemisphere (on the bottom).*

T-test Mean HC/CP D				
Mean_FD	t = -0.98568	df = 4.6896	p-value =	0.3724
Mean_Mose	t = 37.154	df = 4.4839	p-value =	**9.35E-07**
Mean_wFA	t = 4.9041	df = 3.7573	p-value =	**0.009399**
Mean_wAD	t = 1.1267	df = 3.1215	p-value =	0.339
Mean_wRD	t = -5.0002	df = 3.7788	p-value =	**0.008681**
Mean_frac_0	t = -31.539	df = 5.3992	p-value =	**2.48E-07**
Mean_hei_0	t = -10.951	df = 5.5065	p-value =	**6.04E-05**
Mean_frac_1	t = 3.2279	df = 3.0731	p-value =	**0.04668**
Mean_hei_1	t = -2.8502	df = 4.8814	p-value =	**0.03681**
Mean_frac_2	t = -0.23515	df = 4.7759	p-value =	0.8238

T-test Mean HC/CP ND				
Mean_FD	t = -1.255	df = 4.1031	p-value=	0.2762
Mean_Mose	t = 15.694	df = 5.5773	p-value =	**7.91E-06**
Mean_wFA	t = 5.1956	df = 4.8144	p-value =	**0.003883**
Mean_wAD	t = 0.99958	df = 3.0427	p-value =	0.390234304
Mean_wRD	t = -5.0708	df = 3.991	p-value =	**0.007169**
Mean_frac_0	t = -15.628	df = 3.7567	p-value =	**0.000148448**
Mean_hei_0	t = -4.7725	df = 3.1924	p-value =	**0.01515**
Mean_frac_1	t = 0.0096604	df = 3.043	p-value =	0.992955
Mean_hei_1	t = -2.5187	df = 5.7651	p-value =	**0.0469664**
Mean_frac_2	t = -0.22046	df = 5.8372	p-value =	0.8334755

Table A.3: *T-test results for the comparison of the mean of the different DIAMOND metrics between healthy control subjects (HC) and children with CP (CP). The dominant (D) hemisphere on the top and the non-dominant (ND) hemisphere on the bottom. In green: the p-values inferior to 0.05 (significant level).*

The increase of Free Water Diffusivity in children with CP that can be observed in the boxplots (Fig.A.1) was not confirmed by the t-tests due to its high variance between the different subjects.

The wFA and wRD have the same behavior than the FA and RD in the DTI analysis: a lower value of the wFA and a higher value of wRD was observed in children with CP compared to control subjects. This is explained by the absence of the maturation process in the CST for both hemispheres compared to a normal development where the maturation continues to CST development during childhood [62]. The mean wAD computed by this model did not change between the children with CP and the control population. AD reportedly does not decrease during prolonged demyelination, in which axonal atrophy is evident [63]. As explained before, the AD modification is not conclusive between the different authors.

The major difference between DIAMOND and the other models is that the different compartments and their heterogeneity are taken into account. The model selection map (Mose map) corresponds to the number of population in each voxel. The visual

result for a complete slice is shown in Fig.A.5. On the CP map, the voxels in the CST were mainly composed of one population (in gray) compared to the control map, where the majority of voxels have been modeled by two fiber populations (in black). This visual result was confirmed by the boxplots and the t-test.

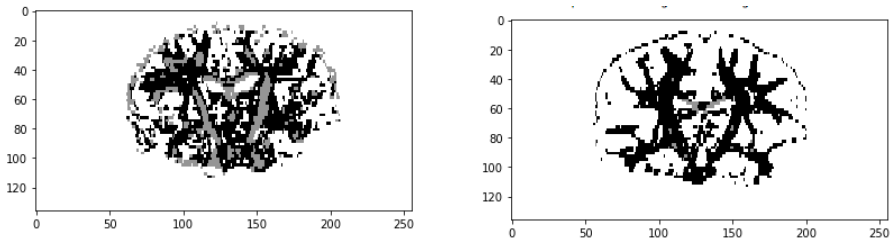

Fig A.5: *Mose map for children with CP on the left and control population on the right. White: 0 population of fibers, Gray: 1 population of fibers and Black: 2 populations of fibers.*

An equivalent way to see that is with the fraction of each population (Frac(Pi)). The fraction of compartment 0, corresponding to the first anisotropic population was higher in the population with CP. The comparison of the fraction attributed to compartment 1 and 2 is not relevant due to the high variation between the subjects.

The last parameter is the heterogeneity, which was higher for the two anisotropic compartments in children with CP than in the control subjects.
In children with CP, a higher fraction of fiber population 1, a lower the fraction of fiber population 2 and a higher heterogeneity were observed. These parameters highlight the non-alignment of the CST fibers in children with CP.

Moreover, since the proportion of voxels modeled with a single fiber population is higher with CP patients, it is to be expected that the heterogeneity increases, as this single fiber population models all the orientation variations that are modeled with two fiber populations in the control patients.

Standard deviation

The second statistical parameter analyzed between the two populations and for all of the DIAMOND metrics is the Standard Deviation (SD). The comparison for both hemispheres for the FD and the Mose parameters is shoxn in Fig.A.6; for wFA, wAD and wRD in Fig.A.7; for the fraction of the different compartments in Fig.A.8; and the heterogeneity of the compartment 0 and 1 in Fig.A.9.

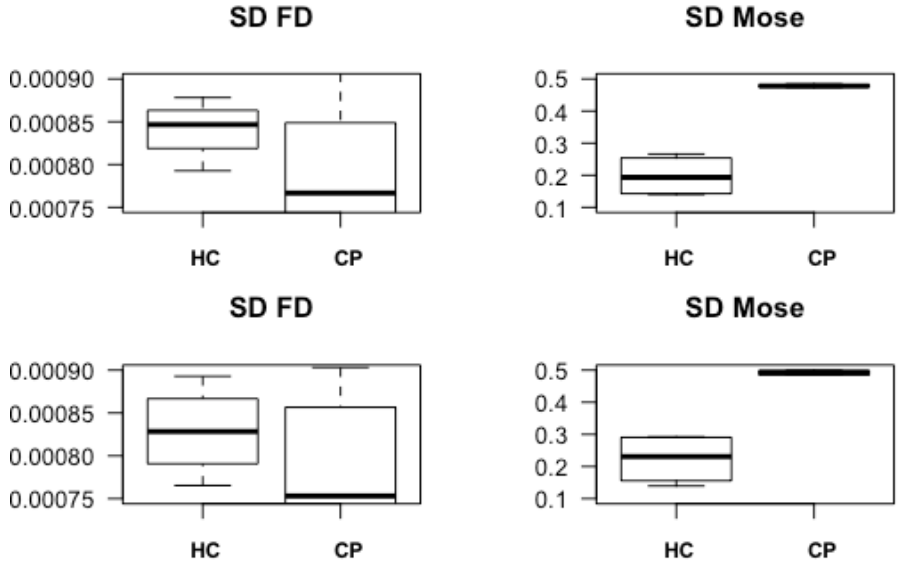

Fig A.6: *Boxplots comparing the SD of the FD and the Mose metrics between control subjects (HC) and children with CP (CP) for the dominant hemisphere (on the top) and non-dominant hemisphere (on the bottom).*

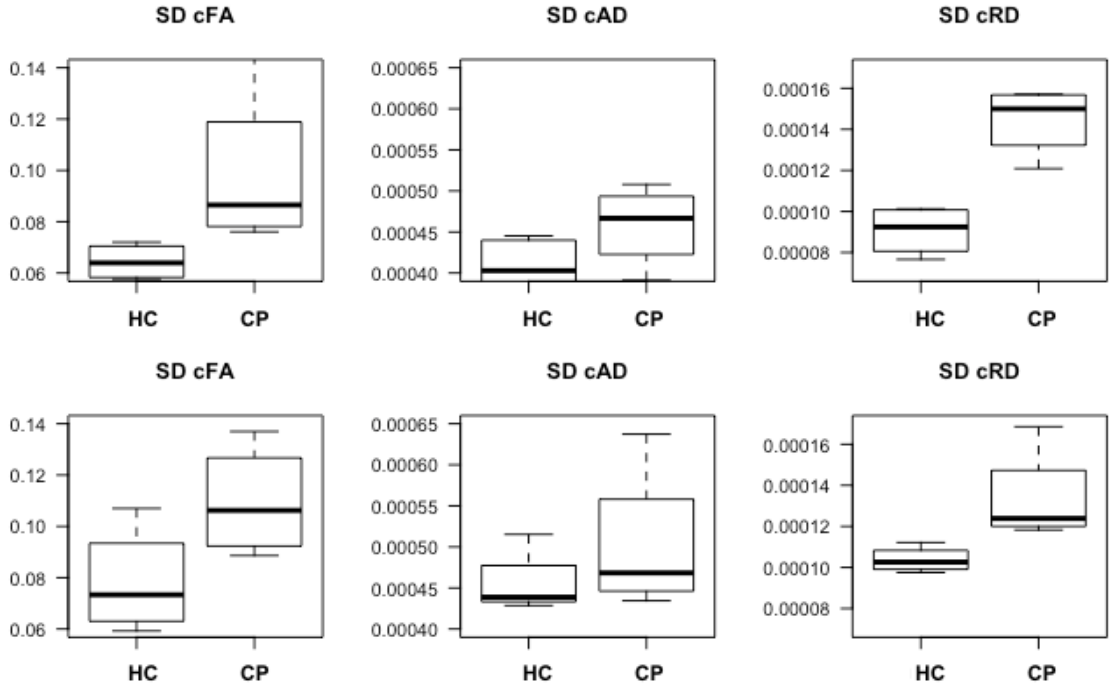

Fig A.7: *Boxplots comparing the SD of the wFA, the wAD and the wRD metrics between control subjects (HC) and children with CP (CP) for the dominant hemisphere (on the top) and non-dominant hemisphere (on the bottom).*

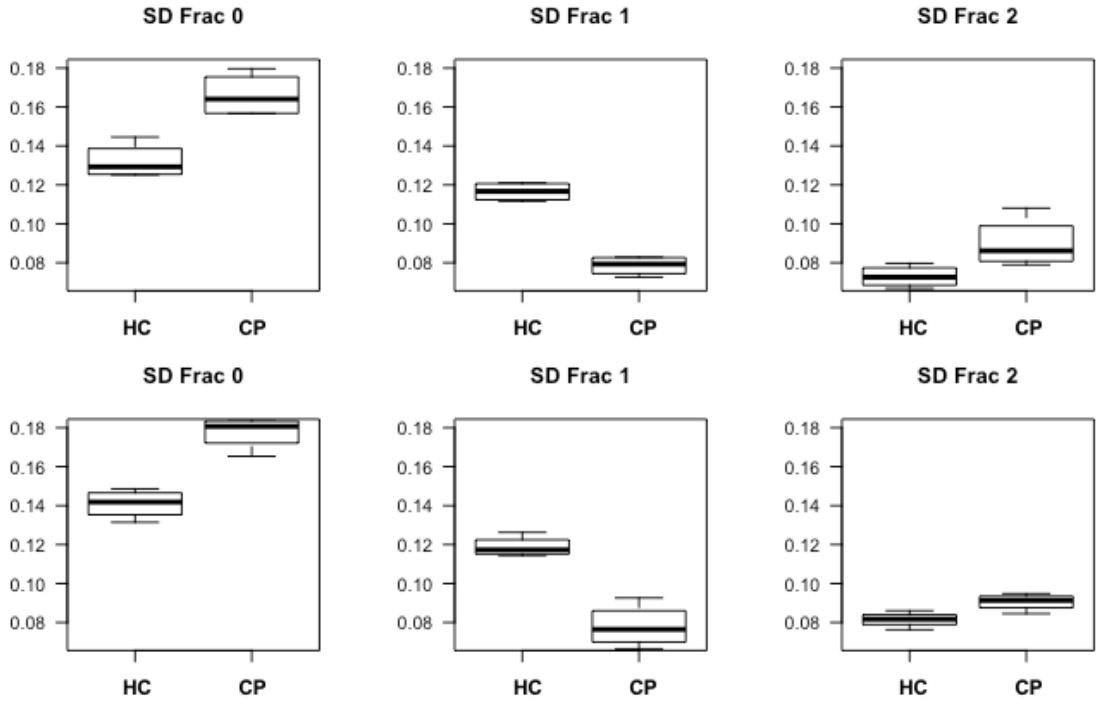

Fig A.8: *Boxplots comparing the SD of the fraction of the different compartments between control subjects (HC) and children with CP (CP) for the dominant hemisphere (on the top) and non-dominant hemisphere (on the bottom). 0 corresponding to the main fiber population, 1 to the second population fiber and 2 to the isotropic compartment.*

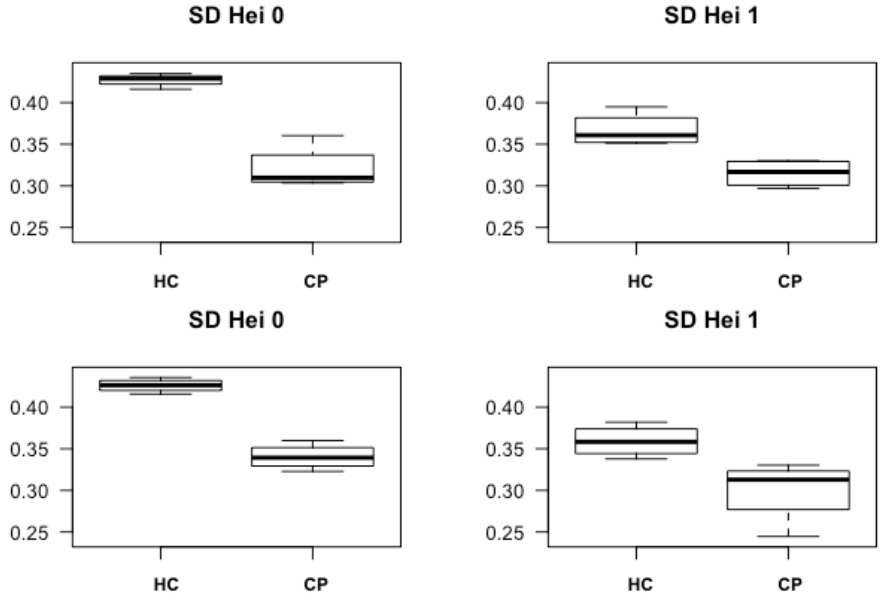

Fig A.9: *Boxplots comparing the SD of the heterogeneity of the compartment 0 (the main fiber population) and 1 (the second fiber population) between control subjects (HC) and children with CP (CP) for the dominant hemisphere (on the top) and non-dominant hemisphere (on the bottom).*

T-test SD CP/C D				
SD_FD	t = 1.0603	df = 4.2033	p-value =	0.3461
SD_Mose	t = -8.6102	df = 3.0269	p-value =	**3.18E-03**
SD_wFA	t = -2.0944	df = 3.3051	p-value =	0.1188
SD_wAD	t = -1.6778	df = 5.8935	p-value =	0.1453
SD_wRD	t = -5.1724	df = 5.4287	p-value =	**0.00279**
SD_frac_0	t = -4.699	df = 5.7171	p-value =	**0.003779**
SD_hei_0	t = 7.6355	df = 3.521	p-value =	**0.002602**
SD_frac_1	t = 10.904	df = 5.9968	p-value =	**3.54E-05**
SD_hei_1	t = 3.9479	df = 5.8199	p-value =	**0.008032**
SD_frac_2	t = -2.3911	df = 4.1091	p-value =	0.07337

T-test SD CP/C ND				
SD_FD	t = 1.0052	df = 4.2776	p-value =	0.3682
SD_Mose	t = -6.7613	df = 3.0602	p-value =	**6.21E-03**
SD_wFA	t = -2.0706	df = 5.9923	p-value =	0.08388
SD_wAD	t = -0.93259	df = 4.1092	p-value =	0.4025
SD_wRD	t = -2.4614	df = 3.4285	p-value =	0.08014
SD_frac_0	t = -6.4804	df = 5.8741	p-value =	**6.98E-04**
SD_hei_0	t = 9.7673	df = 4.5969	p-value =	**3.02E-04**
SD_frac_1	t = 6.6454	df = 4.2957	p-value =	**0.002059**
SD_hei_1	t = 2.771	df = 4.4227	p-value =	**0.04497**
SD_frac_2	t = -3.0675	df = 5.9591	p-value =	**0.02221**

Table A.4: *T-test results for the comparison of the Standard Deviation of the different DIAMOND metrics between control subjects and children with CP. The dominant hemisphere on the top and the non-dominant hemisphere on the bottom. In green: the p-values inferior to 0.05 (significant level).*

Contrarily to the DTI and the NODDI models, in the DIAMOND model, some t-tests were relevant for the SD comparison in both hemispheres, the SD of Mose was higher in subjects with CP than in control patients. The SD of the fraction of compartment 0 was higher in children with CP and the SD of the fraction of compartment 1 was lower.
This is coherent with the comparison of the means. Indeed, in children with CP the fraction of compartment 0 was higher, the variation of this metric is by consequence more susceptible to change, and to have a higher SD. Reciprocally, in the control population, the fraction of compartment 1 was higher so the SD of fraction 1 was higher as well.
The SD of the heterogeneity of both populations was lower in the population with CP. The mean of the heterogeneity was higher is children with CP, with a low SD. This means that the heterogeneity is high and constant across all the CST.

A.3.2 Comparison between the two hemispheres

After comparing the two populations, the analysis of the two hemispheres was investigated. Even if children with CP have lesions in both sides of the brain, they have functional asymmetry. The aim of this section is to investigate if this asymmetry is present in the brain structure. The comparison for the control subjects and children with CP for FD and Mose is shown in Fig.A.10; for wFA, wAD and wRD in Fig.A.11; for the fraction of the different compartments in Fig.A.12; and the heterogeneity of the compartment 0 and 1 in Fig.A.13.

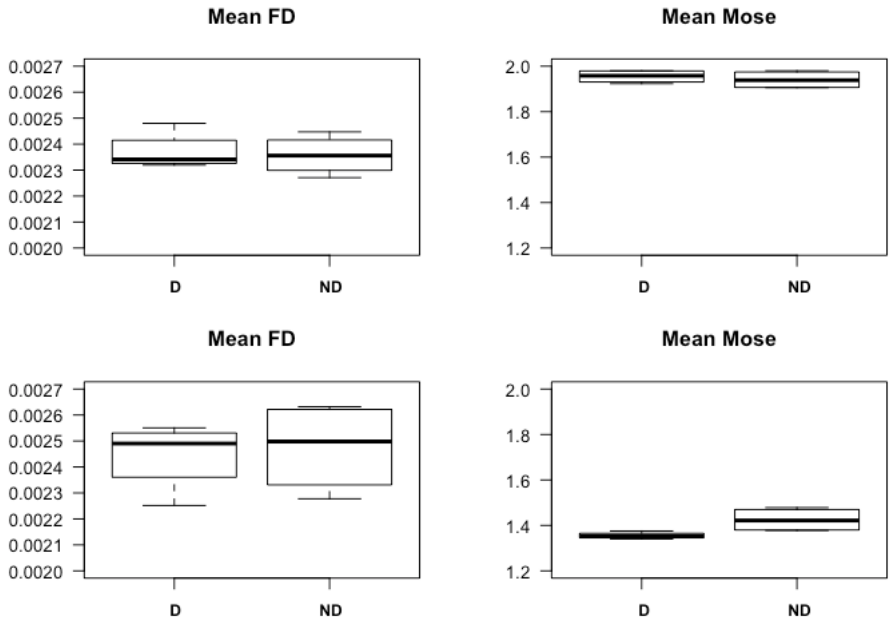

Fig A.10: *Boxplots comparing two hemispheres of the FD and the Mose metrics for the control subjects (on the top) and the children with CP (on the bottom).*

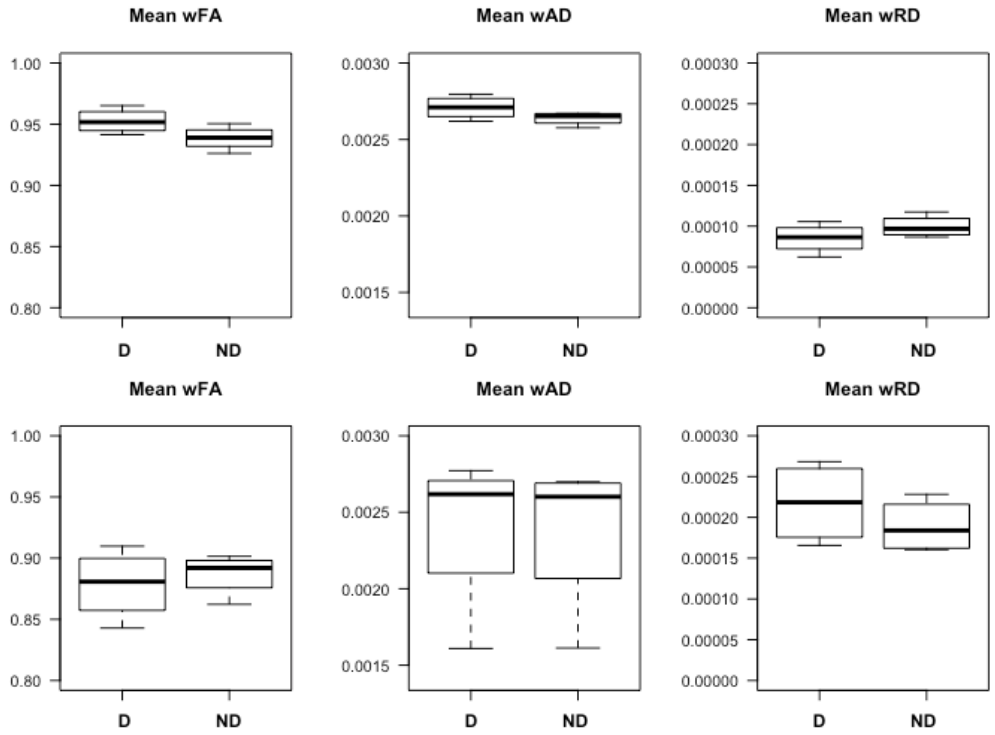

Fig A.11: *Boxplots comparing two hemispheres of the wFA, the wAD and the wRD metrics for the control subjects (on the top) and the children with CP (on the bottom).*

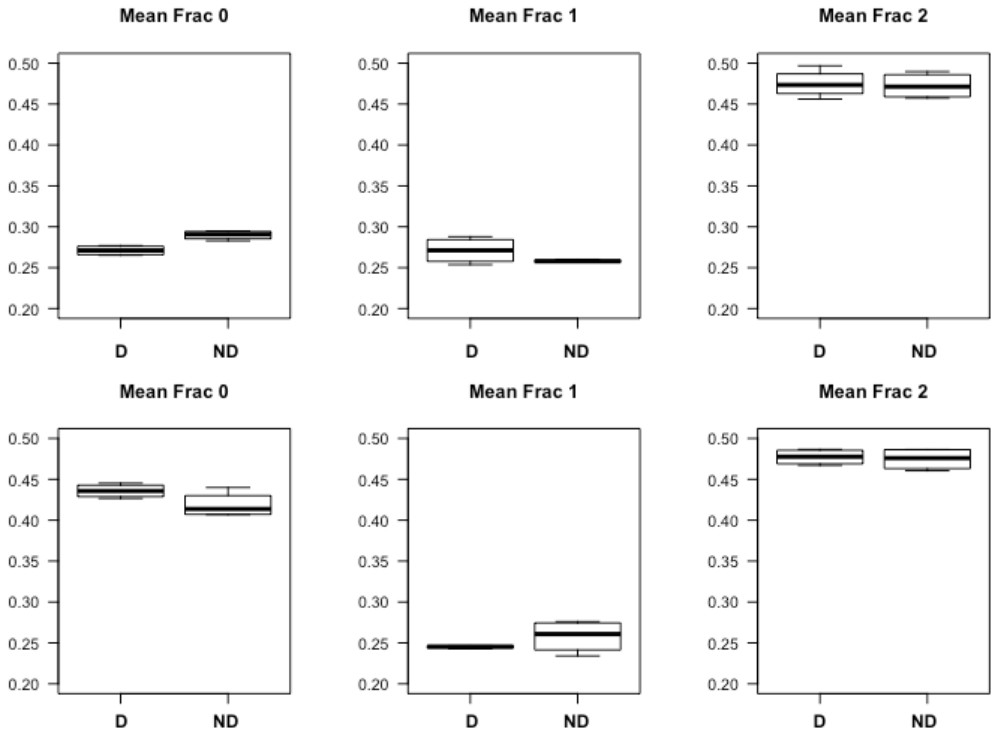

Fig A.12: *Boxplots comparing two hemispheres for the fraction of the different compartments for the control subjects (on the top) and the children with CP (on the bottom). 0 corresponding to the main fiber population, 1 to the second population fiber and 2 to the isotropic compartment.*

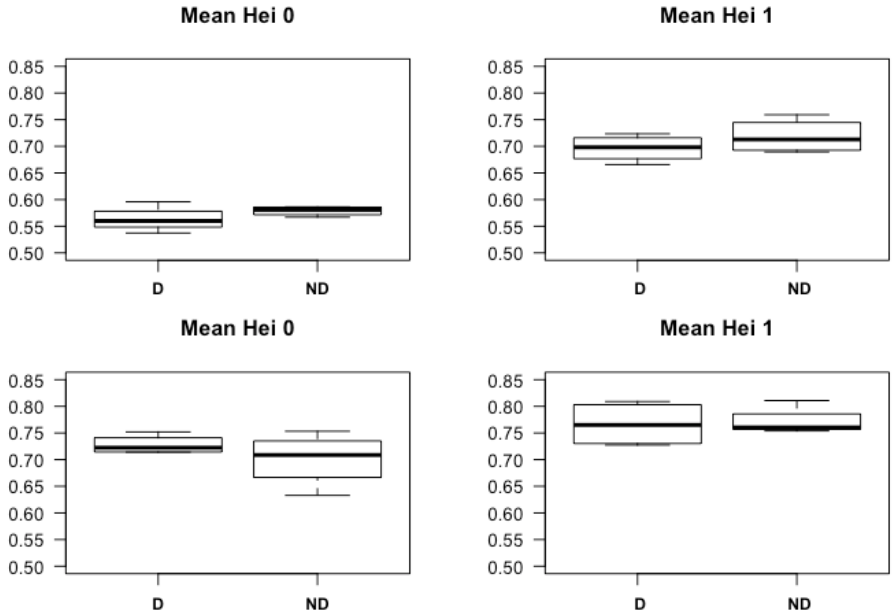

Fig A.13: *Boxplots comparing two hemispheres for the heterogeneity of the compartment 0 (the main fiber population) and 1 (the second fiber population) for the control subjects (on the top) and the children with CP (on the bottom).*

T-test Mean D/ND HC			
Mean_FD	t = -0.42568	df = 3	p-value = 0.699
Mean_Mose	t = -2.1156	df = 3	p-value = 1.25E-01
Mean_wFA	t = -6.6662	df = 3	p-value = **0.006882**
Mean_wAD	t = -2.7154	df = 3	p-value = 0.07283
Mean_wRD	t = 2.8596	df = 3	p-value = 0.0646
Mean_frac_0	t = 4.2638	df = 3	p-value = **0.02367**
Mean_hei_0	t = 1.0708	df = 3	p-value = 0.3627
Mean_frac_1	t = -1.7761	df = 3	p-value = 1.74E-01
Mean_hei_1	t = 0.8383	df = 3	p-value = 0.4634
Mean_frac_2	t = -0.36176	df = 3	p-value = 0.7415

T-test Mean D/ND CP			
Mean_FD	t = 0.43021	df = 3	p-value = 0.6961
Mean_Mose	t = 2.2159	df = 3	p-value = 1.14E-01
Mean_wFA	t = 1.3102	df = 3	p-value = 0.2814
Mean_wAD	t = -0.90594	df = 3	p-value = 0.4318
Mean_wRD	t = -3.0071	df = 3	p-value = 0.05734
Mean_frac_0	t = -2.1754	df = 3	p-value = 1.18E-01
Mean_hei_0	t = -1.1191	df = 3	p-value = 3.45E-01
Mean_frac_1	t = 1.3726	df = 3	p-value = 0.2635
Mean_hei_1	t = 0.31995	df = 3	p-value = 0.77
Mean_frac_2	t = -0.93618	df = 3	p-value = 0.4182

Table A.5: *T-test results for the comparison of the different DIAMOND metrics between dominant hemisphere and the non-dominant hemisphere, for the control (HC) population on the top and the population with CP (CP) on the bottom. In green: the p-values inferior to 0.05 (significant level).*

As for the other models, the t-tests did not highlight any significant differences between the two hemispheres for the different metrics neither for the control subjects nor for the children with CP (see Table A.5).

Correlation D/ND	Controle	CP
Mean_FD	0.6758973	0.5964105
Mean_Mose	**0.9734486**	-0.6232565
Mean_wFA	**0.9146725**	**0.9599007**
Mean_AD	0.7495047	**0.9948356**
Mean_RD	0.8396045	**0.9790696**
Mean_frac_0	-0.1539334	0.2345999
Mean_hei_0	-0.3815487	0.3073608
Mean_frac_1	0.8446262	0.7260594
Mean_hei_1	-0.6915516	0.717303
Mean_frac_2	0.6391275	**0.9432417**

Table A.6: *Correlation results between the two hemispheres for the control population on the left and the children with CP on the right. In green: the correlations superior to 0.9.*

As for the other models, the t-tests do not highlight any significant differences between the two hemispheres for the different metrics (see Table A.5). Even the correlation results are limited. The wFA, wAD and wRD are, as the FA, AD and RD of the DTI model, correlated in CP but the other parameters do not give any reliable results (Table A.6).

A.3.3 Models comparison

The FA, SD and RD are estimated by the DTI and DIAMOND models. The estimation of these metrics by the two models were compared (Fig.A.14).

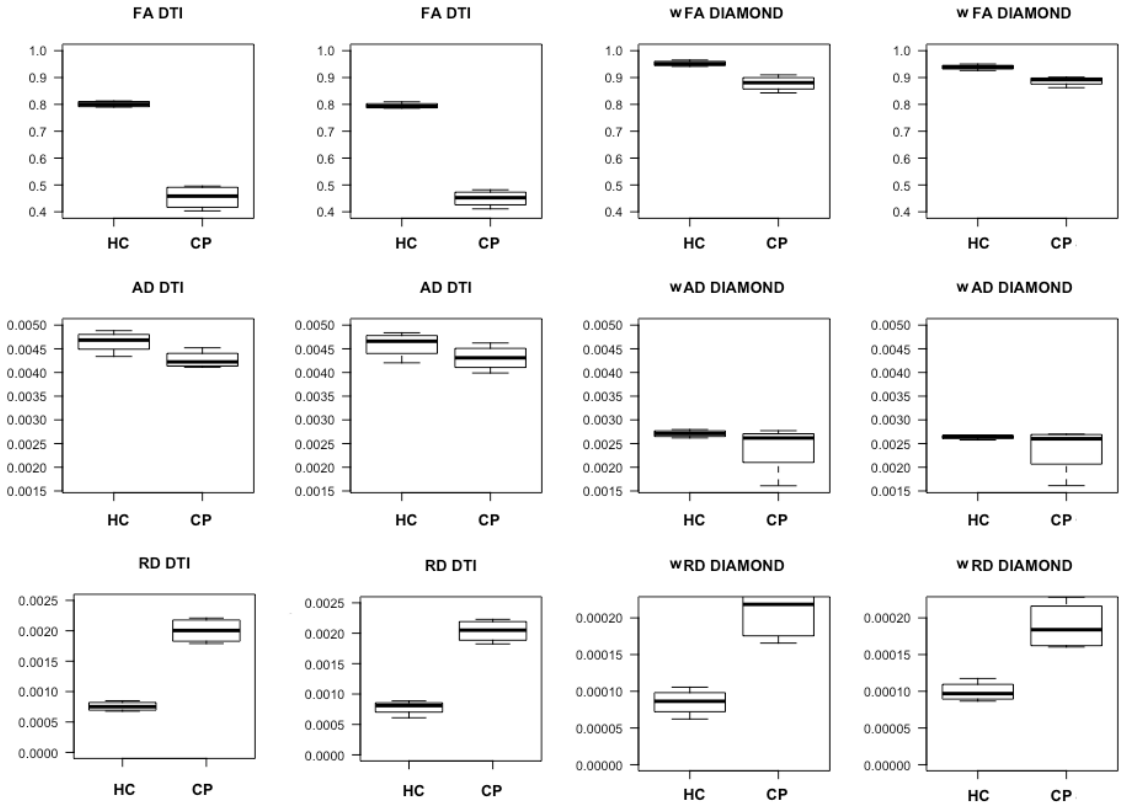

Fig A.14: *Comparison between FA, AD and RD for DTI and DIAMOND models, for non dominant (column 1 and 3) and dominant (column 2 and 4) hemispheres, with both models on the same scale.*

In DIAMOND, the wFA computed from the compartment-specific cFAs (see Section A.1 for the formula used) does not take into account the isotropic diffusion compartment but only the FA due to the two fiber populations. By consequence, it is logical that the values found are higher than those found with DTI. For example, considering a voxel filled only with two perpendicular fiber populations (Fig.A.15), the resulting FA found by DTI will be close to 0 (since both fiber populations "cancel" each other's anisotropy by being considered as a single population), whereas DIAMOND will output a FA close to 1 for both fiber populations.

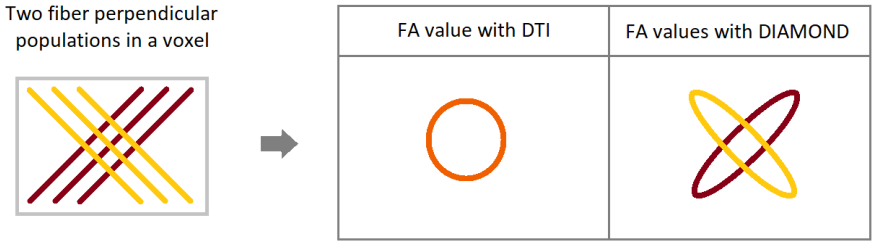

Fig A.15: *Schematic representation of the FA estimation of a voxel filled with only two perpendicular fiber populations by DTI and DIAMOND. DTI: isotropic diffusion (represented by a sphere) and a FA close to 0. DIAMOND: anisotropic diffusion (represented by two ellipses) and a FA tending to 1.*

For both models, the difference of AD was not significant. Comparing this value between the two models is by consequence not relevant. For the RD, since there is more anisotropy considered by DIAMOND, there is less radial diffusivity. The opposite conclusion of FA is therefore found.

A.3.4 Behavioral analysis

A correlation was calculated between each behavioural score (PEDI daily life and mobility, ACTILIM in logit and percent) and the mean of each DIAMOND metric for both dominant (D) and non-dominant (ND) hemispheres. The behavioural questionnaire was only asked to the parents of children with CP. By consequence, the following results only concern this population.

Since the number of children with CP is low (4 subjetcs), this analysis did not give any coherent and significant results is only given for information. The results are given for information in Table A.7.

Behaviour	PEDI_DA	PEDI_M	AL_L	AL_P
FD_D	-0,5930768	**-0,9593203**	0,2569482	-0,4470477
FD_ND	0,2628806	0,3587003	-0,5256319	-0,4779515
Mose_D	-0,5272538	-0,07501634	-0,7846641	0,7583355
Mose_ND	**0,9796921**	-0,4544248	-0,8826397	0,1826865
wFA_D	-0,3044933	-0,03034966	-0,5690246	-0,4658101
wFA_ND	**0,9414448**	0,8118169	-0,8575947	-0,6843213
wAD_D	0,3147016	0,3914059	-0,1772841	-0,1631328
wAD_ND	0,5613578	0,4931146	-0,4317119	-0,3449729
wRD_D	0,8662232	**0,9327195**	0,3406126	0,3477304
wRD_ND	-0,1326759	-0,2853849	0,2559374	0,4297196
Frac_0_D	-0,7048697	-0,5020835	-0,4116669	**-0,9818231**
Frac_0_ND	-0,05261491	0,7702062	0,005166984	-0,5896415
Hei_0_D	**-0,9279194**	-0,1808571	-0,8391393	-0,2662525
Hei_0_ND	0,6681192	-0,4613549	-0,6514726	0,5211347
Frac_1_D	**-0,9560269**	-0,7361319	-0,337107	-0,5747963
Frac_1_ND	0,3944276	0,07852191	-0,5526786	-0,08171727
Hei_1_D	0,5511919	0,8300625	0,2745103	0,09235229
Hei_1_ND	-0,8750166	-0,4929165	**0,9604015**	0,7059805
Frac_2_D	**0,9006242**	0,8353643	0,6766274	0,3975386
Frac_2_ND	-0,3576174	-0,09654622	0,3799105	0,1900398

Table A.7: *Table with the correlation values between behavioural scores and the DIAMOND metrics. PEDI_DA=PEDI-CAT for daily activities domain, PEDI_M=PEDI-CAT for mobility domain, AL_L= ACTIVLIM in [Logit] and AL_P= ACTIVLIM in [%]. In green: the correlation superior to 0.9; in red: the correlations inferior to -0.9.*

Conclusion

In conclusion, the DIAMOND model highlights the same conclusion for the FA and RD than the DTI model. Moreover, it shows the non-parallel fiber structure in children with CP, with the heterogeneity and the fraction population parameters.

Appendix B

Further information

B.1 Functional magnetic resonance imaging (fMRI)

Functional magnetic resonance imaging is an application of MRI which allows the visualization of cerebral activity, although in a indirect manner. When specific brain regions are activated by the task asked of the patient, the slight increase in oxygen consumption by the neurons is over-compensated by a large increase of blood flow. This leads to a diminished desoxyhemoglobin concentration. Due to the paramagnetic properties of desoxyhemoglobin, the MRI signal decreases slightly during the activation periods [64].

fMRI is composed of echo-planar T_2^* sequences. This allows to obtain a Blood Oxygen Level Dependent (BOLD) signal.
This BOLD signal is based on two principles:

- the oxyginated red blood cells are rich in oxyhemoglobin (oxyHb), non-visible molecules in MRI
- the de-oxyginated red blood cells contain desoxyhemoglobin (deoxyHb) which are paramagnetic, and are thus visible with MRI

When part of the cortex is activated to accomplish a task, the quantity of oxyHb decreases and deoxyHb increases. After a time period of 2 to 6 seconds, a local blood flow input is allocated to the activated zone and the quantity are inverted: oxyHb increases and deoxyHb decreases. T_2^* weighted sequence can detect these changes [64].

fMRI is particularly sensitive to movement artefacts.

B.2 The NIfTI format

The two main formats available to store information during this thesis were DICOM (`.dcm`) and NIfTI (`.nii`).

The DICOM (Digital Imaging and Communications in Medicine) format is well-known as an international standard to transmit, store, retrieve, process, and display medical imaging information [65].
However, since the way the dicom files were recorded created 167 individual files per scan (instead of a single file) and since the `DIPY` Python library functions seemed to be centered around the use of NIfTI files, the dicom files were converted to NIfTI using *MRIcroN*.

The NIfTI (Neuroimaging Informatics Technology Initiative) format was created to improve the compatibility of informatics tools related to neuroimaging. The goal was thus to improve the interoperability at the file-exchange level between MRI data analysis software. This is the format used during this thesis. With the help of Python packages, the NIfTI files could be easily accessed and created to analyse data and compare it between scans.

B.3 Tract-based spatial statistics (TBSS)

Many of the articles reviewed for this thesis have used Tract-based spatial statistics (TBSS) to compare metrics along major white matter tracts in different subject populations, this algorithm is available in *FSL*.

TBSS is an automated, observer-independent approach developed by Smith & al. [66] used to assess the fractional anisotropy in the major white matter tracts on a voxel-wise basis across groups of subjects. Many imaging studies were starting to use FA images in voxelwise statistical analyses, to localise and quantify brain changes due to development or diseases. However, the use of registration algorithms in between subjects raised the question of how to align FA images obtained in a manner that was not arbitrary and allowed an objective analysis. Smith & al. introduced TBSS, which uses nonlinear registration, followed by a projection onto an alignment-invariant tract representation (called the "mean FA skeleton"), in order to compare more accurately white matter tracts across different subject populations.

TBSS was not used during this thesis since its main objective is to compare the statistical significance of parameters such as FA across populations and this report compares a single patient before and after abstinence. Furthermore, since the patient is the same, the comparison of regions after registration did not require a mean FA skeleton for the analysis.

Appendix C

Additional data

C.1 b-value

0 1000 1000 1000 1000 1000 1000 1000 1000 1000 1000 1000 1000 1000 1000 1000 1000 1000 1000 1000 1000 1000 1000 1000 1000 1000 1000 1000 1000 1000 1000 1000 1000 1000 1000 1000 1000 1000 1000 1000 1000 1000 1000 1000 1000 1000 1000 1000 1000 1000 1000 1000 1000 1000 1000 1000 1000 1000 1000 1000 1000 1000 1000 1000 1000 0 2000 2000 2000 2000 2000 2000 2000 2000 2000 2000 2000 2000 2000 2000 2000 2000 0 2000 2000 2000 2000 2000 2000 2000 2000 2000 2000 2000 2000 2000 2000 2000 2000 0 3000 3000 3000 3000 3000 3000 3000 3000 3000 3000 3000 3000 3000 3000 3000 3000 0 3000 3000 3000 3000 3000 3000 3000 3000 3000 3000 3000 3000 3000 3000 3000 3000 3000 0 5000 5000 5000 5000 5000 5000 5000 5000 5000 5000 5000 5000 5000 5000 5000 5000 0 5000 5000 5000 5000 5000 5000 5000 5000 5000 5000 5000 5000 5000 5000 5000 5000 5000

C.2 b-vector

0 -0.447214 -0.000894 0.011628 -0.264303 0.105542 0.399362 -0.355982 -0.104648 -0.418592 -0.22629 -0.154736 -0.204377 0.217793 0.276378 -0.258042 0.369846 -0.399809 -0.129692 -0.051877 0.357771 -0.229868 0.352852 -0.424406 -0.104201 -0.009391 -0.097045 -0.346143 0.072001 0.06574 -0.397126 0.251334 0.170388 -0.136847 0.148475 0.430667 0.428878 -0.202588 0.345696 -0.317074 0.309919 -0.305 0.063504 0.330938 0.046063 -0.261173 0.039355 0.246862 -0.374765 -0.162339 0.082287 0.322441 -0.193643 -0.224501 -0.076474 -0.20706 -0.172177 0.318863 -0.116276 -0.000447 -0.016547 -0.254912 0.126114 -0.322441 -0.119406 0 -0.632456 -0.312433 0.075895 -0.581227 0.070835 0.578064 -0.430702 -0.042375 -0.580594 -0.280178 -0.13661 -0.303579 0.347851 0.443351 -0.271323 0.442086 0 -0.459163 -0.246658 -0.108782 0.385798 -0.378841 0.460428 -0.558458 -0.202386 -0.027828 -0.119534 -0.462957 -0.195429 -0.180882 -0.543279 0.067673 0.188472 0 -0.774597 -0.382651 0.092952 -0.711854 0.086755 0.707981 -0.5275 -0.051898 -0.71108 -0.343146 -0.167313 -0.371806 0.426028 0.542992 -0.332302 0.541443 0 -0.562357 -0.302093 -0.133231 0.472504 -0.463983 0.563906 -0.683969 -0.247871 -0.034082 -0.146399 -0.567005 -0.23935 -0.221535 -0.665379 0.082882 0.23083 0 -1 -0.494 0.12 -0.919 0.112 0.914 -0.681 -0.067 -0.918 -0.443 -0.216 -0.48 0.55 0.701 -0.429 0.699 0 -0.726 -0.39 -0.172 0.61

-0.599 0.728 -0.883 -0.32 -0.044 -0.189 -0.732 -0.309 -0.286 -0.859 0.107 0.298 0 0 0.447214 0.290242 -0.342566 -0.23434 -0.115828 0.057691 0.415909 0.06261 -0.377895 -0.37879 -0.282192 -0.173966 0.300975 -0.046957 -0.232998 -0.017889 -0.241943 -0.430667 0.180227 0.375659 0.068424 -0.104201 0.350168 -0.084076 -0.427536 -0.270117 0.159208 0.326913 0.186488 0.103754 0.063952 -0.088996 -0.058138 -0.118512 0.091679 -0.397573 0.28085 0.182463 0.010733 0.236576 -0.32423 0.173519 0.36761 -0.266539 -0.149817 -0.354193 -0.204824 -0.250887 0.175308 -0.309919 0.305 0.308577 -0.227632 0.189171 -0.361796 -0.110462 0.395784 0.034435 -0.403387 -0.135506 0.064846 0.271906 0.429325 0 0 0.549604 0.405404 -0.209343 -0.399079 -0.14926 0.191634 0.631191 0.096766 -0.562885 -0.586286 -0.424378 -0.302314 0.438292 -0.004427 -0.404772 0 0.057553 -0.157481 -0.557193 0.405404 0.435762 0.140405 -0.251717 0.346586 -0.169498 -0.554664 -0.210608 -0.347851 0.542647 0.318758 0.135978 -0.112577 0 0 0.673125 0.496516 -0.256391 -0.48877 -0.182805 0.234703 0.773047 0.118513 -0.689391 -0.718051 -0.519754 -0.370257 0.536795 -0.005422 -0.495742 0 0.070488 -0.192875 -0.68242 0.496516 0.533697 0.17196 -0.308289 0.424479 -0.207592 -0.679321 -0.257941 -0.426028 0.664604 0.390397 0.166538 -0.137878 0 0 0.869 0.641 -0.331 -0.631 -0.236 0.303 0.998 0.153 -0.89 -0.927 -0.671 -0.478 0.693 -0.007 -0.64 0 0.091 -0.249 -0.881 0.641 0.689 0.222 -0.398 0.548 -0.268 -0.877 -0.333 -0.55 0.858 0.504 0.215 -0.178 0 0 0 0.339882 0.112698 0.365821 0.164575 0.264303 0.127009 0.144897 -0.078262 -0.17978 -0.280403 0.349721 0.182016 -0.362243 0.095256 -0.199904 -0.352852 -0.109567 -0.198563 0.077815 -0.266539 0.094362 0.258042 -0.439164 0.088996 0.084971 0.411884 -0.297844 0.086312 -0.355088 0.408753 -0.416356 0.417697 0.019677 0.086312 0.030411 0.039355 0.257148 0.322441 -0.22629 0.301422 0.24552 0.25044 0.246415 0.419486 0.115828 -0.132375 0.332727 -0.402939 0.004025 -0.263409 0.232998 -0.377448 0.348379 0.198563 0.293372 -0.173072 -0.445872 0.192302 -0.341224 -0.423958 0.148475 -0.038013 0 0 0 0.479401 -0.135345 0.485726 0.208078 0.421848 -0.008222 0.232111 0.065143 -0.194164 -0.357337 0.433232 0.10815 -0.571107 0.202386 0 -0.431335 -0.560988 -0.27828 -0.295357 0.258674 -0.410464 0.157481 0.488256 -0.608422 0.280178 -0.375679 0.490785 -0.270059 0.055656 -0.614114 0.593243 0 0 0 0.587144 -0.165764 0.59489 0.254842 0.516656 -0.01007 0.284277 0.079783 -0.237801 -0.437647 0.530599 0.132456 -0.699461 0.247871 0 -0.528275 -0.687067 -0.340823 -0.361737 0.31681 -0.502713 0.192875 0.597989 -0.745162 0.343146 -0.46011 0.601087 -0.330753 0.068165 -0.752133 0.726572 0 0 0 0.758 -0.214 0.768 0.329 0.667 -0.013 0.367 0.103 -0.307 -0.565 0.685 0.171 -0.903 0.32 0 -0.682 -0.887 -0.44 -0.467 0.409 -0.649 0.249 0.772 -0.962 0.443 -0.594 0.776 -0.427 0.088 -0.971 0.938

C.3 Diamond command line

The command line used with the full parameters is the following:

```
/home/rensonnetg/Software/crlDCIEstimate/build/src/crlDCIEstimate -i
/home/ndelinte/Diamond/Data/LC.nii.gz -o /home/ndelinte/Diamond/LC_diamond.nrrd
-m /home/ndelinte/Diamond/Data/T0mask.nii.gz -n 2 -automose aicu -fascicle
diamondcyl -omtm 1 -p 6 -waterfraction 1 -waterDiff -1 -predictedsignal
/home/ndelinte/Diamond/Predicted/LC_predicted.nrrd
```

C.4 All metrics means and standard deviations in 22 regions

	CC		Brain Stem		CorticoSpinalTractL		CorticoSpinalTractR		FornixL		FornixR		riorCerebellarPeduncle		riorCerebellarPedun		LeftInsula		Left Amygdala		t cerebral white Mat	
	T0	T1	T0	T1	T0	T1	T0	T1	T0	T1	T0	T1	T0	T1	T0	T1	T0	T1	T0	T1	T0	T1
FA	0.77544	0.8629	0.61327	0.65929	0.59112	0.579	0.56149	0.56618	0.4376	0.50823	0.46347	0.46977	0.51012	0.57146	0.5297	0.55808	0.24044	0.2689	0.31194	0.35224	0.44357	0.46368
MD	0.00123	0.00123	0.00102	0.001	0.00125	0.00137	0.00121	0.00125	0.00151	0.0016	0.00151	0.00158	0.00094	0.00101	0.00096	0.00107	0.00154	0.0016	0.00148	0.00144	0.00133	0.00143
AD	0.00273	0.00306	0.00188	0.00193	0.00216	0.00228	0.00203	0.00209	0.00228	0.00259	0.00235	0.0025	0.00148	0.00176	0.00153	0.0018	0.00193	0.00205	0.00199	0.00201	0.00201	0.00216
RD	0.00049	0.00031	0.0006	0.00054	0.00079	0.00091	0.0008	0.00083	0.00112	0.0011	0.00109	0.00113	0.00066	0.00063	0.00068	0.0007	0.00135	0.00138	0.00123	0.00115	0.00099	0.00106
MK	0.90975	0.98213	1.00572	1.04441	0.87693	0.86058	0.86672	0.88795	0.7163	0.72201	0.7009	0.69381	0.93857	0.96451	0.94161	0.91898	0.60933	0.59344	0.62551	0.64694	0.75784	0.75705
AK	0.41535	0.38981	0.57759	0.57522	0.49854	0.49025	0.51997	0.52081	0.47684	0.43362	0.46198	0.44601	0.67541	0.58467	0.63388	0.57727	0.50919	0.48305	0.49441	0.49247	0.51054	0.49024
RK	1.50286	1.76255	1.41197	1.51532	1.23141	1.22995	1.17678	1.2441	0.92497	1.00016	0.90502	0.91158	1.1938	1.29472	1.19567	1.19975	0.67507	0.6682	0.7178	0.75591	0.97799	1.01299
KFA	0.63425	0.70088	0.51589	0.55154	0.4902	0.47904	0.46972	0.47178	0.35796	0.41335	0.37864	0.38294	0.46576	0.48558	0.47419	0.47298	0.21711	0.24084	0.27589	0.31269	0.37604	0.3896
MSD	0.00091	0.00081	0.00093	0.00085	0.00096	0.00104	0.00092	0.00097	0.00191	0.00183	0.00181	0.00189	0.00076	0.00076	0.00079	0.00084	0.0011	0.00116	0.00104	0.00096	0.001	0.00104
MKT	0.78007	0.79376	0.92038	0.9493	0.80365	0.7882	0.81027	0.81669	0.677	0.66342	0.66246	0.64993	0.94278	0.89926	0.93236	0.86813	0.60284	0.58512	0.6148	0.63211	0.71646	0.7049
MSK	0.86311	0.96279	0.87084	0.93603	0.83075	0.8287	0.81459	0.83699	0.50082	0.54331	0.5184	0.50227	0.8374	0.90201	0.84576	0.86966	0.60997	0.56885	0.62692	0.62819	0.72401	0.72241
AWF	0.4972	0.55299	0.47619	0.52111	0.50841	0.51798	0.51293	0.52409	0.43768	0.48803	0.38007	0.43093	0.42345	0.4419	0.43787	0.45378	0.37395	0.36924	nan	0.34293	0.449	0.46278
TORT	7E-08	1E-09	5.96429	8610662	8.56166	6390941	10.6586	1.3E-07	5.24944	12.2177	4.96185	6.00996	4.4251	5.90941	5.49056	4.8826	4.13253	4.50232	nan	4.28442	1.2E-08	1.3E-08
ficvf	0.73283	0.80542	0.7981	0.8141	0.64092	0.65503	0.63277	0.66361	0.70553	0.69866	0.69163	0.67577	0.68691	0.66436	0.70726	0.67559	0.38227	0.43133	0.39564	0.46134	0.51042	0.54978
fiso	0.31209	0.26861	0.31978	0.27588	0.25761	0.28552	0.23895	0.25489	0.69341	0.65979	0.6737	0.71413	0.18183	0.14428	0.2235	0.21679	0.21721	0.37357	0.19938	0.2839	0.21598	0.26105
odi	0.19342	0.14942	0.34095	0.31491	0.32975	0.3525	0.34374	0.36618	0.36942	0.33775	0.35598	0.35657	0.40478	0.36238	0.36758	0.35618	0.59599	0.54979	0.51431	0.48618	0.41764	0.42262
fd	0.00267	0.00283	0.00244	0.00231	0.00237	0.00226	0.00227	0.00217	0.00228	0.00243	0.00223	0.00223	0.00212	0.002	0.00222	0.0021	0.00134	0.00124	0.00156	0.00135	0.00206	0.0019
mose	1.39568	1.44346	1.87204	1.93779	1.86018	1.9654	1.85561	1.96539	1.7979	1.78514	1.76424	1.8262	1.97867	2	1.98396	1.99828	1.97121	1.9965	1.94784	1.98815	1.89611	1.95654
frac1	0.40979	0.46081	0.28704	0.32353	0.29716	0.31119	0.29957	0.30908	0.20541	0.2659	0.19579	0.21695	0.2716	0.30572	0.23799	0.27439	0.21601	0.22054	0.21639	0.27597	0.24553	0.28376
hei1	0.71686	0.6473	0.39677	0.36312	0.58571	0.54513	0.64806	0.57036	0.44744	0.33413	0.47692	0.40645	0.41888	0.33203	0.52576	0.41626	0.44726	0.52059	0.46822	0.28827	0.58872	0.56202
kap1	99.9851	129.449	245.413	270.69	133.156	156.248	107.603	144.855	248.306	303.07	224.111	268.281	212.102	278.686	161.319	225.083	237.768	192.886	240.527	334.737	143.342	150.865
lkap1	1.40397	1.78641	3.3188	3.59771	1.99767	2.28968	1.64415	2.13284	3.19609	3.91333	2.95885	3.46442	2.99682	3.74742	2.34861	3.12894	3.13948	2.61558	3.08606	4.26698	2.06319	2.1983
frac2	0.19702	0.1883	0.20211	0.20345	0.22229	0.23591	0.23646	0.23209	0.18623	0.14264	0.17963	0.15269	0.21486	0.20672	0.22115	0.2071	0.20692	0.2239	0.21674	0.18807	0.22395	0.23754
hei2	0.81829	0.85524	0.80299	0.88016	0.73728	0.81525	0.70438	0.81344	0.71475	0.87343	0.73165	0.80112	0.68869	0.84721	0.65275	0.82794	0.57426	0.58937	0.52532	0.7347	0.61264	0.74954
kap2	54.6843	36.6555	25.0952	80.4879	45.3421	95.8522	49.567	107.378	27.0171	94.8323	70.0307	113.308	44.2512	125.875	50.2474	183.416	164.976	215.186	103.092	148.677	78.5122
lkap2	0.79903	0.57392	0.88731	0.42072	1.20439	0.73547	1.40617	0.77436	1.46125	0.44687	1.3187	0.95638	1.57471	0.64942	1.75513	0.74625	2.38676	2.20186	2.74826	1.37832	2.03562	1.15074
frac3	0.51629	0.45849	0.5393	0.48781	0.51233	0.47094	0.5084	0.47563	0.64599	0.62265	0.66727	0.66005	0.53725	0.48776	0.54962	0.51939	0.58601	0.55863	0.5793	0.53819	0.55511	0.50428
hei3	0.00256	0.00256	0.00256	0.00256	0.00256	0.00256	0.00256	0.00256	0.00256	0.00256	0.00256	0.00256	0.00256	0.00256	0.00256	0.00256	0.00256	0.00256	0.00256	0.00256	0.00256	0.00256
kap3	250	250	250	250	250	250	2.50E+02	250	250	250	250	250	250	250	250	250	250	250	250	250	250	250
lkap3	5.52146	5.52146	5.52146	5.52146	5.52146	5.52146	5.52146	5.52146	5.52146	5.52146	5.52146	5.52146	5.52146	5.52146	5.52146	5.52146	5.52146	5.52146	5.52146	5.52146	5.52146	5.52146
dear	3.56E-10	3.26E-10	5.88E-10	6.05E-10	6.25E-10	9.38E-10	6.02E-10	7.85E-10	1.88E-09	1.69E-09	1.72E-09	1.77E-09	3.33E-10	3.99E-10	3.59E-10	4.59E-10	8.30E-10	9.70E-10	6.88E-10	7.26E-10	6.34E-10	8.28E-10
frear	0.22321	0.20549	0.42563	0.59063	0.45701	0.65975	0.45156	0.6379	0.84561	0.76503	0.80209	0.83056	0.54764	0.67101	0.37639	0.57595	0.88507	0.95848	0.76751	0.87961	0.57106	0.7574
fr0	0.78952	0.79525	0.69379	0.69723	0.66078	0.63116	0.64116	0.62096	0.71791	0.77563	0.69511	0.79309	0.62932	0.66038	0.65134	0.63499	0.66492	0.62613	0.70728	0.67498	0.6482	0.6157
fr1	0.34901	0.34524	0.37711	0.3448	0.45756	0.44763	0.48155	0.4666	0.4497	0.34508	0.50262	0.3571	0.43971	0.38929	0.44181	0.44541	0.48333	0.45709	0.42355	0.4061	0.47074	0.46881
fv0	0.41534	0.51435	0.4298	0.51053	0.42823	0.49662	0.44082	0.50356	0.24609	0.24221	0.20189	0.15492	0.38279	0.43157	0.26484	0.3326	0.22166	0.32534	0.17327	0.23671	0.31267	0.40068
fv1	0.56336	0.60695	0.58405	0.64091	0.55457	0.62	0.52612	0.57623	0.42286	0.51026	0.34922	0.39126	0.50544	0.57354	0.43486	0.49559	0.3757	0.43335	0.35446	0.34467	0.4619	0.52979
fvtot	0.37012	0.45958	0.4098	0.48591	0.39308	0.46482	4.02E-01	0.46676	0.23561	0.22767	0.18588	0.14346	0.36796	0.41822	0.24641	0.32237	0.2021	0.30649	0.14984	0.21774	0.29257	0.37379
MSE	26923.2	23395.4	18916.9	17384.9	30716.9	26453.8	3.41E+04	24791.8	31574.7	20956.4	33652	21788	23376.8	20507.6	26967.4	24557.6	17523.7	16238.3	16230.7	13439.2	32538.9	25482
ra0	4.10E-06	4.00E-06	4.74E-06	4.86E-06	4.76E-06	4.82E-06	4.90E-06	4.88E-06	4.79E-06	4.54E-06	5.19E-06	4.92E-06	5.05E-06	5.27E-06	5.50E-06	5.54E-06	5.26E-06	5.54E-06	5.20E-06	5.17E-06	5.20E-06	5.13E-06
ra1	4.88E-06	4.18E-06	4.69E-06	4.16E-06	5.49E-06	5.19E-06	5.57E-06	5.26E-06	5.69E-06	4.24E-06	5.55E-06	4.43E-06	5.54E-06	5.29E-06	5.22E-06	5.33E-06	5.89E-06	5.90E-06	5.90E-06	5.79E-06	5.75E-06	5.65E-06

Fig C.1: *Means of all metrics in all regions (part 1).*

	LeftHippocampus		Left Putamen		Idle Cerebellar Pedu		pCcipitopontineTract		pCcipitopontineTract		Right Insula		Right Amygdala		htCerebralWhiteMat		Right Hippocampus		Right Putamen		erioCerebellarPedur	
	T0	T1	T0	T1	T0	T1	T0	T1	T0	T1	T0	T1	T0	T1	T0	T1	T0	T1	T0	T1	T0	T1
FA	0.36139	0.37012	0.46846	0.47307	0.57627	0.65101	0.61542	0.67239	0.61198	0.65313	0.24635	0.26237	0.31694	0.33868	0.43649	0.46462	0.37866	0.36663	0.46495	0.4971	0.57256	0.6217
MD	0.00139	0.00148	0.00115	0.00115	0.00091	0.00094	0.00114	0.00118	0.00114	0.00121	0.00148	0.00151	0.00148	0.00142	0.00136	0.00139	0.00135	0.00141	0.00113	0.00113	0.00098	0.00106
AD	0.00194	0.00212	0.0018	0.00182	0.00158	0.00178	0.00207	0.0023	0.00203	0.00224	0.00185	0.00192	0.00198	0.00196	0.00201	0.00211	0.0019	0.00199	0.00176	0.00181	0.00168	0.00194
RD	0.00112	0.00117	0.00083	0.00082	0.00058	0.00051	0.00067	0.00062	0.0007	0.00069	0.00129	0.00131	0.00123	0.00116	0.00103	0.00103	0.00107	0.00111	0.00082	0.00078	0.00063	0.00061
MK	0.68676	0.65247	0.81375	0.81357	1.02464	1.06589	0.90539	0.90179	0.90571	0.91274	0.62621	0.62457	0.63438	0.66229	0.75123	0.77104	0.71522	0.6879	0.8201	0.8422	0.97525	0.96266
AK	0.51568	0.48372	0.55689	0.56083	0.64097	0.59995	0.50716	0.46942	0.51338	0.47843	0.52206	0.51236	0.49794	0.51045	0.50918	0.50113	0.52901	0.51452	0.5645	0.5681	0.62601	0.57934
RK	0.81741	0.78408	1.03143	1.02947	1.37466	1.51124	1.29665	1.36337	1.27798	1.37077	0.69551	0.70032	0.72533	0.77058	0.96115	1.02391	0.85835	0.82281	1.02487	1.05998	1.25921	1.30071
KFA	0.31196	0.32007	0.40894	0.41811	0.50132	0.54703	0.51184	0.55159	0.50819	0.53593	0.22392	0.23737	0.27723	0.29924	0.37107	0.3916	0.32536	0.3189	0.4076	0.43718	0.50048	0.52252
MSD	0.00111	0.00113	0.00079	0.00075	0.00073	0.00069	0.00085	0.00084	0.00085	0.00087	0.00102	0.00111	0.00106	0.00099	0.001	0.00102	0.00107	0.00107	0.00076	0.00075	0.00084	0.00086
MKT	0.66784	0.63136	0.77472	0.77621	0.9743	0.97092	0.81795	0.8	0.8273	0.8073	0.61913	0.61588	0.62339	0.64722	0.71282	0.71988	0.69301	0.66806	0.78703	0.80482	0.94431	0.89881
MSK	0.658	0.62459	0.7829	0.79134	0.92577	0.99694	0.84022	0.8533	0.85081	0.8543	0.62055	0.60839	0.64105	0.64577	0.72282	0.7397	0.68385	0.66741	0.78719	0.82359	0.86021	0.90569
AWF	0.41815	0.40059	0.41675	0.44055	0.50447	0.54134	0.46823	0.47166	0.45821	0.48865	nan	0.40307	nan	0.33728	0.46299	0.47516	0.40643	0.40188	0.3952	0.41192	0.49572	0.52181
TORT	5.31871	4.98276	4.87091	6.27761	2.2E-07	5.2E-07	5.94777	10.1731	5.38488	7.11939	nan	4.33111	nan	4.77601	6.9E-07	1.8E-08	4.48328	5.06192	4.64784	5.27901	6.69579	58.3177
ficvf	0.4817	0.48955	0.52998	0.56002	0.7485	0.77379	0.61921	0.6268	0.64327	0.65034	0.40108	0.44573	0.41212	0.47996	0.51439	0.56329	0.51023	0.50564	0.55811	0.58203	0.75903	0.74884
fiso	0.29489	0.39972	0.09428	0.09186	0.18902	0.15506	0.17919	0.17831	0.19783	0.20457	0.19727	0.32694	0.22402	0.30766	0.22471	0.25184	0.27812	0.34713	0.11914	0.10367	0.27979	0.25162
odi	0.47723	0.46346	0.4168	0.44154	0.36894	0.32403	0.30451	0.26621	0.30796	0.28015	0.58646	0.578	0.49691	0.49477	0.42271	0.42422	0.46275	0.47852	0.41821	0.42346	0.35772	0.32654
fd	0.00194	0.00155	0.00187	0.00145	0.00221	0.00218	0.00243	0.00243	0.00238	0.00238	0.00123	0.00118	0.00173	0.00137	0.00202	0.00189	0.00207	0.00149	0.00184	0.0016	0.00235	0.00216
mose	1.97425	1.95836	1.98952	1.97037	1.93331	1.96968	1.90153	1.95466	1.92804	1.9549	1.97002	1.9906	1.92492	1.98113	1.89906	1.95822	1.94986	1.99208	1.97803	1.97927	1.90721	1.91369
frac1	0.19646	0.22003	0.27802	0.31246	0.30274	0.34395	0.27276	0.28612	0.25811	0.28602	0.21037	0.22375	0.20936	0.24653	0.24933	0.28544	0.19936	0.21305	0.29351	0.2954	0.27867	0.31297
hei1	0.36339	0.35742	0.44881	0.40806	0.49589	0.48714	0.58308	0.56151	0.64993	0.59307	0.55965	0.45425	0.42221	0.32801	0.62948	0.55575	0.36904	0.26547	0.39064	0.34503	0.46477	0.4366
kap1	286.921	288.193	207.26	245.247	175.193	192.8	145.569	147.467	114.96	139.23	180.772	231.125	269.992	314.687	125.632	155.473	280.906	338.337	244.15	282.729	202.048	227.476
lkap1	3.71231	3.74454	2.90094	3.30913	2.53822	2.70294	2.10064	2.17638	1.69915	2.0309	2.42411	3.06057	3.42479	3.99599	1.82498	2.24925	3.65773	4.34959	3.32886	3.74353	2.81476	3.08646
frac2	0.18945	0.17299	0.22764	0.21975	0.2296	0.221	0.22712	0.2357	0.25781	0.24242	0.22135	0.20567	0.19612	0.20205	0.2404	0.23934	0.19123	0.17008	0.23635	0.22125	0.22503	0.22159
hei2	0.66714	0.80253	0.69376	0.7508	0.72622	0.85458	0.65341	0.76404	0.67956	0.79244	0.51248	0.68175	0.57931	0.70537	0.60488	0.76861	0.67284	0.82755	0.67502	0.74616	0.69222	0.82827
kap2	138.809	68.4988	114.028	85.3055	90.8934	36.1788	128.598	64.5233	53.3238	216.992	127.959	189.273	118.382	152.072	70.9666	130.115	56.7844	124.741	92.2128	107.46	52.2171
lkap2	1.81672	0.94216	1.56345	1.19626	1.30695	0.56782	1.77602	1.004	1.57452	0.8475	2.801	1.68847	2.41368	1.56105	2.08085	1.04498	1.73622	0.79087	1.69534	1.26783	1.5223	0.75435
frac3	0.61962	0.61718	0.49697	0.4767	0.49592	0.44207	0.52265	0.49061	0.50292	0.48415	0.57725	0.57716	0.61042	0.5603	0.53855	0.49867	0.62043	0.62274	0.47603	0.48908	0.53245	0.48667
hei3	0.00256	0.00256	0.00256	0.00256	0.00256	0.00256	0.00256	0.00256	0.00256	0.00256	0.00256	0.00256	0.00256	0.00256	0.00256	0.00256	0.00256	0.00256	0.00256	0.00256	0.00256	0.00256
kap3	250	250	250	250	250	250	250	250	250	250	250	250	250	250	250	250	250	250	250	250	250	250
lkap3	5.52146	5.52146	5.52146	5.52146	5.52146	5.52146	5.52146	5.52146	5.52146	5.52146	5.52146	5.52146	5.52146	5.52146	5.52146	5.52146	5.52146	5.52146	5.52146	5.52146	5.52146	5.52146
drear	6.74E-10	8.09E-10	4.33E-10	4.72E-10	3.50E-10	3.78E-10	3.70E-10	4.64E-10	4.62E-10	5.60E-10	7.54E-10	8.87E-10	6.18E-10	7.02E-10	6.71E-10	8.03E-10	5.46E-10	7.25E-10	4.17E-10	4.33E-10	4.36E-10	5.52E-10
frear	0.6066	0.81146	0.6442	0.843	0.53203	0.64579	0.35215	0.48484	0.43397	0.51812	0.8906	0.94358	0.66768	0.83038	0.60234	0.75317	0.47776	0.7976	0.62621	0.79794	0.43453	0.62302
fr0	0.69767	0.7256	0.62672	0.60554	0.6187	0.61621	0.62473	0.61743	0.6099	0.61202	0.66026	0.65689	0.7486	0.70665	0.64141	0.61571	0.69616	0.70351	0.61225	0.62744	0.65265	0.6479
fr1	0.43108	0.41587	0.43858	0.43593	0.43625	0.41611	0.47928	0.47831	0.46419	0.484	0.46609	0.43456	0.38212	0.42955	0.46879	0.46539	0.47202	0.43724	0.45692	0.40993	0.4599	0.41631
fv0	0.21707	0.21324	0.33185	0.3565	0.39352	0.46446	0.35559	0.40686	0.33697	0.33686	0.20319	0.27783	0.13432	0.16235	0.31297	0.38903	0.19027	0.19173	0.27557	0.34364	0.33192	0.39234
fv1	0.38316	0.35794	0.46354	0.48855	0.58763	0.63283	0.51448	0.55248	0.49429	0.49741	0.39383	0.42324	0.34232	0.35014	0.45398	0.50662	0.36542	0.37254	0.4556	0.45745	0.50448	0.56066
fvtot	0.20415	0.19543	0.30995	0.33821	0.37608	0.44558	0.33736	0.3878	0.33222	0.32408	0.18811	0.25879	0.12021	0.14808	0.28988	0.36364	0.17799	0.17666	0.24326	0.32753	0.31344	0.37275
MSE	19737.6	13866.4	20527.1	20304.5	24105.9	23945.1	34333	35844.9	46732.5	47493.4	162577	137028	133145	110009	35508.5	25787.5	19501.2	12795.8	15645	19947.9	24245.2	22301.3
ra0	5.43E-06	5.37E-06	5.37E-06	5.57E-06	5.20E-06	5.14E-06	5.12E-06	5.26E-06	5.45E-06	5.24E-06	5.50E-06	5.47E-06	5.50E-06	5.14E-06	5.29E-06	5.17E-06	5.42E-06	5.26E-06	5.36E-06	5.51E-06	5.03E-06	5.02E-06
ra1	5.60E-06	5.31E-06	5.87E-06	5.84E-06	5.21E-06	4.88E-06	5.58E-06	5.45E-06	5.30E-06	5.90E-06	5.84E-06	5.67E-06	5.63E-06	5.77E-06	5.59E-06	5.54E-06	5.18E-06	5.85E-06	5.59E-06	5.29E-06	4.92E-06	

Fig C.2: *Means of all metrics in all regions (part 2).*

	CC		Brain Stem		CorticospinalTractL		CorticospinalTractR		FornixL		FornixR		riorCerebellarPedunL		riorCerebellarPedunR		LeftInsula		Left Amygdala		t cerebral white Mat	
	T0	T1	T0	T1	T0	T1	T0	T1	T0	T1	T0	T1	T0	T1	T0	T1	T0	T1	T0	T1	T0	T1
FA	0.16276	0.14561	0.19841	0.20234	0.24472	0.2777	0.23309	0.25991	0.18216	0.2302	0.15001	0.19252	0.1516	0.19641	0.14542	0.17262	0.10806	0.12017	0.1177	0.14869	0.20733	0.24608
MD	0.00021	0.0002	0.00019	0.0002	0.00049	0.00072	0.00044	0.00054	0.00029	0.00044	0.00023	0.00092	0.00021	0.00014	0.00024	0.00021	0.00024	0.00031	0.00014	0.00017	0.00038	0.00062
AD	0.00064	0.00075	0.00051	0.00054	0.00054	0.00069	0.0005	0.00057	0.00048	0.00055	0.00047	0.00056	0.00039	0.00041	0.00037	0.00039	0.00033	0.00035	0.00026	0.00035	0.00048	0.00068
RD	0.00028	0.00026	0.00025	0.00028	0.00061	0.00085	0.00055	0.00067	0.00036	0.00057	0.00028	0.00039	0.00021	0.00023	0.00024	0.00026	0.00033	0.00033	0.00019	0.00023	0.00046	0.00072
MK	0.19741	0.21931	0.1672	0.22351	0.26096	0.31047	0.23802	0.28717	0.14119	0.2192	0.09917	0.14637	0.16378	0.15229	0.14767	0.16713	0.08623	0.09149	0.05254	0.06291	0.17359	0.22535
AK	0.09055	0.10164	0.13028	0.1388	0.11734	0.14019	0.11307	0.15046	0.08619	0.10272	0.07758	0.09558	0.16037	0.10656	0.13089	0.10861	0.07106	0.06603	0.0487	0.06073	0.09511	0.12477
RK	0.52317	0.63764	0.42539	0.53899	0.53221	0.60995	0.46346	0.55418	0.30115	0.47899	0.20811	0.2948	0.28548	0.35379	0.27199	0.34081	0.12259	0.14479	0.10296	0.13193	0.35355	0.45352
KFA	0.12644	0.11326	0.15292	0.15617	0.19619	0.22368	0.18706	0.20773	0.14551	0.18557	0.11934	0.15307	0.15152	0.14935	0.15763	0.13492	0.08672	0.09896	0.09412	0.11834	0.16423	0.19595
MSD	0.00033	0.00029	0.00039	0.00041	0.00044	0.00068	0.00043	0.00056	0.00064	0.00075	0.00061	0.00066	0.00021	0.00016	0.00028	0.00031	0.00029	0.0005	0.00022	0.00037	0.00035	0.00056
MKT	0.11601	0.11198	0.12681	0.15308	0.19692	0.23905	0.18804	0.23041	0.11426	0.16526	0.0834	0.11844	0.16736	0.10503	0.18491	0.1327	0.08164	0.08347	0.04565	0.05312	0.14085	0.1875
MSK	0.21982	0.21689	0.18259	0.20823	0.21807	0.2686	0.19784	0.24783	0.14512	0.19835	0.13707	0.14375	0.15473	0.12146	0.1691	0.16442	0.07918	0.1023	0.05504	0.09102	0.1483	0.24067
AWF	0.11507	0.109	0.07529	0.09065	0.08071	0.08295	0.08536	0.09669	0.06445	0.10103	0.05428	0.11201	0.03082	0.05792	0.03875	0.04087	0	0.0332	nan	0.01504	0.08227	0.08383
TORT	3.6E-09	4.4E-09	3.06234	4.9E-08	6.42418	3.8E-08	8.64101	5.2E-08	1.44539	18.033	1.08071	2.88744	0.61161	2.31317	3.85546	0.60758	0	0.95333	nan	0.36626	1.5E-09	1.6E-09
ficvf	0.15892	0.13617	0.13575	0.14877	0.18595	0.20003	0.19478	0.20059	0.20407	0.22375	0.18732	0.2013	0.15992	0.12249	0.17186	0.14	0.08096	0.1138	0.06559	0.08445	0.14733	0.18673
fiso	0.22014	0.18968	0.22092	0.23309	0.19362	0.2707	0.19323	0.24261	0.27809	0.27845	0.26449	0.24693	0.13532	0.11203	0.17378	0.1864	0.21356	0.30517	0.19743	0.29803	0.19616	0.2682
odi	0.09344	0.09434	0.16405	0.15723	0.1741	0.20866	0.17111	0.20509	0.17847	0.20211	0.15948	0.17823	0.16035	0.16509	0.15584	0.13524	0.19238	0.19325	0.1847	0.19523	0.19194	0.22103
fd	0.00052	0.00042	0.00063	0.00083	0.00063	0.00076	0.00065	0.00079	0.00051	0.00058	0.00051	0.00064	0.00084	0.00096	0.00064	0.00085	0.00074	0.00071	0.00089	0.00091	0.00078	0.00087
mose	0.489	0.49679	0.33405	0.24154	0.3468	0.18277	0.35148	0.18278	0.40157	0.41072	0.42447	0.37893	0.14448	0	0.12564	0.04142	0.16722	0.05908	0.22335	0.1082	0.30512	0.20388
frac1	0.1822	0.1871	0.11347	0.12807	0.14877	0.15128	0.16972	0.15229	0.07013	0.14507	0.08051	0.10704	0.12875	0.10623	0.10079	0.10802	0.08731	0.09135	0.0828	0.10526	0.11226	0.14429
hei1	0.38927	0.41273	0.45065	0.44675	0.43592	0.44661	0.41667	0.44261	0.46363	0.44427	0.46416	0.46033	0.44363	0.43769	0.44523	0.45162	0.46241	0.45748	0.46511	0.43024	0.43931	0.44272
kap1	197.131	216.226	246.002	245.517	215.249	225.626	200.075	221.314	248.636	242.02	245.679	246.99	242.183	243.676	228.958	243.738	246.595	239.763	248.382	232.874	221.471	223.903
kap1	2.44274	2.65578	2.92543	2.91761	2.65531	2.7673	2.4983	2.71928	3.01818	2.90265	2.98583	2.99689	2.86266	2.86346	2.77055	2.89745	2.98643	2.92039	3.02813	2.81085	2.72071	2.74967
frac2	0.08426	0.08751	0.0636	0.07162	0.10492	0.11422	0.1085	0.10641	0.07594	0.06257	0.07402	0.06498	0.07828	0.0779	0.06849	0.0828	0.07599	0.0929	0.09061	0.07045	0.08901	0.1088
hei2	0.30474	0.25707	0.32106	0.21629	0.37016	0.29888	0.39303	0.30594	0.39263	0.22699	0.38067	0.32755	0.40722	0.27262	0.42046	0.29499	0.45105	0.4416	0.4627	0.3832	0.43653	0.36135
kap2	153.132	126.342	179.313	138.94	192.694	145.358	203.056	110.128	193.265	171.522	206.373	139.424	213.828	147.135	239.026	232.434	246.455	200.493	225.347	178.292		
kap2	1.91	1.60268	2.00484	1.33624	2.25647	1.77752	2.4063	1.84299	2.50735	1.37618	2.39234	2.11537	2.55105	1.7329	2.63331	1.8447	2.93079	2.84579	3.01678	2.47025	2.76837	2.22775
frac3	0.14551	0.14006	0.11402	0.1258	0.12299	0.10029	0.13137	0.10667	0.10959	0.1344	0.11032	0.11905	0.09168	0.0955	0.09043	0.10924	0.09921	0.09506	0.10787	0.0932	0.10166	0.09562
hei3	0	0	0	0	0	0	0	0	0	0	0	0	0	0	0	0	0	0	0	0	0	0
kap3	0	0	0	0	0	0	0	0	0	0	0	0	0	0	0	0	0	0	0	0	0	0
kap3	0	0	0	0	0	0	0	0	0	0	0	0	0	0	0	0	0	0	0	0	0	0
dear	3.51E-10	3.34E-10	6.70E-10	6.73E-10	6.23E-10	9.12E-10	6.00E-10	7.73E-10	9.22E-10	1.05E-09	9.36E-10	1.01E-09	9.98E-11	1.82E-10	2.90E-10	4.17E-10	3.46E-10	5.40E-10	2.96E-10	4.41E-10	5.02E-10	7.12E-10
frear	0.24589	0.21508	0.37223	0.39227	0.37244	0.38187	0.37098	0.39087	0.3367	0.38155	0.36818	0.3418	0.38066	0.37661	0.2859	0.37321	0.27878	0.37537	0.35709	0.27415	0.39397	0.3568
fr0	0.15627	0.16497	0.1744	0.17521	0.19497	0.19652	0.20321	0.20964	0.21133	0.17733	0.2622	0.196	0.16708	0.18203	0.17654	0.19562	0.18621	0.17919	0.17246	0.18924	0.19068	0.203
fr1	0.191	0.22658	0.17049	0.17677	0.18437	0.18907	0.18642	0.20059	0.17056	0.20754	0.24982	0.26645	0.15357	0.19243	0.19029	0.21634	0.17732	0.16784	0.21251	0.22074	0.17687	0.18525
fv0	0.24098	0.24556	0.25578	0.25929	0.23422	0.23307	0.24028	0.22908	0.19594	0.21062	0.16933	0.1506	0.21903	0.22277	0.21105	0.23379	0.17189	0.19794	0.15874	0.17202	0.21241	0.23012
fv1	0.18912	0.2126	0.19719	0.20719	0.16938	0.16116	0.15379	0.16579	0.13869	0.23764	0.11974	0.21977	0.13743	0.16479	0.13485	0.17009	0.12067	0.1457	0.13422	0.13408	0.14251	0.14796
fvtot	0.21501	0.21948	0.25082	0.25798	0.22314	0.23495	0.21503	0.21677	0.18557	0.19732	0.1488	0.14249	0.21929	0.2274	0.20132	0.23008	0.1568	0.18981	0.13837	0.16469	0.20538	0.2257
MSE	14412.2	14231.7	9964.33	9313.86	18537.9	17844.7	22978.9	20699.5	15133.2	10939.9	15526.5	11083.9	14376	13745.5	18351.5	18322.8	10515.5	8923.85	9757.4	8908.35	23206.2	20503.9
ra0	1.97E-06	1.95E-06	1.87E-06	1.79E-06	1.87E-06	1.84E-06	1.79E-06	1.79E-06	1.90E-06	2.01E-06	1.62E-06	1.81E-06	1.81E-06	1.58E-06	1.32E-06	1.24E-06	1.65E-06	1.29E-06	1.68E-06	1.73E-06	1.65E-06	1.67E-06
ra1	1.96E-06	2.28E-06	1.98E-06	2.19E-06	1.24E-06	1.60E-06	1.12E-06	1.56E-06	1.04E-06	2.25E-06	1.33E-06	2.26E-06	1.30E-06	1.57E-06	1.75E-06	1.55E-06	2.73E-07	1.56E-08	8.47E-22	7.76E-07	8.46E-07	1.05E-06

Fig C.3: *Standard deviations of all metrics in all regions (part 1).*

	LeftHippocampus		Left Putamen		Idle Cerebellar Pedu		OccipitopontineTract		OccipitopontineTract		Right Insula		Right Amygdala		htCerebralWhiteMat		Right Hippocampus		Right Putamen		erIorCerebellarPedur	
	T0	T1	T0	T1	T0	T1	T0	T1	T0	T1	T0	T1	T0	T1	T0	T1	T0	T1	T0	T1	T0	T1
FA	0.12998	0.15928	0.17631	0.19055	0.20571	0.20731	0.19614	0.21513	0.19407	0.21769	0.1095	0.1193	0.10238	0.14396	0.21386	0.24567	0.1299	0.15448	0.15948	0.17787	0.17793	0.19053
MD	0.00015	0.00022	0.00015	0.00016	0.0002	0.00015	0.0002	0.00027	0.00027	0.00038	0.00021	0.00024	0.00012	0.00017	0.00046	0.00057	0.00016	0.0002	0.00015	0.00015	0.00024	0.00023
AD	0.00029	0.00048	0.00037	0.00047	0.00043	0.00047	0.00048	0.0006	0.00044	0.00055	0.00027	0.0003	0.00025	0.00037	0.00051	0.00062	0.00029	0.00041	0.00031	0.00044	0.00055	0.00065
RD	0.0002	0.00025	0.00022	0.00023	0.00026	0.00025	0.00029	0.00037	0.00035	0.00049	0.00023	0.00027	0.00016	0.00022	0.00053	0.00067	0.0002	0.00024	0.00021	0.00021	0.00026	0.00028
MK	0.07692	0.08501	0.1113	0.11084	0.17337	0.2015	0.17766	0.20345	0.19115	0.23175	0.08021	0.08952	0.04911	0.06557	0.18471	0.22898	0.08525	0.09278	0.10553	0.11651	0.1721	0.19648
AK	0.05773	0.0801	0.09048	0.10861	0.13538	0.11347	0.09617	0.10425	0.09438	0.10208	0.06284	0.06374	0.05065	0.0679	0.09663	0.12607	0.06167	0.08267	0.0832	0.10738	0.17988	0.13867
RK	0.15303	0.1834	0.25494	0.28413	0.4165	0.5142	0.4402	0.49279	0.42733	0.52931	0.12673	0.15036	0.08781	0.13035	0.35977	0.45189	0.17307	0.179	0.215	0.24928	0.36725	0.40726
KFA	0.10206	0.12194	0.13542	0.14469	0.1746	0.15812	0.15303	0.16933	0.154	0.17296	0.08792	0.09699	0.08207	0.11339	0.1702	0.19512	0.10329	0.11937	0.12376	0.1364	0.15626	0.14829
MSD	0.00031	0.00046	0.00015	0.00014	0.00022	0.00019	0.00019	0.00024	0.00026	0.00035	0.00025	0.00043	0.0002	0.00039	0.00041	0.00054	0.00028	0.00038	0.00016	0.00013	0.00036	0.00041
MKT	0.06447	0.07053	0.08994	0.09174	0.14968	0.11524	0.12552	0.14423	0.14512	0.16422	0.07412	0.07985	0.04428	0.05914	0.15279	0.19035	0.07178	0.08141	0.09114	0.10105	0.18554	0.15474
MSK	0.08778	0.10693	0.10011	0.11015	0.14912	0.14908	0.14188	0.17574	0.15075	0.1835	0.07451	0.10925	0.05052	0.09231	0.16228	0.30222	0.08552	0.10878	0.09616	0.11047	0.17892	0.20587
AWF	0.06353	0.08311	0.05086	0.08289	0.06642	0.08234	0.08995	0.08659	0.08943	0.09347	nan	0.02183	nan	0.01736	0.08875	0.09279	0.06656	0.06938	0.04009	0.06864	0.06785	0.09604
TORT	0.98543	1.1819	1.08983	5.02056	2.2E+08	1.1E+09	3.38276	28.4472	1.7411	4.51252	nan	0.6733	nan	0.62029	1.2E+09	2E+09	0.62003	2.03588	0.89213	1.71569	2.67544	556.994
ficvf	0.12815	0.12025	0.08454	0.10148	0.15802	0.14582	0.15797	0.17148	0.17056	0.18455	0.08724	0.11203	0.07807	0.10145	0.15768	0.19179	0.14262	0.12937	0.10422	0.11303	0.15453	0.14652
fiso	0.24559	0.29423	0.11281	0.11652	0.14898	0.12553	0.12873	0.13094	0.16035	0.17284	0.19383	0.28172	0.19474	0.28775	0.21676	0.25898	0.22248	0.27208	0.13274	0.09902	0.22319	0.24346
odi	0.17252	0.20131	0.16617	0.20148	0.16964	0.15412	0.14283	0.15153	0.14444	0.15826	0.18031	0.1916	0.15788	0.19183	0.19655	0.21899	0.15412	0.19118	0.16453	0.18875	0.16063	0.14961
fd	0.00081	0.0009	0.0009	0.001	0.00082	0.00093	0.00061	0.00074	0.0006	0.0007	0.0007	0.00065	0.00091	0.00093	0.00079	0.00086	0.00076	0.00087	0.00094	0.00102	0.00071	0.00091
mose	0.1584	0.19977	0.10182	0.16955	0.24949	0.17147	0.29795	0.20804	0.25841	0.20753	0.17053	0.09648	0.26351	0.13606	0.30125	0.20008	0.21823	0.08864	0.1466	0.14249	0.29014	0.28082
frac1	0.07236	0.0944	0.11131	0.11723	0.13466	0.12483	0.12021	0.13062	0.11936	0.12959	0.08211	0.09714	0.06685	0.08786	0.12498	0.14135	0.07334	0.09205	0.112	0.11172	0.14894	0.14026
hei1	0.45124	0.45031	0.45323	0.45616	0.44849	0.45562	0.44128	0.43943	0.41858	0.43565	0.45501	0.46156	0.46427	0.44301	0.42694	0.4452	0.45275	0.41745	0.449	0.44406	0.45372	0.45688
kap1	244.725	244.123	241.744	245.475	233.306	238.652	222.184	221.897	205.37	218.398	237.107	246.541	248.143	240.137	212.37	226.094	245.489	231.39	245.568	244.048	241.073	244.695
lkap1	2.9483	2.93529	2.88663	2.94086	2.81114	2.87986	2.73238	2.73143	2.55877	2.7036	2.90461	2.97587	3.0313	2.90885	2.62623	2.77005	2.94727	2.74837	2.91067	2.89805	2.88906	2.93862
frac2	0.06859	0.0682	0.08988	0.09558	0.08293	0.08675	0.08962	0.10825	0.10688	0.10985	0.08468	0.08295	0.06784	0.08436	0.10029	0.11086	0.06823	0.06301	0.0993	0.08599	0.08694	0.08459
hei2	0.42143	0.3258	0.40339	0.36518	0.38003	0.2573	0.42081	0.34406	0.40614	0.32052	0.46345	0.41238	0.45373	0.39937	0.43884	0.34701	0.41649	0.29895	0.41402	0.37219	0.40207	0.2945
kap2	222.281	170.02	207.123	185.656	189.165	125.895	215.467	163.275	204.097	150.02	245.955	216.974	241.627	211.317	226.847	171.034	217.241	156.734	213.681	191.463	201.839	150.396
lkap2	2.73254	2.09607	2.55721	2.2951	2.35817	1.58815	2.65494	2.06196	2.52734	1.90236	3.00863	2.65593	2.9615	2.5915	2.78355	2.1384	2.67327	1.93123	2.63663	2.36995	2.5053	1.86682
frac3	0.10052	0.1055	0.08545	0.08536	0.09646	0.08887	0.09079	0.08408	0.10165	0.08053	0.10681	0.11659	0.09615	0.10216	0.11654	0.10548	0.10654	0.11384	0.10602	0.09625	0.12896	0.12988
hei3	0	0	0	0	0	0	0	0	0	0	0	0	0	0	0	0	0	0	0	0	0	0
kap3	0	0	0	0	0	0	0	0	0	0	0	0	0	0	0	0	0	0	0	0	0	0
lkap3	0	0	0	0	0	0	0	0	0	0	0	0	0	0	0	0	0	0	0	0	0	0
dear	4.84E-10	5.60E-10	1.65E-10	1.50E-10	2.18E-10	2.52E-10	2.61E-10	3.79E-10	4.06E-10	5.49E-10	2.87E-10	4.71E-10	2.90E-10	4.88E-10	5.57E-10	6.83E-10	4.22E-10	4.72E-10	1.45E-10	1.22E-10	4.43E-10	5.94E-10
frear	0.41191	0.34917	0.35782	0.28743	0.33886	0.33572	0.27982	0.35959	0.31063	0.34498	0.26874	0.20212	0.3982	0.32152	0.38842	0.35683	0.39807	0.35306	0.33747	0.31559	0.35093	0.37706
fr0	0.18553	0.18451	0.19635	0.16034	0.1752	0.18992	0.20079	0.18112	0.20303	0.19257	0.20251	0.15383	0.18152	0.20871	0.20013	0.20142	0.17737	0.19002	0.18836	0.19556
fr1	0.17994	0.22855	0.20779	0.21652	0.1648	0.1957	0.18038	0.19705	0.18113	0.22226	0.20933	0.21157	0.20398	0.23599	0.19163	0.20174	0.19426	0.21536	0.21854	0.21093	0.17859	0.20458
fv0	0.1802	0.17945	0.21276	0.21659	0.27152	0.26751	0.2408	0.24503	0.23313	0.23699	0.18103	0.21313	0.13248	0.1511	0.22172	0.23064	0.16925	0.17683	0.22754	0.2132	0.24994	0.2553
fv1	0.12912	0.14381	0.13927	0.15186	0.17402	0.16686	0.16075	0.16698	0.15927	0.16888	0.13747	0.15373	0.13711	0.13302	0.14521	0.15027	0.11229	0.15052	0.14862	0.14635	0.17039	0.18583
fvtot	0.16993	0.16412	0.21096	0.21959	0.27205	0.27107	0.23652	0.24034	0.22991	0.23181	0.17169	0.2026	0.11799	0.145	0.20936	0.22288	0.15928	0.16171	0.21334	0.21138	0.2444	0.25398
MSE	11956.1	9081.31	15497.2	16649.7	17618.5	17561.7	19476	24879.9	30160.2	35456.5	11965.9	8640.94	9150.5	7528.67	25766.2	22717.3	12962.5	8598.97	13942.3	15001.4	14757.1	14477.3
ra0	1.44E-06	1.47E-06	1.53E-06	1.22E-06	1.59E-06	1.62E-06	1.70E-06	1.54E-06	1.33E-06	1.60E-06	1.34E-06	1.41E-06	1.33E-06	1.78E-06	1.55E-06	1.66E-06	1.46E-06	1.67E-06	1.54E-06	1.32E-06	1.80E-06	1.80E-06
ra1	1.22E-06	1.65E-06	3.84E-07	5.07E-07	1.52E-06	1.83E-06	1.13E-06	1.32E-06	1.20E-06	1.56E-06	8.47E-22	5.48E-07	1.09E-06	1.18E-06	7.86E-07	1.19E-06	1.34E-06	1.80E-06	5.01E-07	1.25E-06	1.62E-06	1.92E-06

Fig C.4: *Standard deviations of all metrics in all regions (part 2).*

Appendix D

Supplementary figures

D.1 Movement correction graphs

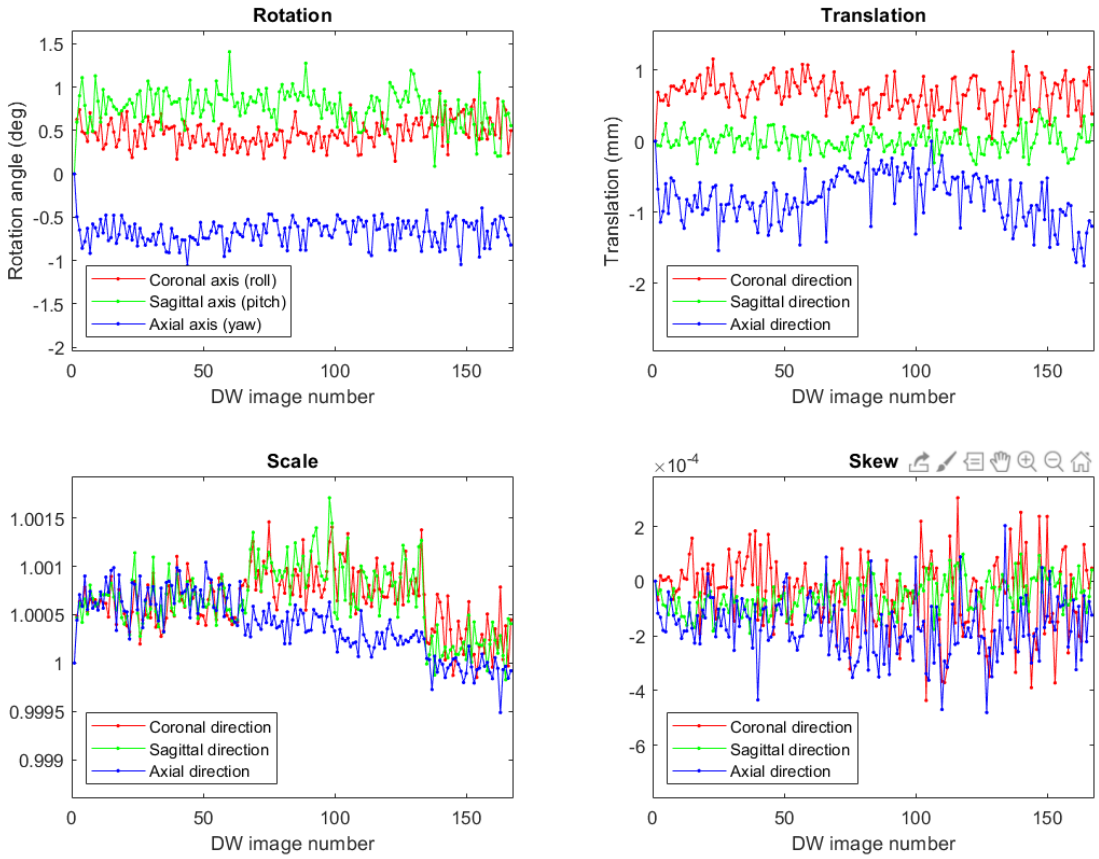

Fig D.1: *Motion correction of T0.*

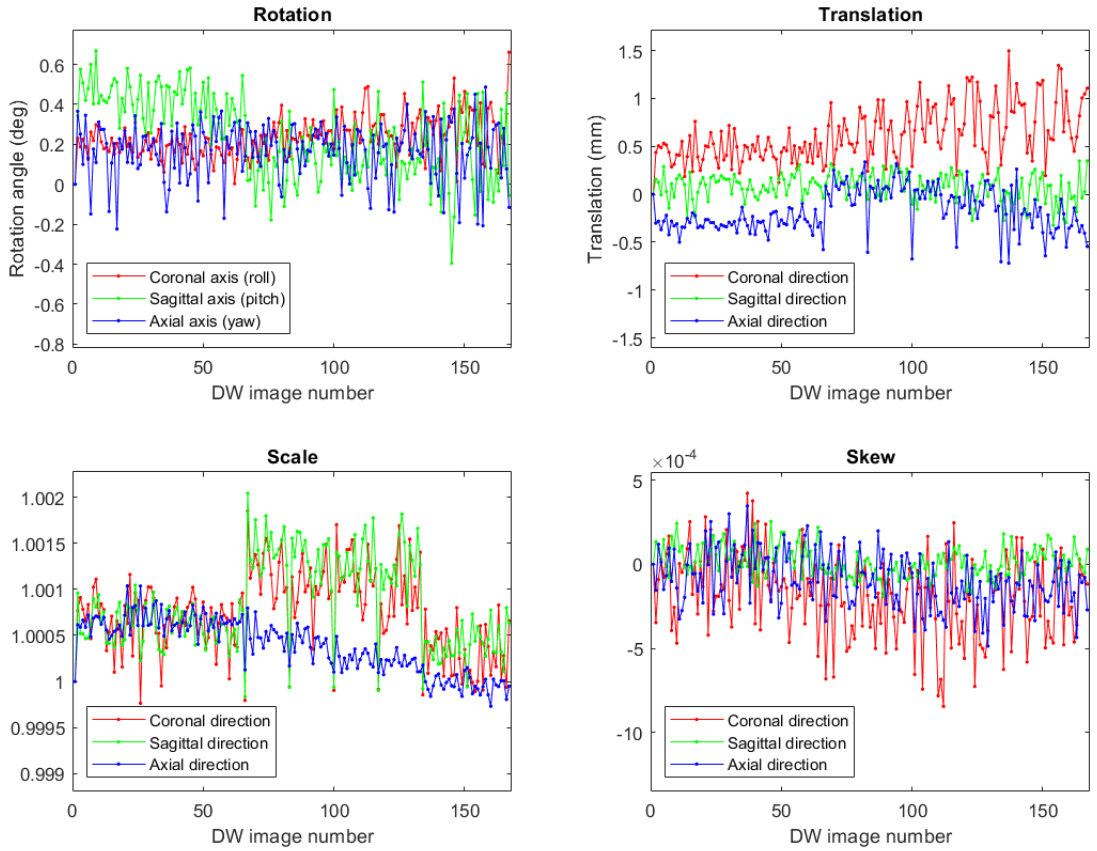

Fig D.2: *Motion correction of T1.*

D.2 Visual comparisons

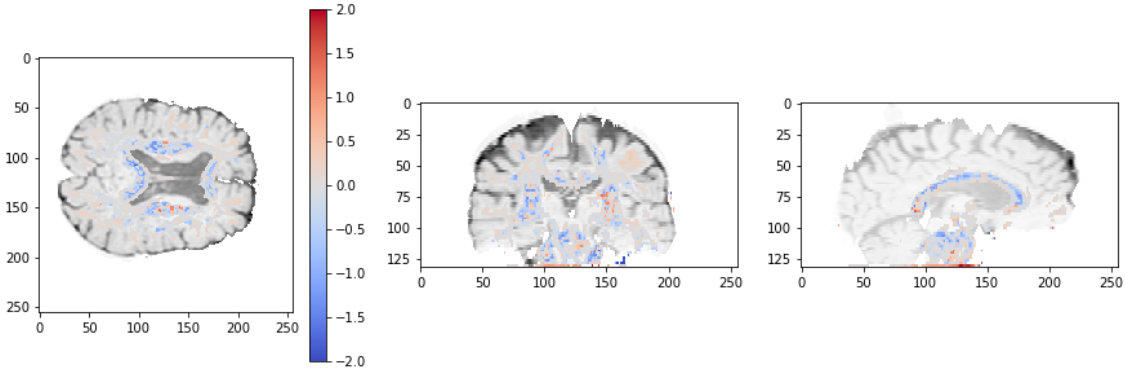

Fig D.3: *Difference in MK values in the white matter before and after abstinence, superimposed on a b0 scan. Axial view (Left), coronal view (Middle) and sagittal view (Right). Red pixels correspond to an increase and blue pixels to a decrease after abstinence.*

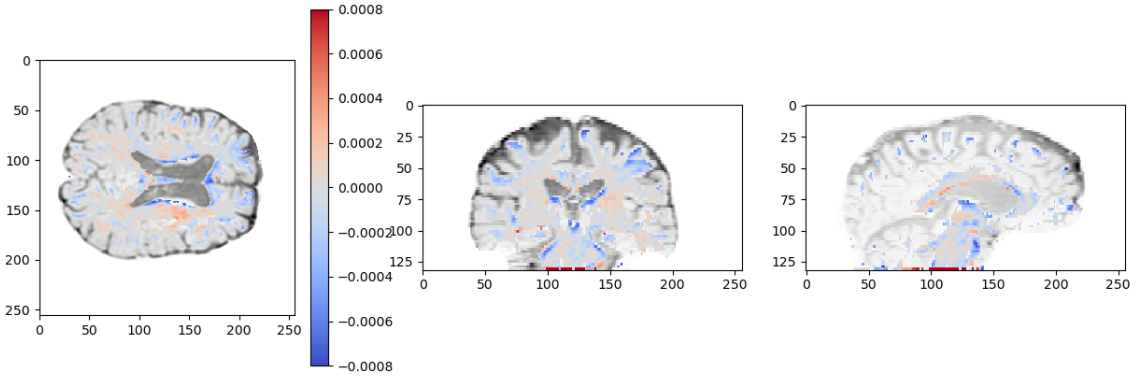

Fig D.4: *Difference in MSD values in the white matter before and after abstinence, superimposed on a b0 scan. Axial view (Left), coronal view (Middle) and sagittal view (Right). Red pixels correspond to an increase and blue pixels to a decrease after abstinence.*

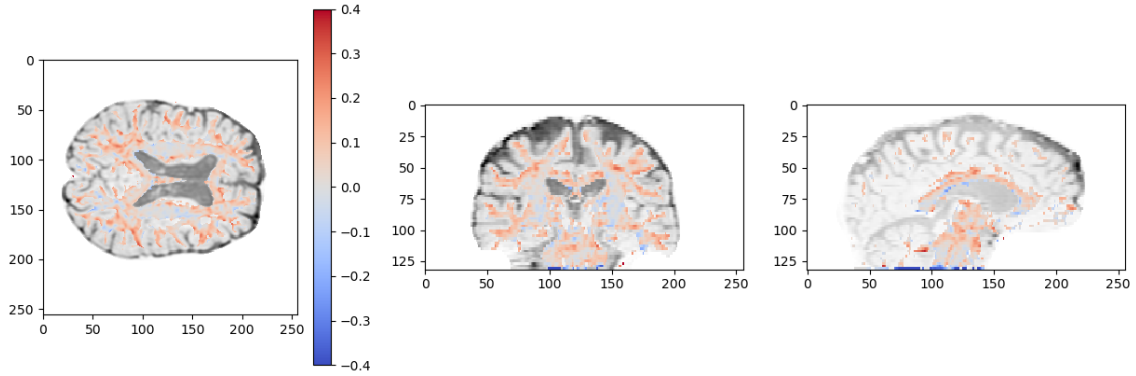

Fig D.5: *Difference in KFA values in the white matter before and after abstinence, superimposed on a b0 scan. Axial view (Left), coronal view (Middle) and sagittal view (Right). Red pixels correspond to an increase and blue pixels to a decrease after abstinence.*

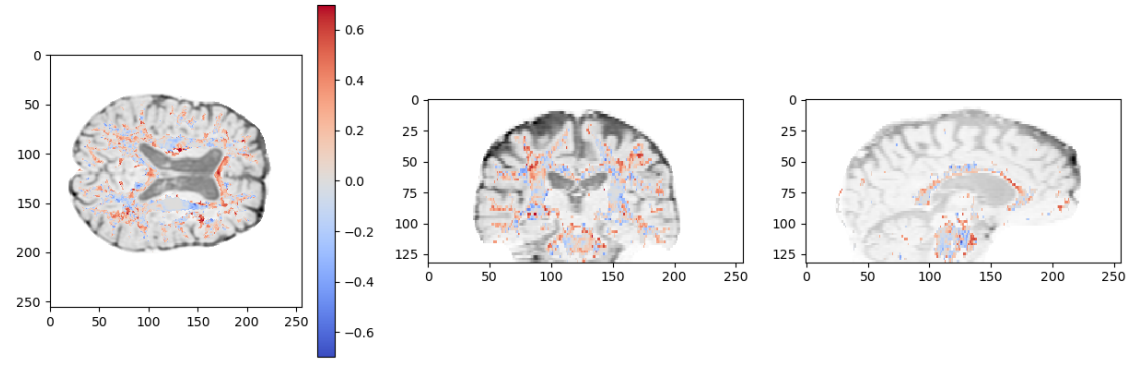

Fig D.6: *Difference in fiber volume fraction attributed to the first fiber population in white matter before and after abstinence. Axial view (Left), coronal view (Middle) and sagittal view (Right).*

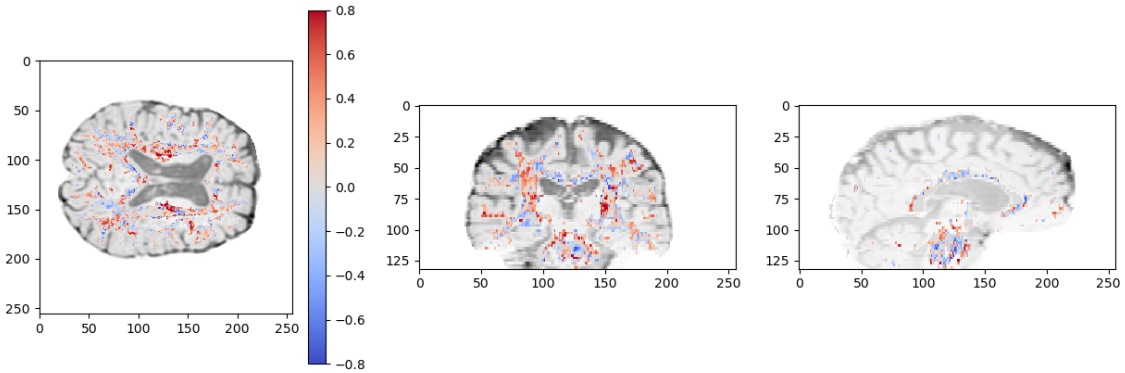

Fig D.7: *Difference in fiber volume fraction attributed to the second fiber population in white matter before and after abstinence. Axial view (Left), coronal view (Middle) and sagittal view (Right).*

D.3 Standard variations and means of metrics

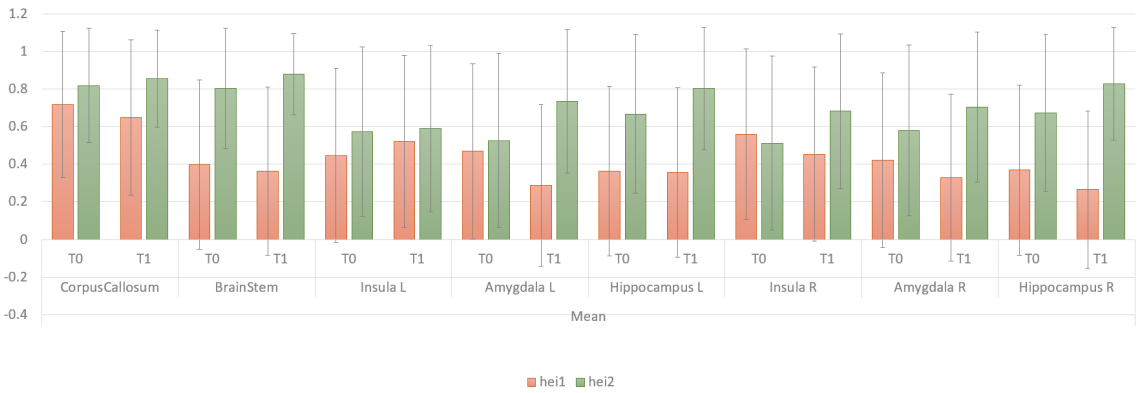

Fig D.8: *Mean and standard deviation of the heterogeneity of the first (hei1) and second (hei2) fiber populations, before (T0) and after (T1) abstinence.*

UNIVERSITÉ CATHOLIQUE DE LOUVAIN
École polytechnique de Louvain
Rue Archimède, 1 bte L6.11.01, 1348 Louvain-la-Neuve, Belgique | **www.uclouvain.be/epl**